Design and Fabrication Technologies for Single-mode Quantum Cascade Lasers

Kenneth Kennedy

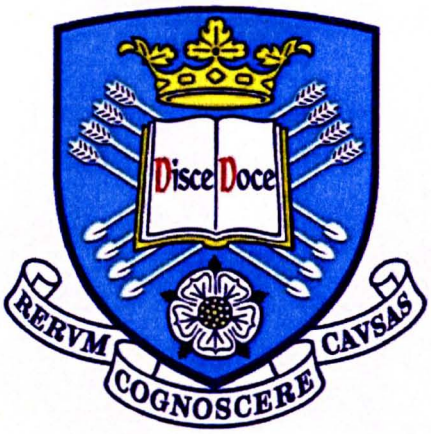

The University Of Sheffield.

Department of Electronic and Electrical Engineering

Thesis submitted to the University of Sheffield for the degree of Doctor of Philosophy

April 2009

Abstract

Quantum Cascade Lasers (QCL's) are unipolar semiconductor lasers offering the potential for low cost, high power, laser sources emitting in the mid- and far- infrared. Single-mode devices are required for spectroscopic and imaging applications because of their narrow emission linewidth and are achieved through distributed feedback (DFB) designs where gratings are incorporated in or close to the active region. This thesis describes design and fabrication technologies for single-mode yield improvements and improved wavelength targeting of QC lasers.

Mid-infrared, single-mode laser designs are developed utilising novel fabrication processes and designs in the indium phosphide (InP) based material system. Lasers without facet coatings, with single-mode yields up to 80% and side mode suppression ratios (SMSR) greater than 25dB are observed. Metalised surface gratings, buried (overgrown) gratings and lateral gratings are defined using inductively coupled plasma (ICP) etching to produce DFB lasers operating above room temperature for wavelengths near to 10μm. A deep etched lateral grating quantum cascade DFB is demonstrated for the first time in the InP material system.

Waveguide modelling demonstrates accurate methods to predict the grating coupling strength of the DFB lasers with good agreement to experimental results. The emission wavelength (λ ~10μm) is found to be highly dependent on the laser ridge width with the experimental shift in wavelength found to be much greater than that predicted. A ridge width and temperature dependence on emission wavelength is utilised in an array device where a continuous tuning range in excess of 230nm is observed.

Finally, an increase in thermal conductance and a symmetric far-field profile are observed for lasers ($\lambda \sim 4\mu m$) with narrow ridge widths. The lasers were designed for improved heat extraction from the active region and a beam quality factor of $M^2 \approx 1$. Almost identical lateral and vertical far-field profiles with high duty cycle operation at thermoelectric temperatures are observed for a ridge waveguide laser that is approximately $5\mu m$ wide.

List of Publications

[1] S. Y. Zhang, D. G. Revin, J. W. Cockburn, K. Kennedy, A. B. Krysa, M. Hopkinson.: 'λ ~3.1μm room temperature InGaAs/AlAsSb/InP quantum cascade lasers', Appl. Phys. Lett. 94, 031106, 2009

[2] A. O. Dirisu, Dmitry G. Revin, Zhijun Liu, K. Kennedy, J. W. Cockburn, C. F. Gmachl.: 'Characterization of Quantum-Cascade Lasers using Single-Pass Transmission Spectroscopy', IEEE J. Quant. Elect, accepted for publication June 2009

[3] Kennedy, K. Revin, D.G. Commin, J.P. Krysa, A.B. Semtsiv, M.P. Chashnikova, M. Masselink, W.T. Cockburn, J.W. Hogg, R.A.: 'Single grating period quantum cascade laser array with broad wavelength tuning range' IEEE Elect. Lett. 2008, 44, 22, pp. 1306-1307

[4] M. Wienold, M. P. Semtsiv, I. Bayrakli, W. T. Masselink, M. Ziegler, K. Kennedy, and R. Hogg.: 'Optical and thermal characteristics of narrow-ridge quantum-cascade lasers', J. Appl. Phys. 103, 083113 (2008)

[5] K. Kennedy, D. G. Revin, A. B. Krysa, J. S. Roberts, K. M. Groom, L. R. Wilson, J. W. Cockburn and R. A. Hogg.: 'Fabrication and characterization of InP-based quantum cascade distributed feedback lasers with ICP etched lateral gratings

Accepted to SSDM 2006 Conference, Special Issue of Japanese J. of Appl. Physics, (2007)

[6] K Kennedy, K.M. Groom, R.A.Hogg.: 'Fabrication of v-groove gratings in InP by inductively coupled plasma etching with $SiCl_4$/Ar', Semi. Science and Tech, 21, L1-L5, (2006)

[7] K. Kennedy, D. G. Revin, A. B. Krysa, J. S. Roberts, K. M. Groom, L. R. Wilson, J. W. Cockburn and R. A. Hogg.: 'High performance InP-based quantum cascade distributed feedback lasers with deeply etched lateral gratings', Applied Physics Letters, 89, 201117, (2006)

[8] S. K. Ray, K. M. Groom, R. Alexander, K. Kennedy, H. Y. Liu, M. Hopkinson, and R. A. Hogg.: 'Design, growth, fabrication, and characterization of InAs/GaAs 1.3 μm quantum dot broadband superluminescent light emitting diode', Journal of Applied Physics, 100, 103105 (2006)

Conference Presentations

1. Oral presentation based on [5] at Solid State Materials and Devices (SSDM) 2006, Yokohama, Japan.

2. Oral presentation based on [7] at UK Compound Semiconductors 2006, Sheffield, U.K.

3. Oral presentation based on [7] at Physics of Inter-subband Emitters, 2006, Cortona, Italy.

4. Oral presentation based on [3] at UK Compound Semiconductors 2007, Sheffield, U.K.

Acknowledgements

The help and encouragement offered by those mentioned below is gratefully acknowledged. The work presented within this thesis would not have been possible without it.

I must first thank my supervisor Dr. Richard Hogg, whose supervision, enthusiasm and advice has been both constant and invaluable. Prof. John Cockburn and Dr. Kristian Groom and Dr. Dmitry Revin, have all supplied great practical knowledge and support during countless discussions. Additionally, the help and advice from Dr. Rob Airey, Dr. Geoff Hill, Dr. Andrey Krysa, Dr. John Roberts and Dr. Luke Wilson and is fully appreciated. Thanks also go to Prof. Ted Masselink and Dr. Mykhaylo Semtsiv of Humboldt University Berlin for their knowledge and epitaxial skills. The excellent fabrication advice and assistance from the staff of the EPSRC National Centre for III-V semiconductors should also be acknowledged, as is the assistance of fellow PhD students, David Austen and Paul Commin. I also acknowledge financial support from the Engineering and Physical Sciences Research Council.

Thankyou to Ryan 'dozo' Alexander, Dr. David Childs, Ben Stevens, Purnima Greenwood and Qi Jiang who shared an office with me and supplied many enjoyable (even if not useful or memorable!) discussions in the pub. I must not forget the III-V Tigers football team for providing many evenings of fun, even if little success.

A huge thank you goes to my baby son Jacob for keeping the sleepless nights

to a minimum and to Sarah for her understanding and for taking more than her fair share of the work. Finally, thank you to my parents for their endless support and continual interest, beyond the call of duty.

List of Contents

Chapter 1 - Introduction

1.1 General introduction

This chapter introduces some of the motivation and history of semiconductor and quantum cascade laser (QCL) development and includes some principles of operation for semiconductor and quantum cascade lasers. Additionally, the general processes and mechanisms involved in plasma etching will be described. The basic device fabrication processes involved in making the QCL devices presented in this thesis are included along with details of experimental set-ups used to optically and electrically measure the laser characteristics.

Since the invention of the semiconductor laser in 1962 [1-4] there have been various applications for these devices due to their compact size. Rapid development of near-infrared (NIR) lasers ($\lambda \approx 0.7\mu m - 2.5\mu m$) yielded improvements in device performance including output power and efficiency, meaning that they became reliable, low-cost, coherent sources for such applications as optical fibre communications. In recent years an increasing amount of attention has been given to the detection and analysis of trace gases, in the parts-per-million (ppm) to parts-per-trillion (ppt) range, for environmental and industrial process monitoring. As most molecules have their fundamental rotational-vibrational absorption bands in the mid-infrared "fingerprint" region of the spectrum ($\lambda \approx 2.5\mu m - 20\mu m$), a significant number of applications are available for laser sources emitting in this technologically important wavelength range. QCL's are high power and potentially low cost laser sources operating above room temperature. To achieve a narrow emission linewidth

(suitable for spectroscopic applications) a distributed feedback (DFB) laser design may be adopted. This design incorporates a grating in the laser structure to achieve a single frequency output where the emission wavelength is determined by the grating dimensions. This design is the basis for the majority of devices demonstrated in this thesis.

The development of semiconductor lasers at longer wavelengths has been slow in comparison to NIR lasers. For ultra-sensitive, high-resolution trace gas analysis applications it is desirable to have an inexpensive, single-frequency laser source that operates at room temperature. The mid-infrared (MIR) region contains many strong features in the absorption spectrum of atmospheric trace gases and so enables much more sensitive detection of trace amounts of molecules. The 'atmospheric windows' (low absorption range) in the absorption spectrum ($\lambda \approx 3\mu m$ - $5\mu m$ and $8\mu m$ - $14\mu m$) are of significant interest. Low background levels of absorption permit longer beam paths to be used in gas sensing applications, providing greater sensitivities and less atmospheric artefacts. Lasers emitting in these wavelength ranges are also potential sources for free-space communications, military counter measures and non-invasive medical diagnostics.

The seminal work of Kazarinov and Suris [5] in 1971 first proposed lasers based on intersubband transitions in quantum wells. In 1994, the first demonstration of a novel type of unipolar intersubband semiconductor laser ($\lambda \sim 4.3\mu m$) by Bell Laboratories was the start of a new class off semiconductor devices. The emission wavelength was controlled by the grown layer thicknesses rather than by the material bandgap. Swift progress and development meant that performance requirements for such applications

as trace gas sensing were soon realised. Quantum cascade lasers as they became known, were first achieved using the III-V semiconductor material system of $In_{0.53}Ga_{0.47}As$ / $Al_{0.52}In_{0.48}As$ grown on latticed-matched indium phosphide (InP). This material system has allowed the realisation of lasers over the wide wavelength range of ~3μm to ~24μm. However, lasers based on other material systems such as gallium arsenide (GaAs) / AlGaAs have been realised with wavelengths up to ~ 250μm [6]. These far-infrared (FIR) 'Terahertz' quantum cascade lasers are of significant interest for security / imaging applications. Although of interest, mid-infrared GaAs-based QCL's typically show poorer performance than InP-based devices and as a consequence, this thesis concentrates on InP-based QCL's.

1.2 Mid-infrared laser sources

Since high-resolution spectroscopy applications require a coherent, tuneable, single-frequency source with very narrow linewidth, the much larger sized gas lasers like the $C0_2$ laser ($\lambda \sim 10\mu m$) have typically been used as mid-infrared sources utilizing their high optical output power and narrow linewidth. Until recently, the only suitable semiconductor sources in the mid-infrared region were IV-VI lead-salt (e.g. PbS, PbSe, PbTe) lasers [7] invented in 1964. Even though they have a wide emission range ($\lambda \sim 3\mu m - 30\mu m$) and temperature tuneable wavelength, they generally only operate at low temperatures, partly due to the low thermal conductivity of the materials. Large non-radiative recombination rates, dominated by the Auger process make interband lasers at longer wavelengths difficult to achieve at room temperature [8]. The energy and momentum of an electron-hole pair can transfer to another carrier (generally electrons) leading to an increased relaxation rate (increasing with

temperature) which makes population inversion difficult to obtain.

Antimonide-based, type-I quantum well diode lasers have been demonstrated in continuous-wave (cw) operation up to a wavelength of ~3μm [9] with single mode lasers available commercially up to a wavelength of ~2μm [10]. Increasing the wavelength is problematic with GaInAsSb / AlGaAsSb active regions. One reason being decreased material quality. Type-II "W" diode lasers [11] are another potential source and have demonstrated good performance in the 3-4μm range with continuous wave operation up to 230K [12] and pulsed operation up to 317 K [13]. The device was proposed by Meyer *et al.* in 1995 and was given the "W" name because of the shape of the conduction band profile.

Interband cascade lasers (ICLs) are semiconductor lasers which utilise a cascade scheme similar to that of QCL's. However, the radiative transitions occur between the conduction and valence bands. The concept was first proposed by Yang [14] in 1995 and an improved design was published later by Meyer *et al.* [15]. Devices with wavelength up to 5.4μm have been reported [16] but the best performance is in the 3-4μm wavelength range. Continuous wave operation below room temperature has been reported at 3.3μm [38] and at 3.7μm [17]. Single-mode IC DFB lasers are also available commercially [18].

1.3 General laser principles

A laser is a device that amplifies light and typically produces a high intensity beam of light with a very narrow wavelength spectrum. However, broad wavelength or multiple wavelength laser sources are possible and are also of significant

technological interest [19] [20]. A laser makes use of processes that increase or amplify light after it has been generated by other means. There are basically two requirements for laser operation. Firstly, a gain medium is required to amplify the electromagnetic radiation propagating inside it and provide spontaneous emission input. Secondly, a feedback mechanism is required to confine the electromagnetic field.

Basic laser operation is through the creation of photons by the stimulated relaxation of particles in an excited energy state. For a simple two level atomic like system (lower and upper states) a particle will generally tend to be in the lowest possible energy state. If a photon is incident on the material with an energy that is equal to the energy gap between the lower and upper levels then there is a high probability of the particle gaining energy and making the transition to the upper energy state. This is the process of stimulated absorption. The particle will not remain indefinitely in the upper state. Typically, after a few tens of nanoseconds the particle will make the transition back to the lower energy state and will emit a photon in the process. This process of spontaneous emission results in a photon with energy equal to the energy gap (E_2-E_1). When a photon with energy equal to the energy gap is incident on the material (when the particle is in the upper state) then stimulated emission may occur. Stimulated emission can happen when the incident photon ($E = E_2$-E_1) causes the relaxation of the particle from the upper state to the lower state. The stimulated photon will then have the same direction and wavelength as the photon that initiated the transition of the particle and both photons will have identical phase and state of polarisation. As shown in Fig.1.1, this process forms the basis of light amplification in lasers. For semiconductor lasers in their natural state, the population of particles (electrons) will

be much greater in the lower energy state than upper state. Consequently, the probability of an incident photon contributing to the stimulated emission will be negligible compared to the absorption process. For laser action to occur it is necessary to achieve 'population inversion' so that the upper state occupancy is higher than the lower state and so stimulated emission is the dominant mechanism. In practice, to achieve population inversion the upper level must be injected with electrons (electrical or optical pumping) from a separate level and the lower level must be depopulated by extraction to another level. Therefore, in reality most practical laser systems will contain more than two levels.

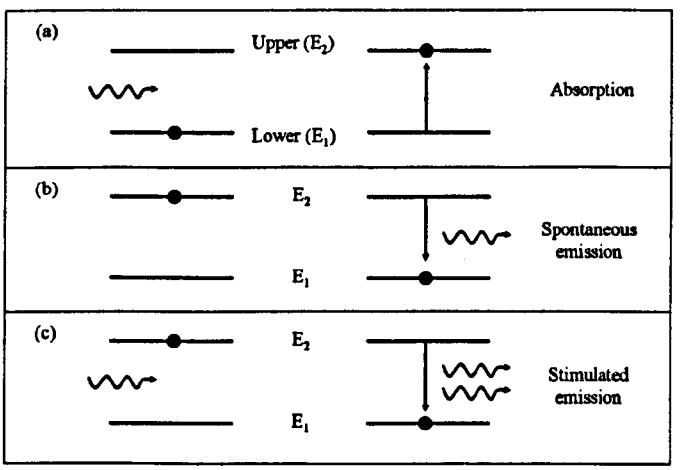

Figure 1.1 Schematic diagram of a two level atomic like system showing the processes of (a) absorption (b) spontaneous emission and (c) stimulated emission. Left hand side indicates the initial state and right hand side indicates the final state.

A four level system is used in many laser systems and has significance in the design of QCL active regions. Electrons are excited from level 1 to 4 and then rapidly decay into level 3. Between levels 3 and 2 the laser transition takes place with the population

of level 2 kept low by ensuring rapid relaxation into level 1. This helps to achieve population inversion by efficiently transferring electrons into the upper laser level and by fast relaxation out of the lower laser level. This four level system is illustrated in Fig.1.2.

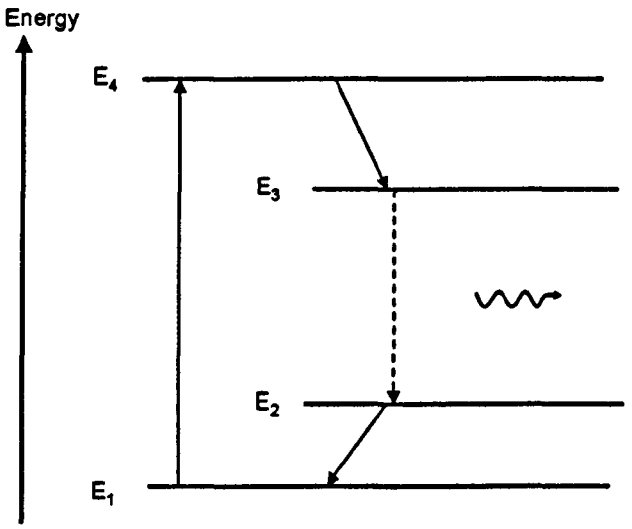

Figure 1.2 Schematic diagram of a four level laser system used to achieve population inversion. Level 4 can be populated by either optical pumping at a shorter wavelength than the laser transition (dashed line) or by electrical injection of carriers.

Optical confinement and feedback are required to reduce the loss of stimulated photons. Stimulated photons can stimulate other photons to increase the gain or may be lost by escape or by absorption. To increase the amount of gain material the photon travels through, a Fabry-Perot (FP) cavity may be formed by producing two parallel mirrors at the ends of the gain material. In semiconductor lasers this is usually achieved by cleaving along the crystal axes producing mirror like 'facets' which result in optical feedback. Since the optical cavity is generally much longer than the laser wavelength a large number of longitudinal optical modes are permitted, with a mode

spacing given by,

$$\Delta\lambda = \lambda^2 / 2nL \qquad (1.1)$$

where (n) is the effective refractive index of the optical mode and L is the length of the FP cavity. Typical cavity lengths for QCL's are in the range of 0.5mm to 3mm resulting in a relatively small FP mode spacing. The gain peak is usually large in comparison so it is very likely there will be lasing on several FP modes. This broad spectral characteristic of a FP laser makes it unsuitable for many gas sensing applications (especially spectroscopic) and so DFB laser designs are often utilised. The facet mirror losses for the laser are dependent on cavity length with a value given by,

$$\alpha_m = (1/2L) \ln(1/R_1R_2) \qquad (1.2)$$

where R_1 and R_2 are the facet reflectivities and L is cavity length (cm). Typically, for semiconductor lasers in the near infrared the facet reflectivity is approximately 30%.

Dielectric waveguiding is used to confine the optical mode by total internal reflections by sandwiching the gain material (active region) between two cladding layers and defining the material into a ridge structure. Usually, the cladding layers are of a lower refractive index material and with as low absorption as possible. Waveguide design is discussed in more detail in chapter 2. Waveguide losses (α_w) due to such mechanisms as absorption or scattering (from material interfaces) in the gain medium must be overcome before there is a net gain, allowing lasing to occur. An expression for the wavelength dependent, threshold modal gain coefficient g_{th} of a semiconductor laser may be written as,

$$g_{th} = \alpha_w + \alpha_m \quad (1.3)$$

$$g_{th} = \Gamma g_a \quad (1.4)$$

where (Γ) is the overlap of the optical mode with the gain region and (g_a) is the active medium gain. Typically, units for (g_{th}) will be in reciprocal centimetres (cm^{-1}).

1.3.1 Light output versus input current

It is necessary to measure laser diode characteristics to quantitatively assess the quality of both the device and laser material. One of the most important parameters for any laser diode is the amount of light emitted compared to the amount of current injected into the device. It is commonly referred to as the L-I curve. In Fig.1.3 an example of a laser L-I curve is shown. It first demonstrates spontaneous emission which gradually increases with injection current until stimulated emission occurs. At this point, the onset of lasing action occurs. The injection current at this point is referred to as the threshold current (I_{th}). Threshold current is highly dependent on device geometry. When comparing devices that are not identical (e.g. ridge width, cavity length, gain region volume) then threshold current density (J_{th}) is often more appropriate. In ridge lasers this can be obtained by dividing the experimental threshold current value by the area of the laser ridge. The threshold current density is a good indication of the quality of the semiconductor material. It is desirable to have as low a value for J_{th} as possible, but it is also desirable to get as much output power for as little current as possible. The ability of a laser to convert electrical power to light can be directly measured from the slope of the L-I curve above threshold. The number of Watts of laser output for every Ampere increase in current is given by $\Delta P/\Delta I$ as shown in Fig.1.3.

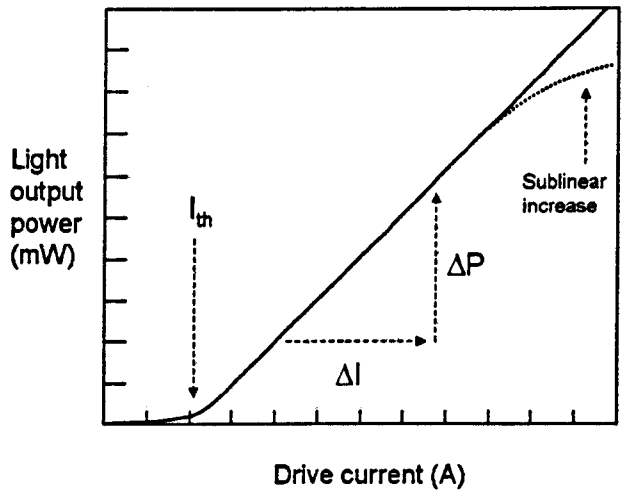

Figure 1.3 Example of an L-I curve for a semiconductor laser. Light output power is plotted against drive current. Point of laser action is denoted by I_{th}. Dotted line indicates common behaviour of semiconductor lasers where power no longer increases linearly with increasing drive current.

Transparency threshold current density (J_0) is another significant parameter that can be extracted from experimental data and is independent of device length. It is obtained by plotting the threshold current density versus the inverse cavity length (1/L). An example of this is shown in Fig. 4.12. The intercept of the linear fit line with the vertical axis is the value of J_0. This value can be thought of as the threshold current density of an infinitely long laser which has no mirror losses. It should be noted that this is not suitable for DFB lasers due to length dependent grating effects explained later in chapter 2.

1.3.2 Temperature sensitivity

The light-current characteristics of semiconductor lasers are strongly dependent on

temperature. The threshold current (point of laser action) will typically increase with temperature, limiting the laser performance. The slope of the linear part of the L-I curve will be lower (less efficient) and the onset of the sublinear part of the curve (as shown in Fig.1.3) will happen more quickly after threshold. For the same current there will be less output power at higher temperatures.

Typically, more current is required for lasing at higher temperature, which in turn causes a further increase in internal laser temperature, compounding the situation. This temperature limitation on performance has meant considerable work has been carried out to understand temperature sensitivity. The characteristic temperature (T_0) is a measure of the temperature sensitivity of a laser. Higher T_0 values imply that the threshold current density increases less rapidly with temperature. Experimentally measured J_{th} values can be plotted on a logarithmic scale against temperature as demonstrated in Figure 1.4. The inverse of the slope of the linear fit is equal to T_0.

The centre wavelength of a semiconductor laser is linearly related to its operating temperature. The wavelength increases with increasing temperature. This is sometimes advantageous for spectroscopic applications but undesirable for other applications like some telecommunications applications where the laser emission needs to be as stable as possible. For FP interband lasers the shift in wavelength with temperature is typically ~ 0.4 nm/K. This is can be reduced to less than 0.1 nm/K for quantum dot lasers [21] which are of technological interest due to their low and theoretical temperature insensitive threshold current. Quantum cascade lasers exhibit larger changes in wavelength. Typically, mid infrared QCL values are in the region of ~1 nm/K.

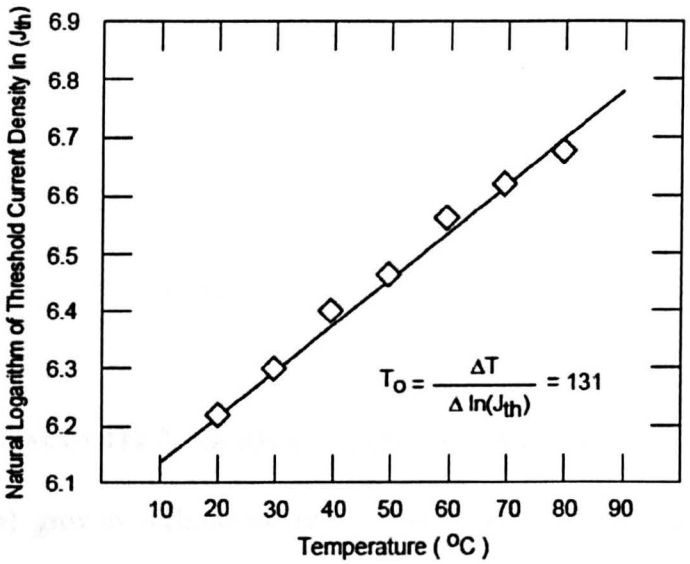

Figure 1.4 Example plot of laser threshold current density variation with temperature. Characteristic temperature may be obtained from the inverse slope of the linear fit line. Reproduced from [22]

1.3.3 Spatial-mode characteristics (Near and Far Field)

Semiconductor lasers generally emit a spot of light with an elliptical cross section. The 'near field' is the spatial intensity distribution of the emitted light, very close to the laser facet. As the light propagates away from the device the spot size will increase due to divergence. The angular intensity distribution further away from the laser facet is known as the 'far field'. The spot size and divergence angles in both the lateral (parallel to grown layers) and vertical (perpendicular to growth) directions are associated with the laser mode(s) propagating in the laser cavity and are dependent on the lateral and vertical waveguide dimensions and material refractive indices. Measuring these parameters is often important in understanding the spectral and electrical characteristics of a laser. For certain applications a circular spot is desirable to simplify the optics required to focus the beam. The divergence is important in

determining the coupling efficiency when launching the beam into optical fibre. Mathematically, the far field is obtained by taking the Fourier transform of the near field. Experimentally, a photodetector may be scanned across the beam in either direction to profile the intensity pattern. The full-width-at-half-maximum (FWHM) values are generally used to measure the dimensions of the spot.

1.4 Properties of III-V semiconductor materials

Modern epitaxial growth techniques such as molecular beam epitaxy (MBE) and metal organic vapour phase epitaxy (MOVPE) allow the very thin layers (few nanometers) of different semiconductors to be deposited. High quality crystal layers on the atomic scale are possible with abrupt interfaces allowing many advanced semiconductor devices to be realised. The growth of the layers is limited by the lattice matching between the alternating semiconductor materials. Certain combinations of III-V materials (e.g. $In_{0.53}Ga_{0.47}As$ and $Al_{0.52}In_{0.48}As$) are more technologically developed because they are latticed matched or only slightly different. Also, it is advantageous for the grown layers to be lattice matched to a convenient substrate material (e.g. InP).

1.4.1 Semiconductor heterostructures and quantum wells

The concept of the heterostructure laser diode first proposed in the 1960s, leading to the double heterostructure (DH), were responsible for large improvements in laser performance (significantly lower threshold currents). The DH active region layer is surrounded by a higher bandgap material. This enables the transverse confinement of both the injected carriers and optical field. When two different semiconductor materials (different bandgap) are grown directly on top of each other a junction is

formed at the interface. The change in bandgap at the interface results in a discontinuity in the conduction band (CB) and valence bands (VB). The size of the changes in the CB and VB are known as the conduction and valence band offsets. These are denoted by ΔE_c and ΔE_v respectively. A quantum well is formed when a thin layer of semiconductor material is sandwiched between two layers of a material with a larger bandgap. The bandgap difference forms a potential well for electrons with a depth of ΔE_c. The free motion of the electrons is restricted to the direction parallel to the layers with discrete quantum energy levels formed in the perpendicular direction. This is known as a two-dimensional system. Quantum well (QW) structures like QCL's and conventional interband QW lasers have active regions made up of multiple quantum wells situated within waveguides of lower refractive index. In Fig.1.5 the basic concepts of the semiconductor double heterostructure and quantum well are illustrated schematically.

Controlled addition of an impurity during the growth process into the crystal lattice is known as doping. Adding a dopant that is an electron donor produces a material with excess negative charge carriers and so electrons are the majority carrier. Conversely, an acceptor dopant produces p-type material where holes are the majority carrier. In the case of conventional QW interband lasers, the top cladding layer and will typically be p-type and the lower cladding and substrate then n-type. When a forward biased external voltage is applied electrons and holes can move freely to the active region. However, the potential barrier (resulting from bandgap difference) means that they cannot move to the other side and so a substantial build up of electrons and holes occurs. This enables the recombination of electrons from the conduction band and holes from the valence band producing optical gain. Photons emitted during radiative

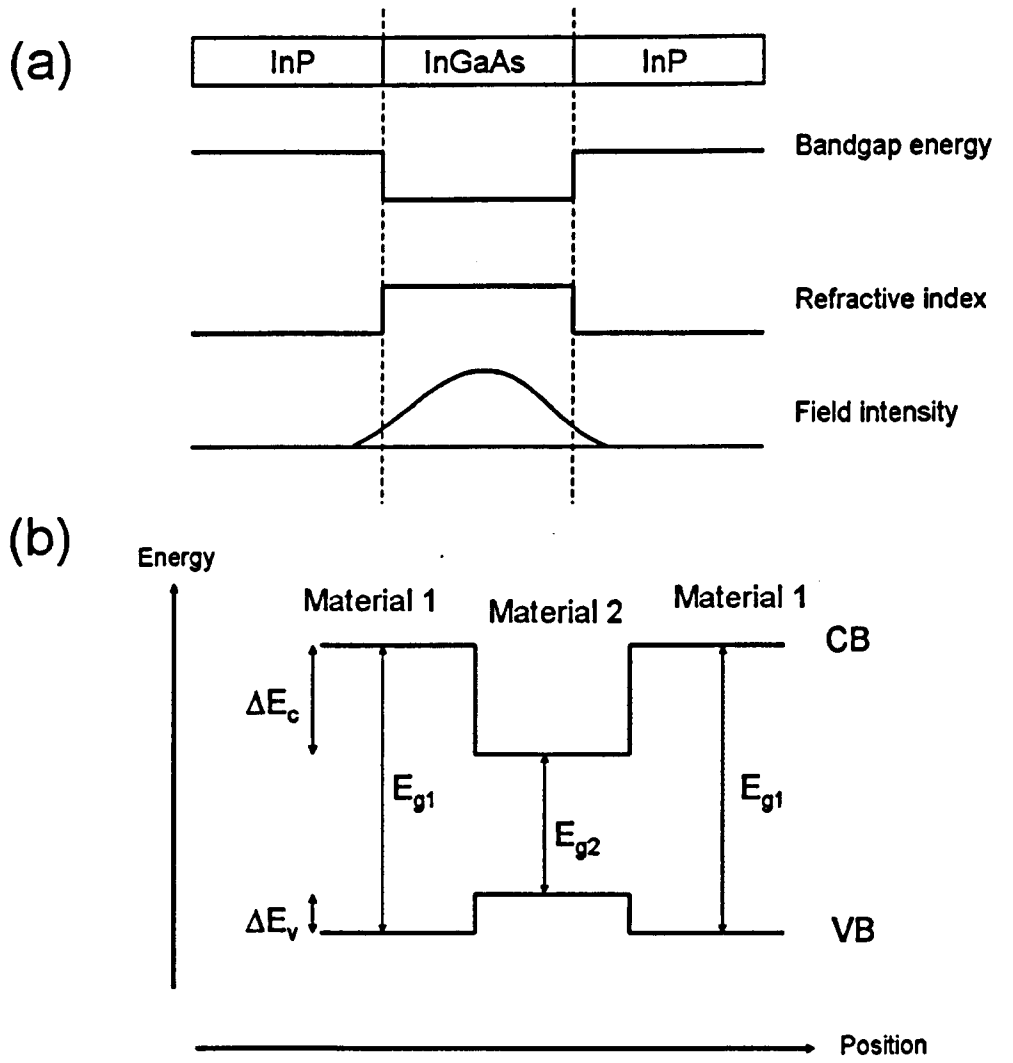

Figure 1.5 Schematic diagrams illustrating (a) bandgap energy, refractive index and transverse field intensity of a double heterostructure (b) energy diagram of a single quantum well formed by a thin layer (material 2) sandwiched between two barrier layers (material 1) with wider bandgap. Conduction band (CB) and valence bands (VB) offsets (ΔE) are shown.

recombination will have energy equal to the bandgap energy (E_{g2} in Fig.1.5b). This energy is related to the emission wavelength of the photon by $E = hc/\lambda$ (where h is the Planck constant). Lasers based on interband transitions are restricted in the upper

wavelength range by the magnitude of the bandgap energy. The limit is approximately 2μm for conventional type-I laser devices with band structure similar to that in Fig.1.5b.

1.5 Quantum cascade lasers

1.5.1 Selected history of QCL development

The first QCL ($\lambda \sim 4.3\mu m$) demonstrated by Faist *et al.* [23] in 1994, at Bell Laboratories in the InGaAa/InAlAs/InP material system, was grown by MBE and worked in pulsed mode at cryogenic temperature. Since then large improvements in performance have been achieved, primarily due to optimization of active region designs. In 1996, Faist [24] presented a three quantum well active region with vertical transition. This design had narrow well close to the injection barrier and demonstrated pulsed operation at room temperature for the first time. Three well designs were responsible for good performance over a large wavelength range from 3.4μm [25] to 13μm [26]. High optical powers and current carrying capabilities were introduced around 1997 with the superlattice (SL) active regions investigated by Scamarcio *et al.* [27]. Chirped (wells of decreasing width) SL active region designs by Tredicucci *et al.* [28] offered an undoped active region and hundreds of milliwatts of power in cw operation up to ~150K. Good performance at wavelengths up to 24μm have been demonstrated [29].

Two new designs were introduced in 2001 to achieve high temperature, continuous wave operation. The 'bound-to-contiuum' [30] and the four quantum well [31] 'two-

phonon resonance' designs were presented by the Faist group at the University of Neuchatel. The bound-to-contiuum design was intended to combine the advantages of the three QW design and the chirped SL designs with efficient electron injection into the upper state and efficient extraction from the lower state. The four well design utilises the three lower states which are engineered to be separated by two optical phonon energies. This enables efficient depopulation of the lower levels and improved performance at higher temperatures. This design was used in the first demonstrated QCL with continuous wave operation ($\lambda \sim 9.1\mu m$) at room temperature by Beck *et al.* [32]. An important milestone in QCL development was the first demonstrated laser device grown by metal organic vapour phase epitaxy (MOVPE). This was achieved at the University of Sheffield in 2003 [33] [34]. MOVPE offers multi-wafer growth capability and does not require as long baking cycles to recover from atmospheric contamination as MBE growth. This coupled to faster growth rates and the ability to grow a whole structure in a single step makes MOVPE more suitable to commercial production. Demonstrated lasing just below 3μm has been demonstrated in the InAs/AlSb material system by Devenson *et al.* from the University of Montpellier [35]. Another promising material system for low wavelengths is the InGaAs/AlAsSb material system which is lattice-matched to InP. The first laser based on these alloys was reported in 2004 by Revin *et al.* (University of Sheffield) [36]. Room temperature operation was reported recently by the same group in 2009 [37]. In 2007 the Razeghi group at Northwestern University reported the development of ($\lambda \sim 4.7\mu m$) strain-balanced InP-based quantum cascade lasers with high wall plug efficiency and room temperature cw operation [38]. They used narrow-ridge buried heterostructure waveguides and thermally optimized packaging. Over 9.3% wall plug efficiency was reported at room temperature from a single device producing over

0.675 W of cw output power. For devices at a temperature of 150K, output powers of more than 1W were measured.

Single-mode DFB lasers as mentioned previously are important devices because of their narrow emission linewidths, suitable for spectroscopic applications. Predictably, following on from the improvements in QCL performance, research on DFB QCL's quickly followed. In 1997, Faist *et al.* [39] demonstrated the first DFB lasers (pulsed operation) at two wavelengths (λ ~5μm and 8μm). Room temperature, continuous-wave operation has now been demonstrated over the wavelength range of approximately 4.8μm [40] to 10μm [41]. In pulsed mode at 80K, single-mode lasing has been demonstrated as low as 3.95μm in a surface emitting ring DFB laser design [42].

1.5.2 Principles of operation

1.5.2.1 Electron-phonon scattering.

For an ideal crystal lattice the atoms are arranged in periodic positions such that at 0K an electron would not undergo any scattering when it travelled through the lattice. In a real crystal lattice, impurities, defects, other carriers and lattice vibrations (phonons) give rise to scattering of carriers. Phonons are lattice vibrations in a crystal resulting from the displacement of the ions in the lattice away from their equilibrium energy positions. The vibration energy is quantised and has increasing amplitude with temperature. Vibrations of two species of atoms in the lattice where they move in anti-phase with each other causes a transfer of electric charge which interacts with electromagnetic waves leading to an 'optical' phonon classification. Acoustic phonons arise from atoms moving in-phase with each other. The direction of motion can be longitudinal or transverse and so longitudinal optical (LO), transverse optical

(TO), longitudinal acoustic (LA) and transverse acoustic (TA) branches are classified. Acoustic phonon scattering energies are several orders of magnitude lower than the important scattering energies in QCL design. However, electron-optical phonon scattering events are much larger and significant at infrared energies. Once the energy spacing between subbands in a QCL system becomes equal to the optical phonon energy, scattering between the two levels becomes possible by the emission by an LO phonon. This speeds up the relaxation time (~ps) and is used in the design of QCL's where a fast non-radiative scattering rate is engineered between two energy levels in a system of coupled quantum wells, by designing their energy spacing to be close to an LO phonon energy.

1.5.2.2 Coupled quantum wells and density of states.

Quantum cascade laser active regions consist of multiple quantum wells (hundreds of alternating semiconductor layers). QCL's differ from conventional diode lasers in many fundamental ways. Typically, one of them being the absence of p-type material. As illustrated in Fig.1.6, these unipolar lasers rely on only one type of carrier (electrons) which make intersubband transitions (between conduction band states (subbands) only. This smaller energy transition facilitates longer wavelength photons than conventional interband lasers discussed. As explained previously for conventional quantum well diode lasers, conduction band electrons and valence band holes radiatively recombine across the bandgap, when injected into the active region through a forward biased p-n junction. The bandgap essentially determines the emission wavelength. QCL transitions arise from size quantisation in the semiconductor heterostructure so wavelength is essentially due to the grown layer thicknesses in the active region. In principle, many semiconductor materials may be

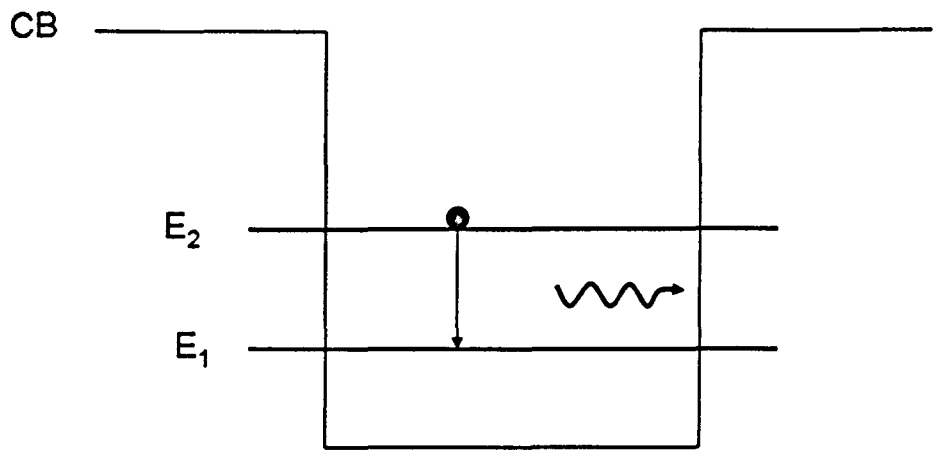

Figure 1.6 Schematic diagram of a photon emission originating from a transition of an electron in the conduction band (intersubband transition).

used to achieve a QCL, but in reality there are other factors limiting material choice. The low refractive index and good thermal conductance of InP makes it a good waveguide material for mid-infrared QC lasers. A good optical waveguide is extremely important for confining the optical mode to the gain region and increasing the rate of stimulated emission. However, the required thickness of the cladding layers, for some materials, may be found to be so thick that it becomes impractical in terms of growth time and device fabrication. Thermal resistance should be minimised to aid the thermal dissipation of heat that is generated in the active region. At even longer wavelengths (>20μm) GaAs based devices may have greater design and growth flexibility but mid-infrared devices have generally shown higher threshold current densities and lower temperature operation. Furthermore, the greater effective mass of GaAs compared to $In_{0.53}Ga_{0.47}As$ when used as active region wells acts to reduce the probability of an electron in the upper laser level decaying radiatively. GaAs based devices typically use AlGaAs barriers. This structure has a lower

conduction band offset than for InGaAs / AlInAs active regions and so the maximum transition energy is limited. There is also an increased probability of electrons being thermally promoted from the upper laser level into the continuum above the barriers.

The discrete quantised energy levels formed in the growth direction have energies and wavefunctions that can be found by solving the Schrödinger equation (for a well formed between infinitely high potential barriers). For finite potential depths (real case) numerical techniques are required. Each confined electron wavefunction (ψ) has a squared wavefunction $|\psi|^2$. The squared wavefunction describes the probability of finding a particle (electron) per unit distance [43]. They are often plotted in schematic representations of the active region conduction bands of QCL's to visualise the energy levels of the laser system and indicate confinement energy and the spatial regions over which the energy levels are localised.

The density of states (DOS) is modified by a confinement potential (quantum well). In Fig1.7, the DOS is illustrated for bulk material (3D) and quantum well material (2D). For the quantum well case, we see abrupt increases in the density of states occurring at the minimum energy of each subband. Classically, an electron would be reflected by a potential barrier unless its energy was larger greater than the top of the barrier. However, quantum mechanically, due to the wave-like nature of the electron there is a finite possibility that it can tunnel through the barrier. In a QW with a finite barrier height the wavefunctions may penetrate into the barrier material with exponential decay. If the barrier is sufficiently thin the electron wavefuntion may 'leak' through. If there are two wells separated by a barrier a coupling of the quantum wells can take place. In isolation both wells and wavefunctions are identical. However, when

separated by a thin barrier the electrons experience an interaction over both wells and are able to tunnel between them. As the barrier is made thinner a larger coupling occurs and the two ground state levels (equal in the isolated case) become split into a coupled ground state and first excited state. This principle can be extended to multiple quantum wells as in quantum cascade laser active regions.

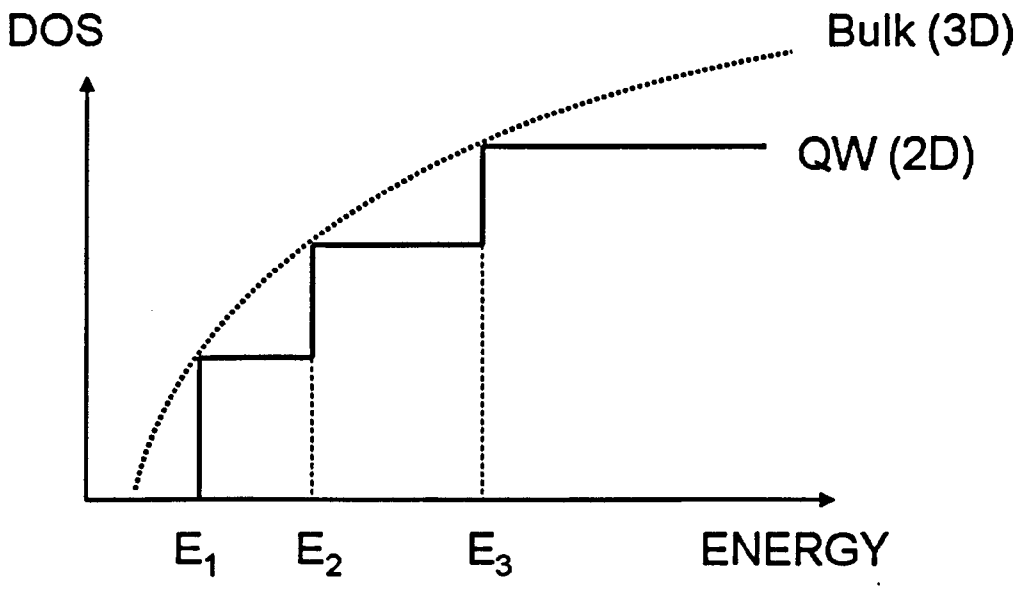

Figure 1.7 D*ensity of states (DOS) versus energy for Bull material (dashed line) and for 3-dimenional case of a quantum well (solid line).* E_1- E_3 *represent the confinement energies of the ground, first and second QW excited states.*

Multiple quantum wells, sometimes referred to as a superlattice, can be coupled. The closely spaced states (separated due to the coupling) form a miniband of states delocalised over the wells, as do the first and second excited states. Any other confined excited states will do likewise. This is illustrated in Fig.1.8a for five identical coupled quantum wells.

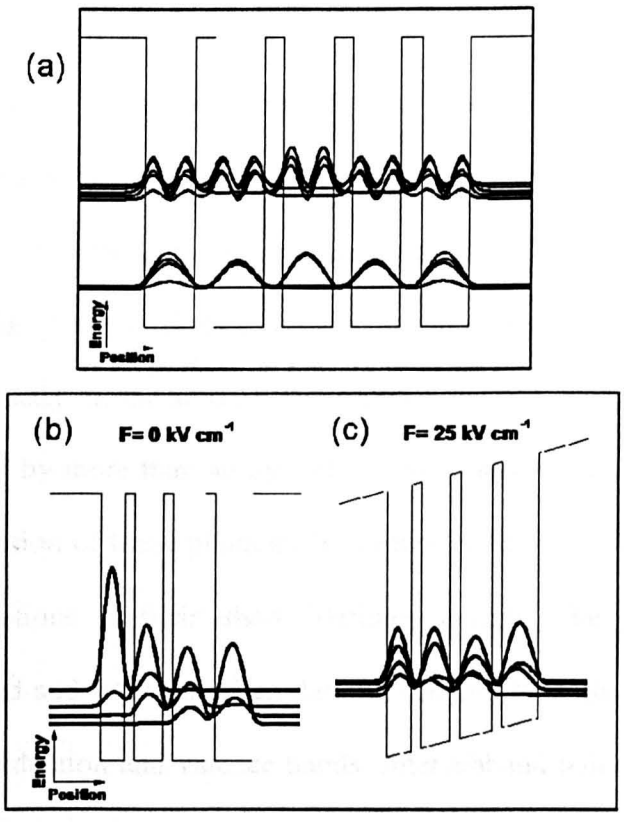

Figure 1.8 Conduction band diagrams with squared wavefunctions for (a) five coupled quantum wells at zero electric field (b) modulated four well structure (c) four well structure with applied electric field. Reproduced from [44]

When an electric field is applied in the direction of growth, the ground state energy in each well separates, decoupling the levels. However, as discussed later, in QCL active regions the well and barrier widths are modulated. In this case, at zero applied electric field (Fig.1.8b) the electronic wavefunctions are separated and localised in individual quantum wells. When an electric field is applied at a certain bias voltage (Fig1.8c), the energy levels align, forming a miniband of states. This enables efficient conduction of electrons through the structure.

In Fig. 1.9, the principal characteristics of interband and intersubband transitions in quantum wells are shown schematically. The joint density of states is constant for energies larger than the transition energy E_{21} for interband transitions. In contrast, intersubband transitions have a sharp joint density of states that is atomic-like and peaked at E_{21}. This results in a narrow gain linewidth. Since the initial and final subbands have the same curvature (neglecting nonparabolicity), this linewidth depends only indirectly on the subband populations through collision processes. For subbands separated by more than an optical phonon energy, the dominant scattering process is the emission of these phonons. Therefore, a fundamental characteristic of intersubband transitions is their short lifetimes (~1ps). The gain in interband transitions is limited and saturates when the electron and hole quasi-Fermi levels are well within the conduction and valence bands. Intersubband gain does not have this limitation and is only limited by the amount of current that can be driven in the structure to sustain the population in the upper state.

The repeated multi-stage structure of the QCL is a fundamental aspect of the active region design. Electrons are recycled from period to period contributing to gain and photon emission each time. Therefore in principle, an electron injected into the structure above threshold, will generate the same number of photons as the number of stages. The differential efficiency and power will then be proportional to the number of stages. Typically, QCL's will have 16 to 50 stages allowing high output powers.

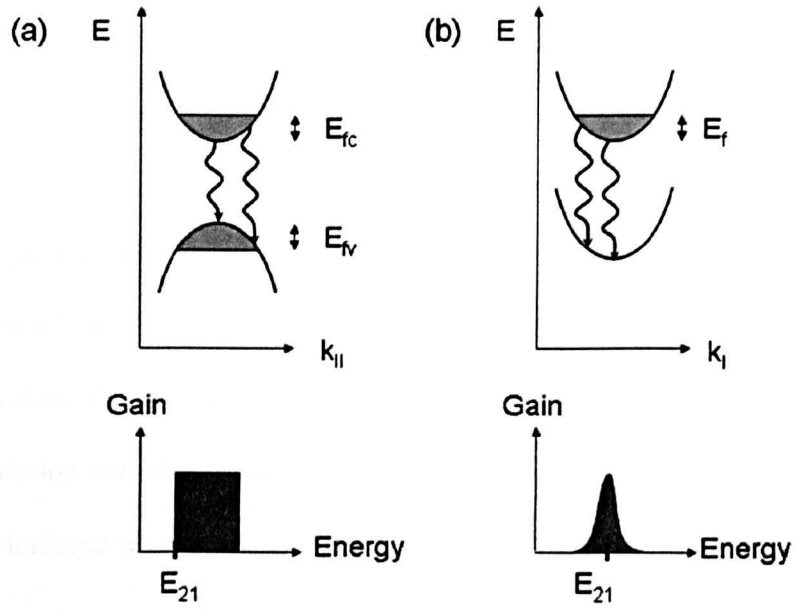

Figure 1.9 Schematic diagrams illustrating (a) interband transition (b) intersubband transition, in a quantum well.

1.5.3 Active region design

The first demonstration of laser emission from intersubband transitions by Faist *et al.* was based on the material system of $In_{0.53}Ga_{0.47}As$ / $Al_{0.52}In_{0.48}As$ grown on latticed-matched InP. QCL's typically consist of active core regions consisting many repeats of identical stages. Each stage consists of an active region followed by a bridging (relaxation-injection) region. The general philosophy of the design and the conduction band diagram (under bias) for the original three quantum well laser structure is shown in Fig.1.10 (a) and (b) respectively. The electric field needs to be sufficient that the lower laser level of any given period is at a higher energy than the upper laser level of the next repeated stage. If a simplified model is assumed with 100% injection efficiency into level E_3 then the population inversion condition is simply $\tau_{32}>\tau_2$ where τ_{32} is the radiative transition and τ_2 is the carrier lifetime in level E_2. In reality, the nonradiative transition 3-1 is not negligible in coupled well structures so the previous

condition is actually not as stringent as the requirement that $\tau_3>\tau_2$ between the total lifetimes of states E_3 and E_2. In most QC structures the lifetime of in E_2 is determined by the scattering rate to the lower subband E_1. In Fig.1.10b the electrons are injected into the structure from the right of the diagram and the laser transition again takes place between levels E_3 and E_2. The quantum wells and barriers in the active region are designed so that the energy spacing between the two levels corresponds to the desired emission wavelength of the laser. Population inversion is achieved with the reported calculated lifetimes of $\tau_3 \sim 2.5$ps, $\tau_{32} \sim 4.3$ps and $\tau_{21} \sim 0.6$ps which satisfies the $\tau_{32}>\tau_2$ requirement [45]. Fast transfer of electrons between levels E_3 and E_2 is ensured by engineering the two levels to be equal to the energy of an optical phonon (34meV). The energy levels in the bridging region are designed to allow fast extraction of electrons from E_1 and E_2. The tunnelling escape time out of E_1 is estimated to be ~1ps further facilitating population inversion. After passing through the bridging region electrons are injected into E_3 of the following repeat stage of the structure. The active region is left undoped since it can significantly broaden the lasing transition and increases the scattering from ionised impurities leading to a reduction in peak gain. However, the injector region which acts as an electron reservoir is doped.

Structures are generally distinguished by the radiative transition. If the wavefunctions of states E_3 and E_2 have a strong overlap then the transition is termed as being 'vertical'. The transition is said to be 'diagonal' if the overlap is reduced. The original three well design described previously has a radiative transition where two of the energy levels involved are mainly localised in different wells. This design is described as having a diagonal transition. Several other types of active region design have been

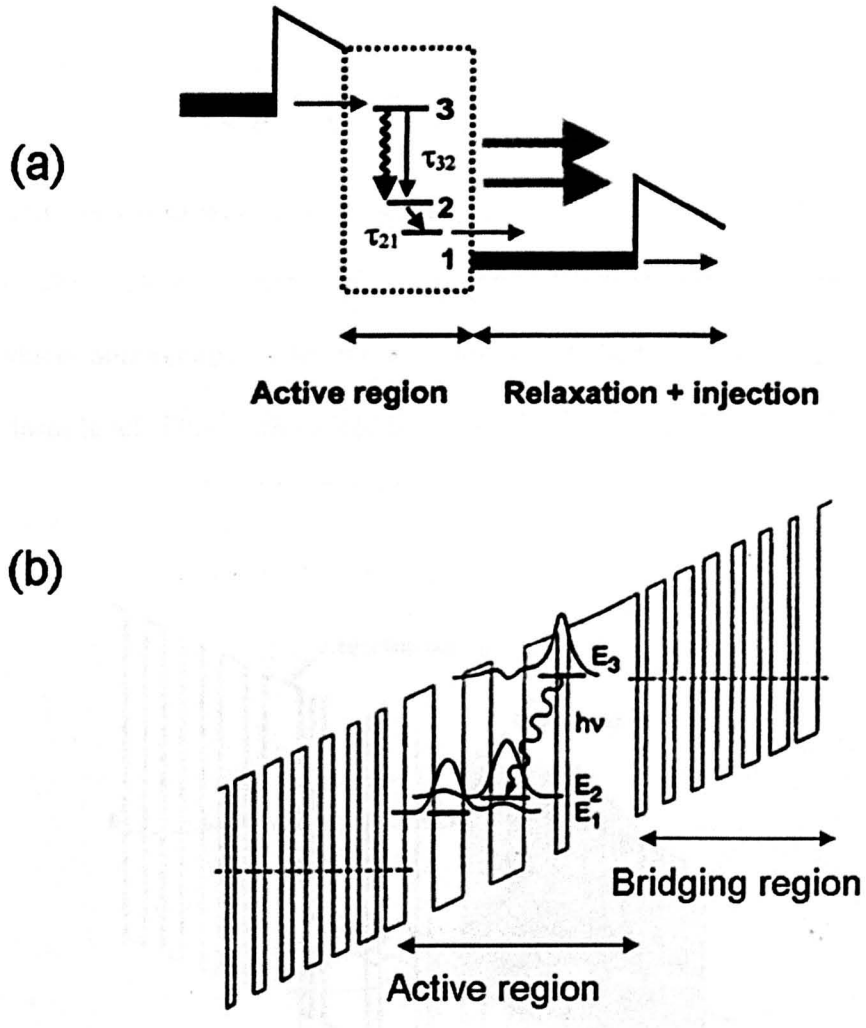

Figure 1.10 Schematic diagrams illustrating (a) the general concept of a QCL design (b) calculated conduction band diagram for one stage of the original three well active region QCL under positive bias conditions (electric field ~10^5 V/cm). Dashed lines are the effective conduction band edges of the electron injector. Electrons are tunnel injected into E_3 subband of active region. Images reproduced from [45].

utilised in QCL's. The properties of these designs are addressed in various publications [45] and will not be discussed, with the exception of the 'four-well' and 'bound-to-continuum' designs used in the devices presented in this thesis. All the

lasers with wavelength ~10μm presented in the thesis were based on a four-well active region design as described next.

1.5.3.1 Four quantum well active region

Four-well active regions incorporate a thin first quantum well in the active region. This introduces another energy level that is designed to be two phonon energies below the lower laser level. This is illustrated in the conduction band diagram in Fig. 1.11.

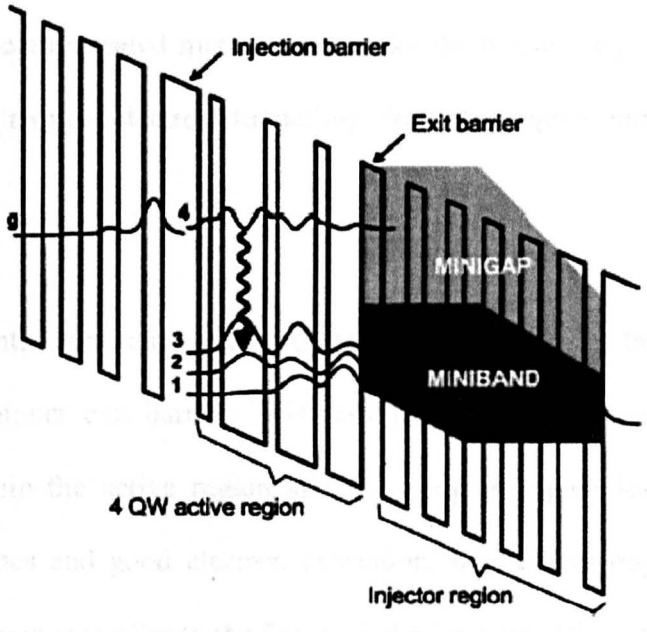

Figure 1.11 Schematic conduction band diagram of part of a four-well QCL active region including the relevant squared wavefunctions. Reproduced from [46].

The three lower states of the active region are designed to be separated by one phonon energy each enabling this 'two-phonon resonance' design to have a short intersubband electron scattering time. Keeping the lifetime of the lower laser level short further

helps to achieve population inversion. The upper and lower lasing states are the wave functions 4 and 3, respectively., A miniband facing the lower states of the active region is formed allowing efficient carrier escape from the ground state of the lasing transition. A minigap facing the upper state results in efficient carrier confinement. The ground state of the injector is represented by 'g'. Essentially, the extra energy level is used to keep the population of state 2 low, reducing the probability of thermal excitation of electrons back into the lower laser level. The additional thin well still maintains good electron injection from the bridging region into the upper lasing level and this design has resulted in devices with very high performance levels. In addition, the use of strain-compensated material can make the barrier height larger which can quite efficiently reduce electron tunnelling from the upper lasing state into the continuum.

The bound-to-continuum active region design is very similar to the four-well design but contains a thinner exit barrier. This results in a stronger coupling between the lower levels within the active region and the bridging region levels. This forms a continuum of states and good electron extraction, thus aiding population inversion. The upper laser level is similar to the four well design with efficient injection of electrons across the injection barrier, into the upper laser level.

All the devices presented in this thesis with emission wavelength λ ~10μm, were fabricated from material that was grown by MOVPE and had the same active region and cladding layer structures based on a four quantum well, two-phonon resonance design. Firstly, an n-doped InP substrate had 2.5μm of InP (Si-doped, n ~ $1x10^{17}$ cm^{-3}) grown, followed by 270nm of InGaAs (n ~ $6x10^{16}$ cm^{-3}). The 35-stage active region

with the nominal layer structure of (thicknesses in Angstroms); **35** / 23 / **8** / 66 / **9** / 64 / **9** / 58 / **20** / 40 / **12** / 40 / **12** / 40 / **13** / 39 / 17 / 38 / 21 / 35 / **22** / 35 was then grown. The underlined layers are doped ($n \sim 1\times 10^{17}$ cm^{-3}) and bold type refers to the $Al_{0.52}In_{0.48}As$ barriers. Normal type refers to the $In_{0.53}Ga_{0.47}As$ wells. Another 270nm of InGaAs (same as below active region) was grown on top of the active, followed by 3μm ($n \sim 1x10^{17}$ cm^{-3}) and 900nm ($n \sim 7x10^{18}$ cm^{-3}) of InP.

1.6 Plasma etching

A basic overview of plasma etching is given here. Good introductions to the technique can be found in references [47 - 48]. Plasma etching was originally introduced in the 1970's, mainly intended as a method to remove photoresist during fabrication of integrated circuits. The technique became more mature in the 1980's with the main technology being reactive ion etching (RIE). In the 1990's there was an introduction of new etch technologies like electron cyclotron resonance (ECR) and inductively coupled plasmas (ICP). The use of plasma technologies in the semiconductor industry has become widespread with plasma enhanced chemical vapour deposition (PECVD), plus RIE and ICP etching becoming invaluable tools in the compound semiconductor industry where sub-micron feature sizes and the need for deep, smooth, vertical etching of materials is a regular requirement.

A plasma is a partially ionised gas where free electrons collide with neutral atoms or molecules. As a result of this process the electron can remove one electron from the atom/molecule producing two free electrons and one ion. The result is also dependent on the energy of the incoming ion. It is also possible that a collision can end up producing other species, such as negative ions due to electron association, excited

molecules, neutral atoms and ions. Since excited electrons can return to their ground state, light is emitted. This light can be then be used to analyse the plasma since the wavelength of the light will be specific to each gas used in the process, as the energies between the electron states are well defined for each element.

1.6.1 Reactive ion etching (RIE)

Reactive ion etch systems have been a useful 'dry' etching technique for many years now, allowing the fabrication of small features in a wide range of materials used in the semiconductor industry. Capacitively coupled RF plasmas are still the most common plasmas used. A typical reactor will have power (frequency = 13.56MHz) applied to the lower or upper electrode. For the case shown in Figure 1.12, the lower electrode is powered and substrates are situated on this electrode. A 'dark sheath' is formed close to all surfaces of the reactor, electrodes and walls, so can be considered as a kind of dielectric or capacitor. If it is considered that the applied power is transmitted through a capacitor, we can see the reasoning for the term 'capacitively coupled RF plasma. The 'dark sheath' can usually be observed as a region of lower brightness than the bulk of the plasma. In this region there are less free electrons and they have lower energy. Therefore, there are less collisions, less excitations and so less photons being emitted.

In the frequency range of 1MHz-100 MHz the free electrons will gain significant energy (in the order of some hundred eV) unless they undergo a collision. This is because they are able to follow variations in the applied electric field. However, much heavier positive ions are effectively not influenced (simple case), and their energy (order of a few hundredths of an eV), is due to the thermal energy of the environment

Chamber pressure plays a large but complicated role in the etch characteristics of an etch recipe as explained later. In the range of a few mTorr to a few hundred mTorr, the electrons will travel much greater distances than ions. They will then have more. frequent collisions with the reactor walls and electrodes and as a consequence will be

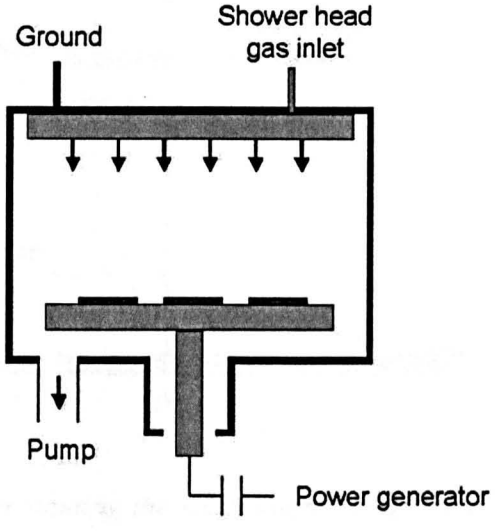

Figure 1.12 Simplified schematic diagram of a plasma etch reactor

removed from the plasma. Plasmas must remain neutral, so this removal of electrons would leave the plasma positively charged. Therefore, to maintain a neutral status, a DC electric field has to be formed in such a way so that electrons are repelled from the walls. As shown in Figure 1.12, the capacitor between the power generator and the electrode helps to form this. Electrons generated in the plasma will escape to the electrode and negatively charge the capacitor, during the first few cycles. Consequently, a negative DC bias voltage is formed on the electrode, which repels the electrons. The AC voltage then becomes superimposed on this negative DC voltage. A certain DC voltage is also needed to repel electrons from the walls but it can be

seen that the DC voltage of the Plasma will always be the most positive of all the DC voltages in the reactor as illustrated in Figure 1.13, showing how the DC voltage varies between the upper and lower electrode.

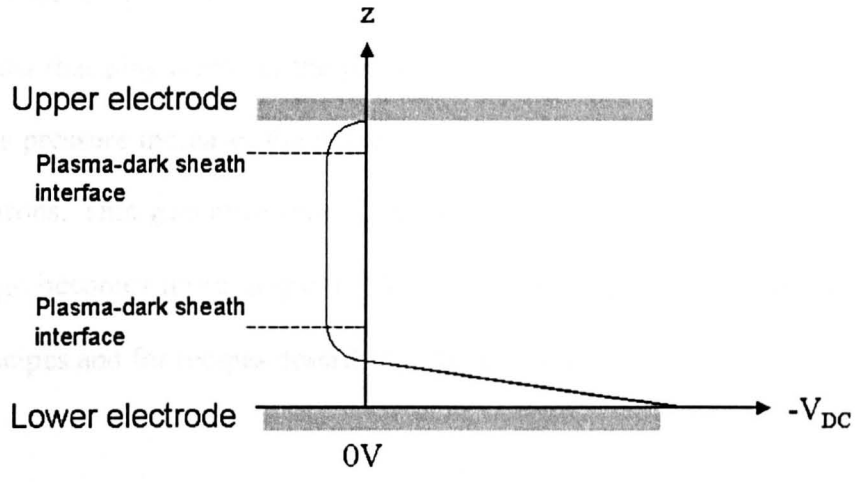

Figure 1.13 Diagram representing the DC voltage in a plasma reactor

1.6.2 Plasma Parameters

The dimensions of an etching reactor will influence the value of the DC voltage, but assuming these are fixed, it is the plasma process parameters (power, pressure, gas flow, etc.) that can be varied and have a significant influence on the DC voltage and etch characteristics. If we recall that the DC voltage is used to repel electrons, it follows that for higher electron densities and energies, the value of the DC voltage will be more negative.

1.6.2.1 Power

The influence of varying the power is quite straightforward. As power is increased the

density and energy of the free electrons increases as well. As a consequence the DC voltage will become more negative.

1.6.2.2 Pressure

The influence of pressure is a more complex than for power. There are a few mechanisms that play a role in the process. In the pressure range of (1 mTorr ~ 100 mTorr), as pressure increases the plasma becomes denser and more molecules collide with electrons. This generates more free electrons and positive ions. As a result the DC voltage becomes more negative. This pressure range is typical for most Plasma etching recipes and for recipes described later in this thesis.

An interesting point, for even higher pressures than mentioned above, is that a further increase in pressure will have an opposite effect. The density of species will increase, meaning that the mean free path of the colliding electrons will be shorter. They will gain less energy between collisions and there will be a reduction in the formation of electron-positive ion pairs. The DC voltage will then become less negative.

1.6.2.3 Gases and gas flows

If all other parameters in a process are kept constant, then it is the electronegativity of the gases that will determine the DC voltage. Put simply, the electronegativity of an atom or molecule is its ability to attract electrons. Group VII gases such as Fluorine and Chlorine are very electronegative since they are very prone to absorbing free electrons. They decrease the density of the free electrons in the plasma and increase the number of negative ions. Therefore, the DC voltage of a plasma using a less electronegative gas such as Nitrogen, would be considerably more negative. The

absolute gas flows do not generally affect the DC voltage. However, if there is a mixture of gases, The relative flows may have an effect. If a small flow of a low electronegative gas (e.g Nitrogen) is added, the DC voltage tends to become rapidly more negative.

1.6.3 Inductively coupled plasma (ICP) etching

Inductively coupled plasma (ICP) etching is a very useful technique for achieving smooth, vertical etching with the capability of faster etch rates than RIE. A simplified ICP etch system is shown in Fig.1.14. In this configuration, the plasma is mainly generated by inductive coupling. This is due to an RF voltage being applied to the water cooled RF coil, resulting in an RF current which induces a magnetic field in the reactor. Therefore, the wall must not be magnetically conductive. There is also a separate table generator that can apply a bias voltage. However, in contrast to the RIE configuration mentioned previously, this is not used to generate the plasma but is for increasing the ion bombardment on the substrate. By utilising this extra facility, the process can be optimised since it is possible to independently control the plasma density and the energy of the ions that are incident on the substrate. Since many fabricated devices require etched features with high aspect ratios, the ions must be incident on the substrate at near perpendicular angles. This means very few collisions should take place in the dark sheath so low pressures are required for this. High density plasmas can be obtained at low pressures (~ 2 mTorr) meaning that fast etch rates (1-2 microns/min) are easily achievable. However, the plasma may need to be 'struck' at a higher pressure (~ 8 mTorr) and then reduced.

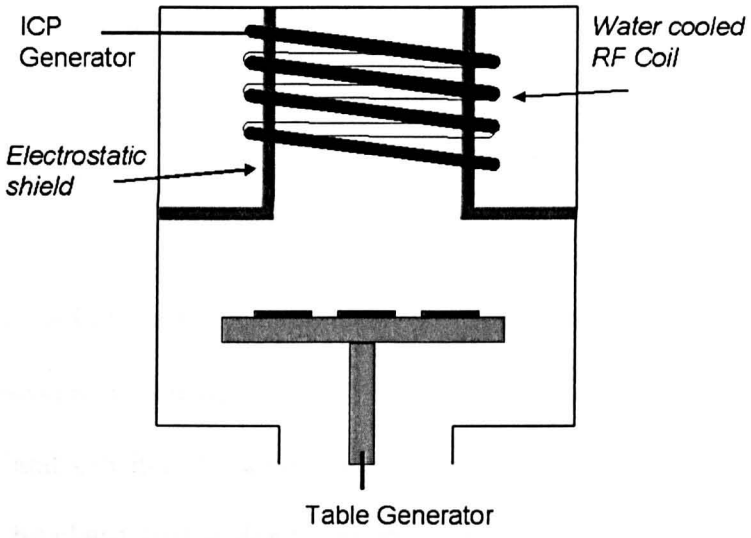

Figure 1.14 Simplified schematic diagram if an inductively coupled plasma (ICP) reactor

1.6.4 Etching mechanisms

The basic mechanisms described in this section are applicable to both RIE and ICP etching techniques. A plasma etching process is typically a chemical reaction that takes place between a solid atom (from a layer on the substrate that is being etched) and a gas atom, which forms a molecule. This molecule is then removed from the substrate. However, there is a DC bias voltage as explained previously, which does involve a physical sputtering or 'bombardment' component. The main mechanisms are :

- Reactive particle is formed
- Reactive particle arrives at surface to be etched
- Adsorption of reactive particle at surface
- Chemical bond is formed

- Product molecule is formed
- Desorption of product molecule
- Product molecule removed from reactor through the exhaust.

The etch rate of a film on the substrate can be thought to be limited by the slowest mechanism mentioned above. Several mechanisms can be influenced by ion bombardment and can help to speed up the vertical etch rate and achieve vertical sidewalls. Ion bombardment is due to positive ions arriving at the interface between the dark sheath and the plasma where they are then accelerated towards the substrate by the negative DC voltage. The ion bombardment can be utilised to increase the vertical etch rate whilst the horizontal etch rate remains constant, helping to achieve vertical etch profiles. The ion bombardment can do this for example, by speeding up the removal of the etch product molecules by supplying the required energy for them to be removed from the etch layer surface. These product molecules may remain on the sidewalls slowing down chemical etching on those surfaces and so anisotropic etching occurs.

1.6.5 RIE and ICP – a comparison

For some applications ICP etching has shown itself to be advantageous over RIE. Although the initial cost of an ICP etcher is usually more expensive, the main advantages in terms of process engineering are:

- To achieve a dense plasma with RIE, an increase in power will also mean an increase in ion energy. With ICP etching the plasma density and ion bombardment can be independently controlled allowing mainly chemical etches with little ion

bombardment.

- Since ion bombardment can be controlled with ICP, it is possible to achieve recipes with faster or equally fast etch rates but without inducing as much 'damage' to the material as with RIE. This can be crucial when fabricating interband semiconductor lasers for example, where electron-hole recombination centres can result and decrease the performance and reliability of the lasers.

- ICP systems are good for etching vertical sidewall profiles since typically lower pressures can be used whilst still achieving a higher density plasma than for RIE.

1.7 Laser spectrum measurement

1.7.1 Fourier transform spectroscopy

The apparatus of a Fourier transform (FTIR) spectroscopy system is derived from the well known Michelson interferometer as illustrated in Fig.1.15. The advent of FTIR spectroscopy has considerably improved the speed of measurements in the infrared region of the spectrum. A collimated beam of radiation from a source is directed to the interferometer. The beam splitter B is a plate made of suitably transparent material (e.g KBr) which sends half the radiation to mirror M_1 and half to M_2. The radiation from both mirrors travels back along the same path and recombine to a single beam at B. Monochromatic light from the source will then show constructive and destructive interference depending on the path lengths of B-M_1 and B-M_2. For identical lengths (or if they differ by an integral number of wavelengths) there is constructive interference and a bright beam leaving B. For a half number of wavelengths the

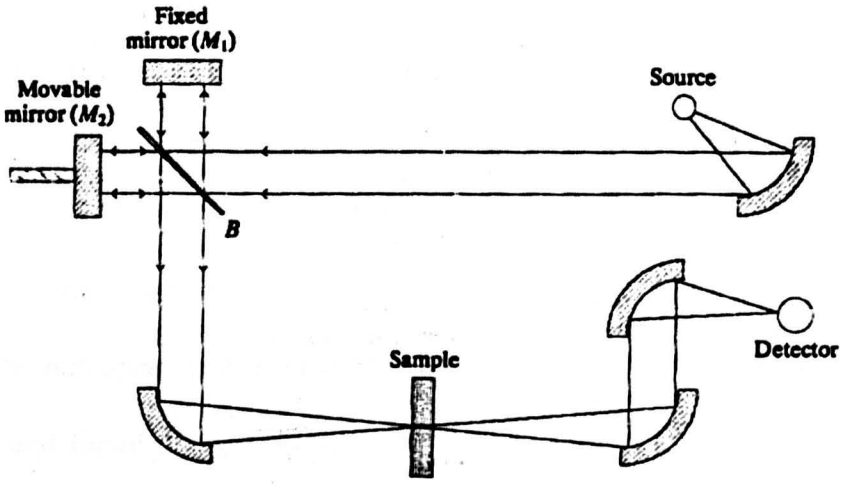

Figure 1.15 Schematic diagram of a Fourier transform spectrometer (based on the Michelson interferometer). For laser spectrum measurements no sample is placed in the beam path. Reproduced from [49]

beams will destructively interfere. By moving M_2 smoothly and continuously towards or away from B, a detector will see a modulation of the radiation intensity. If two separate frequencies were emitted by the source then the interference pattern (beat pattern) of the two frequencies would overlay the interference caused by M_1 and M_2. The detector will see a more complicated intensity fluctuation. However, Fourier transforming the resultant signal will rapidly obtain the original frequencies and intensities emitted by the source. FTIR spectroscopy offers several advantages over conventional dispersive techniques, especially in the mid-infrared. All wavelengths are measured simultaneously meaning that a single spectrum can be measured in just a few seconds. The signal to noise ratio (*S/R*) of the spectrum can be improved by increasing the number of measurements (N) scanned ($S/R \propto \sqrt{N}$) and an FTIR system will also show a higher optical throughput than a dispersive system since it

does not require use of an optical slit which severely limits the amount of energy passing through the system. This results in improved ability to detect weak signals, especially where the detector is the limiting source of noise in the system.

The spectra measured and presented in this thesis were obtained using a Bruker IFS66V vacuum spectrometer (resolution = 0.2 cm^{-1}) with KBr beamsplitters (λ up to ~27 μm) and liquid nitrogen cooled HgCdTe detectors (cut off wavelength, λ ~13 μm). The previous description of the operation of FTIR systems concentrated on a continuous-scan technique where the movable mirror moves at a constant linear velocity. This modulates the infrared emission at a characteristic Fourier frequency.

When the source light is modulated (as with pulsed operation of a QCL) the device modulation can be incorporated into the spectral data. To avoid this, the device modulation frequency should typically be at least ten times greater than the highest Fourier frequency of interest. This would limit the range of frequencies at which QCLs presented in this thesis can be driven to approximately 40 kHz and above. Step-scan FTIR spectroscopy (moving the mirror in discrete steps rather than at a constant velocity) will overcome this issue. Since the measurements are taken with a stationary mirror, the Fourier frequency is zero. Thus, eliminating the effect on the transform process. Typically, the output from the detector will be fed into a lock-in amplifier and combined with a reference signal obtained from the device driver electronics. The output from the lock-in would then be fed back to the A/D converter within the FTIR system. Software controlling the FTIR can adjust the time taken to pause at each mirror position before commencing the recording of measurements, to account for the time constant of the detection electronics. Since the stabilisation delay is carried out

only once at each mirror position, a significant time saving is possible over the equivalent method of recording several scans and averaging (continuous-scan FTIR)

1.8 Grating period measurement

The grating period is a critical parameter in the design of distributed feedback lasers and plays a major role in determining the single mode frequency of the laser. A quick, non-destructive and accurate measurement of a semiconductor wafer sample is extremely useful for the fabrication of these devices and for accurately measuring other device parameters. Due to the small linewidth of the gratings for near to mid-infrared lasers (typically < 1μm), conventional optical microscopy does not have suitable resolution. In general, the grating will first be defined in photoresist on the surface of a sample. A scanning electron microscope (SEM) may be used to measure the grating period but can require a bar to be cleaved from the sample. This can be costly, especially if several exposures of the photoresist grating are required. Furthermore, the cost of an SEM can be prohibitively expensive. The gratings for many of the devices in this thesis have been exposed by contact lithography using laser written masks. The advantage is that every exposure will produce a grating with the same period. However, there is usually some tolerance in the grating period specified to the mask manufacturer and the actual mask supplied. This required measurement of the quartz mask which can be problematic if using an SEM.

In this thesis, a combination of SEM and laser measurements was used to measure the grating periods. Figure 1.16 illustrates the laser based measurement set-up. A He-Ne laser (λ = 632.8nm) was used with a rotation stage and a silicon detector. The laser light is reflected back from the grating into diffraction orders. The angle (θ) between

the 1^{st} and -1^{st} orders can then be used to calculate the grating period (Λ) using equation 1.5 [50].

$$(\Lambda = \lambda / \sin\theta) \qquad (1.5)$$

The resolution of the rotation stage is stated by the manufacturer to be 1 arc min. Therefore, the calculated measurement error for a grating period of 1.615μm is (+/- 0.003μm).

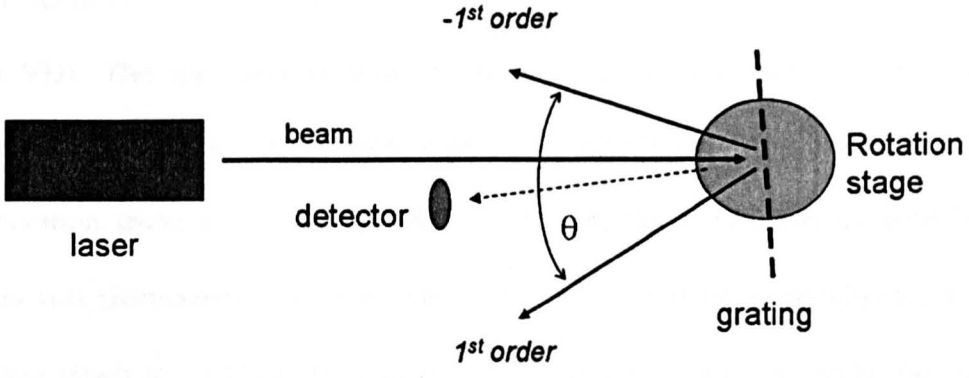

Fig. 1.16 Schematic diagram of the laser based set-up for grating period measurements. The first order diffraction beams are separated by angle θ (measured by the rotation stage) and detected by a silicon detector sensitive at the He-Ne laser wavelength. Zero order beam is represented by the dashed line.

1.9 Standard laser fabrication

After the epitaxial growth, the samples were processed into ridge waveguides. The basic fabrication steps given here are for wet chemically etched Fabry-Perot ridge laser devices. The dry etched devices follow an identical process flow but the ridge is plasma etched as described further in the relevant experimental chapters. The grating

process for the distributed feedback lasers is also described in each experimental chapter.

Since the laser ridges were typically >10μm wide, the wafer patterning was carried out with standard contact photolithography using Suss MJB3 mask aligners and standard broadband photoresists. The wet chemical etchant was a (1:1:1) hydrobromic acid : acetic acid : potassium dichromate solution which is non-selective, and has similar etch rate for all layers in the QCL structures used. For an insulating layer we used 500nm of Si_3N_4 deposited by plasma enhanced chemical vapour deposition (PECVD). The top opening was etched by reactive ion etching (RIE) under a CHF_3/O_2 atmosphere. The top contact of Ti/Au (20/200 nm) was deposited by thermal evaporation using a photolithographic lift-off procedure and a thick gold layer of ~3μm was electroplated on to the top contact.. The 350μm thick substrate was then thinned down to ~150μm by mechanical polishing in order to make the cleaving easier and with the further advantage of reducing device thermal resistance. The Ti/Au (20/200 nm) bottom side contact was again thermally evaporated and annealed at 340°C. The samples were then cleaved in to laser bars / chips and soldered to heat-sinks (epitaxial-layer up) using indium solder.

1.10 References

[1] R. N. Hall, G. E. Fenner, J. D. Kingsley, T. J. Soltys, and R. O. Carlson.: 'Coherent light emission from GaAs junctions', Phys. Rev. Lett. 9, 366, 1962

[2] M. I. Nathan, W. P. Dumke, G. Burns, F. H. Dill, Jr., and G. Lasher.: 'Stimulated emission of radiation from GaAs p-n junctions, Appl. Phys. Lett. 1, 62, 1962

[3] N. Holonyak, Jr. and S. F. Bevacqua.: 'Coherent (visible) light emission from Ga(As1−xPx) junctions', Appl. Phys. Lett. 1, 82, 1962

[4] T. M. Quist, R. H. Rediker, R. J. Keyes, W. E. Krag, B. Lax, A. L. McWhorter, andH. J. Zeiger, "Semiconductor maser of GaAs", Appl. Phys. Lett. 1, 91, 1962

[5] R. F. Kazarinov and R. A. Suris.: 'Possibility of the amplification of electromagnetic waves in a semiconductor superlattice', Sov. Phys. Semicond. 5, 707, 1971

[6] [81] B. Williams, S. Kumar, Q. Hu, and J. Reno.: 'Operation of terahertz quantum-cascade lasers at 164 K in pulsed mode and at 117 K in continuous-wave mode', Opt. Express13, 3331, 2005

[7] J. F. Butler, A. R. Calawa, R. J. Phelan, Jr., T. C. Harman, A. J. Strauss, and R. H. Rediker.: 'PbTe diode laser', Appl. Phys. Lett. 5, 75, 1964

[8] G. P. Agrawal, N. K. Dutta.: 'Semiconductor lasers', second edition, KAP, 2000

[9] C. Lin, M. Grau, O. Dier, and M.-C. Amann.: 'Low threshold room-temperature continuous-wave operation of 2.24-3.04 μm GaInAsSb / AlGaAsSb quantum-well lasers', Appl. Phys. Lett. 84, 5088, 2004

[10] Sarnoff Corporation, Princeton, NJ, USA.

[11] J. R. Meyer, C. A. Hoffman, F. J. Bartoli, and L. R. Ram-Mohan.: 'Type-II quantum well lasers for the mid-wavelength infrared', Appl. Phys. Lett. 67, 757, 1995

[12] C. L. Canedy, W. W. Bewley, C. S. Kim, M. Kim, J. R. Lindle, I. Vurgaftman,

and J. R. Meyer.: 'cw midinfrared "W" diode and interband cascade lasers', J. Vac. Sci. Technol. B 24, 1613, 2006

[13] C. L. Canedy, W. W. Bewley, J. R. Lindle, I. Vurgaftman, C. S. Kim, M. Kim, and J. R. Meyer, "High-power continuous-wave midinfrared type-II "W" diode lasers', Appl. Phys. Lett. 86, 211105, 2005

[14] R. Q. Yang.: 'Infrared laser based on intersubband transitions in quantum wells', Superlatt. Microstruct. 17, 77, 1995

[15] J. R. Meyer, I. Vurgaftman, R. Q. Yang, and L. R. Ram-Mohan.: 'Type-II and type-I interband cascade lasers', Electron. Lett. 32, 45, 1996

[16] C.J. Hill, C.M. Wong, B. Yang, and R.Q. Yang, "Type-II interband cascade lasers emitting at wavelengths beyond 5.1 μm", Electron. Lett. 40, 878 (2004).

[17] W. W. Bewley, J. A. Nolde, D. C. Larrabee, C. L. Canedy, C. S. Kim, M. Kim, I. Vurgaftman, and J. R. Meyer.: 'Interband cascade laser operating cw to 257K at λ=3.7μm', Appl. Phys. Lett. 89, 161106, 2006

[18] Maxion Technologies Inc., Maryland, USA.

[19] W. H. Ng, E. A. Zibik, M. R. Soulby, L. R. Wilson and J. W. Cockburn.: 'Broadband quantum cascade laser emitting from 7.7 to 8.4μm operating up to 340K', Journal of Applied Physics 101, 046103, 2007

[20] S. K. Ray, K. M. Groom, R. Alexander, K. Kennedy, H. Y. Liu, M. Hopkinson, and R. A. Hogg.: 'Design, growth, fabrication, and characterization of InAs/GaAs 1.3 μm quantum dot broadband superluminescent light emitting diode', Journal of Applied Physics 100, 103105, 2006

[21] Y. Arakawa and H. Sakaki.: Multidimentional quantum well laser and temperature dependence of its threshold current', Appl. Phys. Lett. 40, pp. 939-941, 1982

[22] K.S. Mobarhan.: 'Test and Characterisation of Laser Diodes: Determination of Principal Parameters', Application notes, Newport Corp.

[23] J. Faist, F. Capasso, D. L. Sivco, C. Sirtori, A. L. Hutchinson, and A. Y. Cho.: 'Quantum cascade laser', Science, 264, pp. 553-556, 1994

[24] J. Faist, F. Capasso, C. Sirtori, D. L. Sivco, J. N. Baillargeon, A. L. Hutchinson, S. N. G. Chu, and A. Y. Cho.: 'High power mid-infrared ($\lambda \sim 5$ μm) quantum cascade lasers operating above room temperature', Appl. Phys. Lett. 68, 3680, 1996

[25] J. Faist, F. Capasso, D. L. Sivco, A. L. Hutchinson, S.-N. G. Chu, and A. Y. Cho.: 'Short wavelength (λ ~3.4 μm) quantum cascade laser based on strained compensated InGaAs/AlInAs', Appl. Phys. Lett. 72, 680, 1998

[26] C. Gmachl, F. Capasso, A. Tredicucci, D. L. Sivco, A. L. Hutchinson, and A. Y. Cho, "Long wavelength ($\lambda \sim 13$ μm) quantum cascade lasers", Electron. Lett. 34, 1103, 1998

[27] G. Scamarcio, F. Capasso, C. Sirtori, J. Faist, A. L. Hutchinson, D. L. Sivco, and A.Y. Cho.: 'High-power infrared (8-micrometer wavelength) superlattice lasers', Science, 276, 773, 1997

[28] A. Tredicucci, F. Capasso, C. Gmachl, D. L. Sivco, A. L. Hutchinson, and A. Y. Cho.: 'High performance interminiband quantum cascade lasers with graded superlattices', Appl. Phys. Lett. 73, 2101, 1998

[29] R. Colombelli, F. Capasso, C. Gmachl, A. L. Hutchinson, D. L. Sivco, A. Tredicucci, M. C. Wanke, A. M. Sergent, and A. Y. Cho,.: 'Far-infrared surface-plasmon quantumcascade lasers at 21.5 μm and 24 μm wavelengths', Appl. Phys. Lett. 78, 2620, 2001

[30] J. Faist, M. Beck, T. Aellen, and E. Gini.: 'Quantum-cascade lasers based on a bound-to- continuum transition', Appl. Phys. Lett. 78, 147, 2001

[31] D. Hofstetter, M. Beck, T. Aellen, and J. Faist.: 'High-temperature operation of distributed feedback quantum-cascade lasers at 5.3 μm', Appl. Phys. Lett. 78, 396 2001

[32] M. Beck, D. Hoffstetter, T. Aellen, J. Faist, U. Oesterle, M. Ilegems, E. Gini and H. Melchior.: 'Continuous-wave operation of a mid-infrared semiconductor laser at roomtemperature', Science 295, 301, 2002

[33] J. S. Roberts, R. P. Green, L. R. Wilson, E. A. Zibik, D. G. Revin, J. W. Cockburn, and R. J. Airey.: 'Quantum cascade lasers grown by metalorganic vapour phase epitaxy', Appl. Phys. Lett. 82, 4221, 2003

[34] R. P. Green, A. Krysa, J. S. Roberts, D. G. Revin, L. R. Wilson, E. A. Zibik, W. H. Ng, and J. W. Cockburn.: 'Room-temperature operation of InGaAs/AlInAs quantum cascade lasers grown by metalorganic vapor phase epitaxy', Appl. Phys. Lett. 83, 1921, 2003

[35] J. Devenson, D. Barate, O. Cathabard, R. Teissier, and A. N. Baranov, "Very short wavelength (λ=3.13.3 μm) quantum cascade lasers", Appl. Phys. Lett. 89, 191115 (2006).

[36] D. G. Revin, L. R. Wilson, E. A. Zibik, R. P. Green, J. W. Cockburn, M. J. Steer, R. J. Airey, and M. Hopkinson, "InGaAs/AlAsSb quantum cascade lasers", Appl. Phys. Lett. 85, 3992, 2004

[37] S. Y. Zhang, D. G. Revin, J. W. Cockburn, K. Kennedy, A. B. Krysa, M. Hopkinson.: 'λ ~3.1μm room temperature InGaAs/AlAsSb/InP quantum cascade lasers', Appl. Phys. Lett. 94, 031106, 2009

[38] A. Evans, S. R. Darvish, S. Slivken, J. Nguyen, Y. Bai, and M. Razeghi.: 'Buried heterostructure quantum cascade lasers with high continuous-wave wall plug

efficiency', Appl. Phys. Lett. 91, 071101, 2007

[39] J. Faist, C. Gmachl, F. Capasso, C. Sirtori, D. L. Sivco,, J. N. Baillargeon, A. Y. Cho.: 'Distributed feedback quantum cascade lasers', Appl. Phys. Lett. 1997, 70, 20, pp. 2670-2673

[40] J. Yu, S. Slivken, S. Darvish, A. Evans, B. Gokden, and M. Razeghi.: 'High-power, room-temperature, and continuous-wave operation of distributed-feedback quantum-cascade lasers at λ~4.8μm', Appl. Phys. Lett. **87**, 041104, 2005

[41]. R. Darvish, S. Slivken, A. Evans, J. S. Yu, and M. Razeghi.: 'Room-temperature, high-power, and continuous-wave operation of distributed-feedback quantum-cascade lasers at λ~9.6 μm', Appl. Phys. Lett. **88**, 201114, 2006

[42] E. Mujagić, L. K. Hoffmann, S. Schartner, M. Nobile, W. Schrenk, M. P. Semtsiv, M. Wienold, W. T. Masselink, and G. Strasser.: 'Low divergence single-mode surface emitting quantum cascade ring lasers', Appl. Phys. Lett., 93, 161101, 2008

[43] J. W. Rolf.: 'Modern Physics' Wiley and Sons, 1994

[44] R. P. Green.: 'Physics and Technology of Intersubband Transitions in III-V Semiconductor Heterostructures', PhD thesis, University of Sheffield, 2005

[45] H.C. Liu, F. Capasso.: 'Intersubband Transitions in Quantum Wells: Physics and Device Apllications II, Semiconductors and semimetals, volume 66, Academic press, 2000

[46] D. Hofstetter, M. Beck, T. Aellen, J. Faist.: 'High Temperature operation of distributed feedback quantum-cascade lasers at 5.3μm', Appl. Phys. Lett., 78, 4, 2001

[47] D.M. Manos, D. L. Flamm;: 'Plasma Etching: An introduction', Academic Press, 1989

[48] Liebermann, Lichtenberg.: 'Principles of Plasma Discharges and Materials Processing', Wiley and Sons, 1994

[49] C. N. Banwell, E. M. McCash.: 'Fundamentals of Molecular Spectroscopy', fourth edition, McGraw-Hill, 1994

[50] E. Hecht.: 'Optics', second edition, Addison-Wesley, 1987

Chapter 2 - Waveguide Modelling of Distributed Feedback Quantum Cascade Lasers

2.1 Introduction

This chapter describes the theory and the methods used to accurately and quickly model the semiconductor waveguides presented in this thesis. Being able to accurately model the optical modes propagating in a waveguide is an invaluable tool when designing a distributed feedback (DFB) semiconductor laser diode. A greater understanding of the optical mode behaviour can significantly reduce experimental time and facilitate in the design of more advanced devices. The modelling of the waveguides is assisted by the use of a commercial software package [1] providing quick calculations with good agreement to experimental results.

Distributed feedback lasers were first worked on in the early 1970's [2, 3] but it wasn't until the mid 1970's that DFB diode lasers were demonstrated [4]. The research towards dynamic single mode semiconductor lasers was aimed at investigating lasers for tight mode control during high speed direct modulation. Alternative approaches included, cleaved coupled-cavity lasers, external cavity lasers and distributed Bragg reflector (DBR) lasers. However, DFB lasers have proved to be a cost effective solution becoming key components in high speed communication systems. Extensive research during the 1980's resulted in DFB lasers becoming widely used in commercial systems by the 1990's. DFB lasers are different to conventional lasers because the feedback mechanism is provided by distributed Bragg scattering from periodic variations of the refractive index, and/or gain (loss) along the waveguide. This differs from conventional semiconductor lasers where the feedback

is provided by discrete end cavity reflectors (cleaved crystal facets). Coupled radiation from a periodic structure (grating) in a waveguide is utilised in a DFB laser to achieve a high level of spectral selection (and potentially single transverse mode operation) with narrow emission linewidth. When the grating period is approximately an integral multiple of half the propagating wavelength in the waveguide (the Bragg condition), strong coupling will exist between the propagating wave and an identical wave propagating in the opposite direction. The degree to which these counter propagating waves transfer energy (Bragg scattering) and hence the amount of feedback (per unit length) provided by the grating is given by the so-called "coupling coefficient". The threshold gain (threshold current) and other characteristics of a DFB laser depend on the magnitude of the coupling coefficient and so control over this value is important. The numerical value of the coefficient depends on the grating parameters (i.e. depth, period and shape).

The interactions between electro-optic and thermal phenomena in a laser diode are often non-linear. A model which successfully describes the system in full detail may be too complex. For DFB lasers, the coupled wave theory [2] is a good balance between a simplistic model and one which provides sufficient accuracy. Two equations corresponding to the forward and backward propagating waves are solved, subject to boundary conditions, specific to the device. Much work has followed the original paper by Kogelnik and Shank, although often with slightly different notation. The original paper presented an analysis of laser action in a periodic structure with approximations given for both index and gain periodicities. Non-linear effects such as gain saturation were not considered and it was intended to be meaningful only near threshold and for "weak" gratings (i.e. small dielectric constant differences in the

grating region). Work generally focused on index-coupled devices but a potential improvement in device performance and single-mode yield meant that gain (loss) coupled devices generated significant interest [5, 6]. Later work dealt with the more common case where there is both index and loss coupling and is commonly referred to as being complex-coupled [7]. This is generally the case for DFB quantum cascade lasers due to the relatively high optical losses in many materials at mid-infrared wavelengths.

An alternative approach to the work by Kogelnik and Shank [2] by Wang [8], first obtains the Bloch-type eigensolutions by assuming an infinitely long structure, then applying the solutions to a specific device. Both methods were shown to be equivalent by Yariv [9]. When surface gratings are employed with the contact metal deposited on top (e.g. gold) there is a very large refractive index difference between the semiconductor and gold in the mid-infrared. This very "strong" grating may lead to an underestimation of the coupling strength using the Kogelnik and Shank method. This is addressed by Finger *et al* [10], where metal surface gratings for vertical emitting QC lasers are analysed.

In this chapter the emphasis will be on using the commercially available software (based around a fully vectorial waveguide solver, implementing a film mode matching method [1, 11]) to create a model which accurately predicts the propagation of optical modes in the semiconductor waveguide structures and facilitates the calculation of the coupling coefficients and emission wavelength of the lasers. This is applied to each type of quantum cascade DFB discussed in this thesis, with relevant results from the modelling presented and discussed.

2.2 Semiconductor ridge waveguide

The laser devices presented in this thesis are all ridge waveguide structures where the ridge has been fabricated by either wet chemical or 'dry' plasma etch processes. The various epitaxial layers and their refractive indices are used within the waveguide modelling software to allow the characterisation and visual representation of the propagating optical modes in the waveguide. In Fig. 2.1 the refractive index and optical mode intensity profiles (vertical direction) are plotted for a typical quantum cascade ridge laser structure ($\lambda \sim 10\mu m$) as used in this thesis. The structure takes an average refractive index value for the active core region (AlInAs barriers, InGaAs wells) but the cladding layers are specified individually.

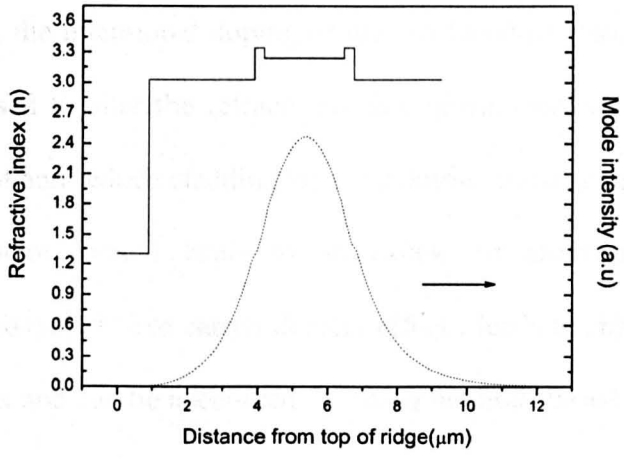

Figure 2.1 R*efractive index and fundamental TM mode intensity profiles (vertical direction) of a quantum cascade ridge laser structure ($\lambda \sim 10\mu m$).*

2.2 Refractive index and the free carrier density effect.

The refractive indices of the layers making up the dielectric waveguide play an important role in the optimisation of the semiconductor laser performance. The active core region will have a larger value of refractive index than the cladding regions so

that the optical mode is confined as much as possible to the active region where there is gain. Significantly, for DFB lasers, the effective refractive index value of the propagating mode and the amount of coupling of the optical mode to the grating will depend on the refractive index values of the material layers. Therefore, emission wavelength (Bragg condition) and optical performance are dependent on the refractive index values. Typically, the designed thickness of the cladding layers will increase with laser wavelength. This is to keep the optical field strength (at the metal contact on top of the cladding) at an acceptable level. However, as the wavelength is increased into the mid-infrared region the thickness of the cladding layers would become impractical from an epitaxy and fabrication point of view.

As explained later, the intentional doping of the semiconductor materials in the laser structure can be used to alter the refractive index of the cladding layers to improve optical confinement and reduce cladding layer thickness. Introducing donor impurities to the semiconductor crystal leads to an excess of electrons and absorption mechanisms. The so called 'free carrier density effect', leads to changes in absorption and refractive index and can be accounted for using methods based on the Drude free-electron model.

The electric permittivity is a constant of proportionality between electric displacement and electric field intensity. The permittivity of free space (ε_0) is approximately equal to 8.85 x 10^{-12} F/m. The relative permittivity (ε_r) is typically used, and is also known as the dielectric constant,

$$\varepsilon_r = \varepsilon / \varepsilon_0 \qquad (2.1)$$

where the permittivity of the material is represented by (ε).

The refractive index (n) of a medium is a measure of the reduction in the speed of light inside the medium. It is related to the dielectric constant by

$$n = \sqrt{(\varepsilon_r \mu_r)} \tag{2.2}$$

where μ_r is the relative permeability. For optical frequencies $\mu_r \approx 1$.

In reality, materials have a loss or gain that can be expressed by a complex (real and imaginary parts) and frequency dependent permittivity. In a non-magnetic medium with a relative permeability equal to 1, the dielectric constant (ε_r) is the square of the complex refractive index (n')

$$n' = n + ik \tag{2.3}$$

$$\varepsilon_r = \varepsilon_1 + i\varepsilon_2 = (n + ik)^2 \tag{2.4}$$

In the equations above, the extinction coefficient (k) indicates the amount of absorption loss of the wave propagating through the waveguide. Both n and k are frequency dependent. In general, as wavelength increases, the real part (n) will decrease. The absorption coefficient (α) is commonly used, with units in (cm^{-1}), and is related to the extinction coefficient as shown below.

$$\alpha = 4\pi k / \lambda \tag{2.5}$$

The plasma frequency of a doped semiconductor material is a natural mode of oscillation of the carrier (typically electron) 'gas'. The mode is sometimes referred to as the plasma mode or plasmon. The optical properties of the material depend on the doping concentration level of the semiconductor material since the plasma frequency is a function of the concentration of free carriers (typically electrons) in the material. The plasma frequency (ω_p) is related to the free carrier concentration (N) (i.e., the doping level), the electron charge (e), the free space permittivity (ε_0), and free carrier effective mass (m^*) by the equation below.

$$\omega_p = (N e^2 / \varepsilon_0 m^*)^{1/2} \tag{2.6}$$

The real and imaginary parts of the complex dielectric constant can be written as,

$$\varepsilon_1 = \varepsilon_\infty - (\omega_p^2/\omega^2) \tag{2.7}$$

$$\varepsilon_2 = (\omega_p^2 / \omega^2)(1 / \omega\tau) \tag{2.8}$$

where $\omega = 2\pi c / \lambda$, is the emission frequency. ε_∞ is the high-frequency lattice dielectric constant and τ is the electron scattering time. For intraband processes a value of $\tau \sim 0.1$ps is assumed.

Using the previous equations the real and imaginary parts of the refractive index can be written as,

$$n = [(\varepsilon_1^2 + \varepsilon_2^2)^{1/2} / 2 + (\varepsilon_1 / 2)]^{1/2} \tag{2.9}$$

$$k = [(\varepsilon_1^2 + \varepsilon_2^2)^{1/2} / 2 - (\varepsilon_1 / 2)]^{1/2} \tag{2.10}$$

From these equations the doping concentrations that are required to optimise the laser design for optical confinement and absorption can easily be determined. In Fig. 2.2 the calculated values of n and k are shown for InP and InGaAs materials for a range of carrier concentrations, similar to the doping levels used in the quantum cascade structures (λ=10μm) used in this thesis. Effective electron mass and high frequency dielectric constant values are taken from reference 12. It can be seen from these plots that the absorption loss and real part of the refractive index are strongly dependent on the free carrier density (doping levels) in the semiconductor material.

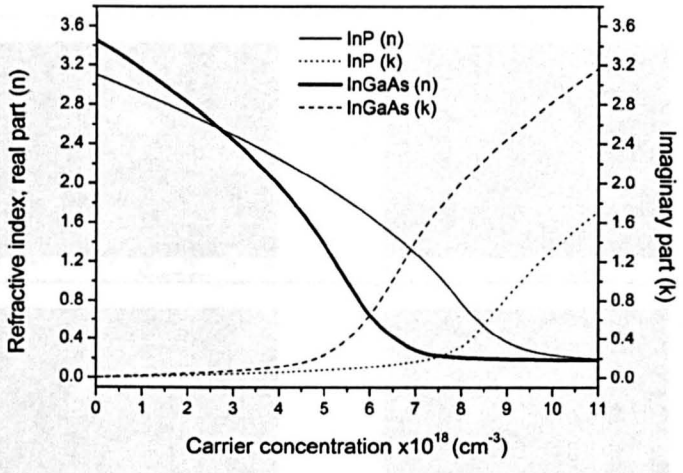

Figure 2.2 *Calculated refractive index (real and imaginary parts) for InP and InGaAs for a range of free carrier concentrations. (λ=10μm).*

The propagation constant β of a mode in a waveguide, determines how the phase and amplitude of the light with a certain frequency varies along the direction of propagation. The effective refractive index, n_{eff} (sometimes referred to as the modal index) does not only depend on wavelength but also on the mode propagating in the waveguide and is related to the propagation constant (β).

$$\beta = n_{eff}(2\pi / \lambda) \qquad (2.11)$$

The effective refractive index can be a complex quantity and is not (as sometimes assumed) just a weighted average of the fraction of the optical mode power overlapping with the core and cladding layers in the waveguide. The effective refractive index values for higher order transverse modes propagating in the waveguide can vary significantly and are also dependent on the refractive indices of the layers within the waveguide structure.

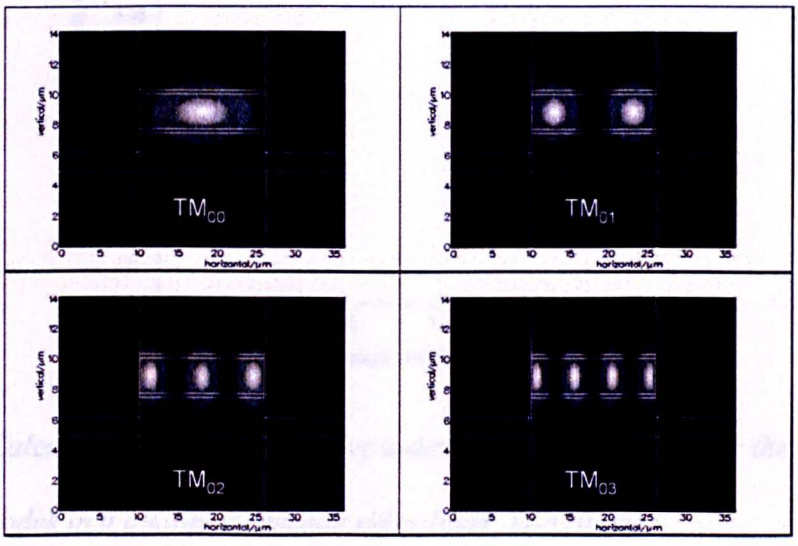

Figure 2.3 *Two-dimensional representation of the four lowest order transverse magnetic modes permitted to propagate in a QCL ridge waveguide. (λ = 10μm). Images are taken from commercial modelling software [1].*

In Figure 3, 2D representations of some of the transverse modes 'found' by the software, and permitted to propagate in the waveguide (λ=10μm), are shown as an example. A useful visual presentation by Yu *et al*, [13] demonstrates the presence of

higher order modes propagating in a quantum cascade laser (λ~5μm) waveguide and shows a preference for higher order modes close to threshold. The modes have been shown experimentally using a near-field scanning optical microscope (NSOM) to image the intensity profile directly at the laser facet. The preference for higher order modes lasing close to threshold is due to a reduced mirror loss calculated for higher order modes, even though the confinement factor (the fraction of the mode energy contained in active core region) is poorer.

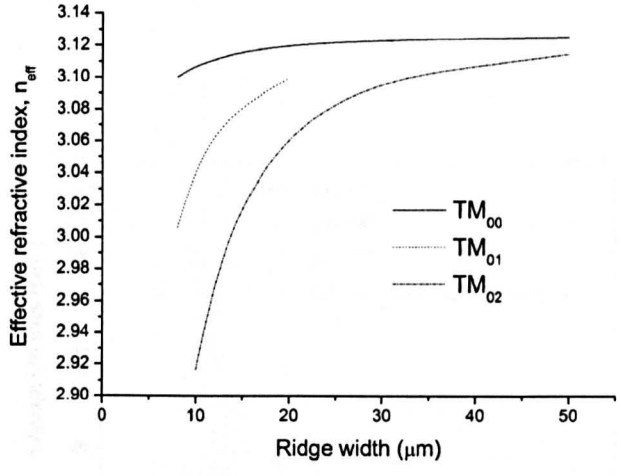

Figure 2.4 *Calculated effective refractive index versus ridge width for the three lowest order TM modes in a quantum cascade ridge laser. (λ=10μm).*

In Fig. 2.4 the ridge width is plotted against the calculated effective refractive index values of the three lowest order transverse modes. The effective refractive index value can be significantly lower for higher order modes and will decrease more rapidly as the ridge width approaches the wavelength. In Fig. 2.5 the ridge width is plotted against the calculated waveguide loss. The loss can be seen to increase as the ridge width decreases. This is due to a greater overlap with the higher loss material (e.g.

silicon nitride) on the outside walls of the waveguide. The arbitrary value used for the complex refractive index (n = 2 + 0.079i) for Fig. 2.5 (a-c) is chosen for the purpose of demonstrating the higher losses for narrower ridge widths and higher order modes. The complex refractive index of silicon nitride at mid-infrared wavelengths is not widely published. However, work published by Gunde and Macek [14] shows strong absorption in silicon nitride for wavelengths close to 10μm. Using the refractive index (n = 1.2 + 0.785i) taken from the aforementioned reference, the importance of a good understanding of the optical characteristics of the isolation layer on the outer walls of the waveguide is demonstrated by the larger losses shown in Fig. 2.5 (d).

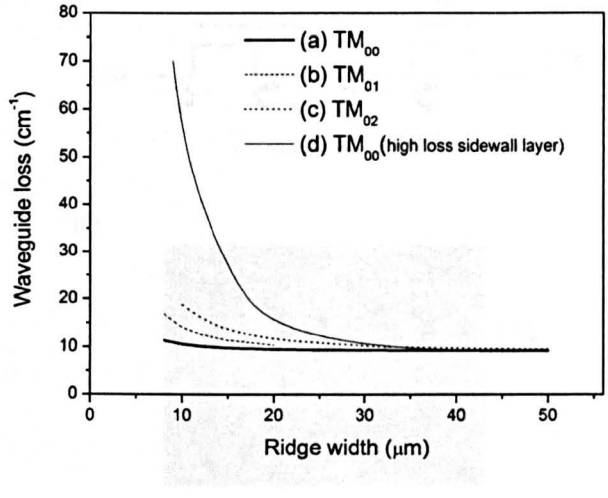

Figure 2.5 *Calculated waveguide loss versus ridge width for various transverse modes (λ=10μm) in a quantum cascade ridge laser.*

The waveguide losses discussed above do not include the mirror losses which also have a significant impact on device performance and will increase with decreasing cavity length. Assuming a cavity length of 1.5mm and a simple Fresnel analysis facet reflectivity of R ~ 27%, the mirror losses would be $\alpha_m = -\ln(R^2)/(2L) \approx 8.7$ cm^{-1}. As

explained in [13] higher order modes will have a slightly higher reflectivity from the facet, so lower mirror loss. In reality the mirror losses are likely to be significantly higher as explained by Page et al [15]. The mirror reflectivity of a cleaved facet QCL may be as low as 23% resulting in $\alpha_m \approx 9.8\ cm^{-1}$.

2.3 Coupled wave theory, coupling coefficients and stop bands

To obtain an accurate estimation for the coupling coefficient, the wave propagation in a periodic structure is considered. Good explanations, but different notations and approaches are given in the original paper [2] or references [16, 17].

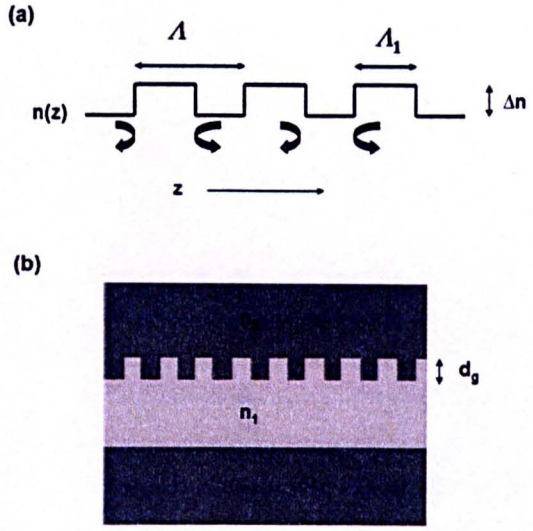

Figure 2.6 *(a) Schematic diagram of a periodic structure with refractive index n, period Λ and amplitude of refractive index variation, Δn. Curved arrows represent coupling of forward and backward waves (b) Schematic diagram of a waveguide with grating (depth = d_g) formed in the waveguide core region. Cladding regions have a refractive index (n_2) lower than core region (n_1).*

If a periodic structure (Fig. 2.6a) with refractive index varying in the z-direction (direction of propagation) and all variations in the x and y directions are neglected, then refractive index n(z), and the gain constant $\alpha(z)$ can be written as,

$$n(z) = n_{av} + \Delta n \cos(2\beta_0 z) \tag{2.12}$$

$$\alpha(z) = \alpha_{av} + \Delta\alpha \cos(2\beta_0 z) \tag{2.13}$$

where (n_{av}, α_{av}) are the average values of the medium and (Δn, $\Delta\alpha$) are the amplitudes of the spatial variation.

The Bragg propagation constant β_0 is related to the period of the grating by

$$\beta_0 = m\pi / \Lambda = 2\pi n_{av} / \lambda_B = k_0(\lambda_B)\, n_{av} \tag{2.14}$$

where λ_B is the Bragg Wavelength in free space and $k_0(\lambda_B)$ is the free space propagation constant at λ_B. M is the period order (any integer value). For a first order grating (M=1), the grating period will be equal to one half of the wavelength in the structure,

$$\Lambda = \lambda_B / 2\, n_{eff} \tag{2.15}$$

where (n_{eff}) is the effective refractive index of the mode propagating in the structure. The effect of the periodic structure is to couple forward and backward travelling waves in the structure. The equation for the electric field propagating with wavelength λ and free space constant ($k_0 = 2\pi / \lambda$) is,

$$\frac{d^2E}{dz^2} + [n(z)\, k_0]^2 E = 0 \qquad (2.16)$$

Assumptions are made that the DFB laser oscillates close to the Bragg frequency, the gain is small over distances of the order of a wavelength and the variations in refractive index and gain (loss) are small.

$$\Delta n << n_{av}$$

$$\Delta\alpha << \beta_0 = 2\pi\, n_{av} / \lambda_0 \qquad (2.17)$$

This allows the k_0 constant of the wave equation to be written as,

$$k_0^2 = \beta^2 + 2j\alpha\beta + 4\kappa\beta \cos 2\beta_0 z \qquad (2.18)$$

where $\beta = 2\pi\, n_{av} / \lambda_0$.

The coupling coefficient κ is introduced and is defined as,

$$\kappa = \frac{\pi\, \Delta n}{\lambda_0} + j\frac{\Delta\alpha}{2} \qquad (2.19)$$

where the coupling coefficient is a measure of the strength of the backward Bragg scattering and so is the amount of feedback (per unit length). Commonly the unit used is (cm^{-1}).

In the work reported in references [16] and [17] a slightly different equation for the real refractive index part of the coupling coefficient is derived for a uniform

rectangular grating formed in the waveguide core (active region) as shown in Fig. 2.6b. The methods combine the essential features of references [2] and [8] with the intention to take into account grating shape, depth and mark to period ratio. Furthermore, since the coupling is due to the interaction of the grating and the evanescent part of the transverse mode, then the coupling coefficient will also depend on the thickness and composition of the active and cladding layers in the DFB laser. The equation is written as,

$$\kappa \approx k_0 \, \Delta n \, \Gamma_g \, [\sin(m\pi\Lambda_1/\Lambda) / m\pi] \qquad (2.20)$$

where Γ_g is the confinement factor of the grating region, m is the period order. Λ_1/Λ is the mark to period ratio. This can be further simplified for a first order grating to

$$\kappa \approx \frac{2 \, \Delta n \, \Gamma_g}{\lambda_B} \cdot f_{red} \qquad (2.21)$$

where

$$\Delta n = (n_1 - n_2)$$

$$\textit{Reduction factor, } f_{red} = \sin(\pi\Lambda_1/\Lambda)$$

and the confinement factor Γ_g is calculated for an unperturbed structure where the grating has been replaced by a layer of thickness d_g and refractive index n_{av}. The n_{av} value is given by $n_{av}^2 = (n_1^2 + n_2^2) / 2$. The shape of the grating can have a significant effect on the coupling coefficient. For a triangular shaped (sawtooth) grating the

reduction factor would be expected to be, $f_{red} \approx 2/\pi$. For a sinusoidal grating, $f_{red} \approx \pi/4$ (note the similarity of equation 21 to 19 in this case).

It is well known that stop-bands of frequencies (where propagation is forbidden) are observed for periodic structures. Therefore, stop bands can be present in DFB lasers. A DFB laser will have two oppositely travelling waves. Theses are given the notation S and R. These waves will grow due to the presence of gain and because they feed into each other (Bragg scattering). The waves can be described by their complex amplitudes S(z) and R(z).

$$E(z) = R(z) \exp(-j\beta_0 z) + S(z) \exp(j\beta_0 z) \qquad (2.22)$$

The amplitudes vary slowly, when taking the assumptions from (17) into account, so the second derivatives (d^2R/dz^2) and (d^2S/dz^2) can be neglected.
Using all the assumptions, equation (22) can be inserted into wave equation (16) to obtain a pair of coupled-wave equations,

$$-R' + (\alpha - j\delta)R = j\kappa S$$
$$S' + (\alpha - j\delta)S = jkS \qquad (2.23)$$

where δ is a normalised frequency parameter defined by,

$$\delta \approx \beta - \beta_0 = n(\omega - \omega_0) / c \qquad (2.24)$$

and is an indication of the departure of the oscillation frequency ω from the Bragg frequency ω_0, at the Bragg condition ($\delta = 0$). Since departures are small an assumption is made that ($\beta/\beta_0 \approx 1$) in the above equation. The coupled wave equations describe the propagation of the waves in the DFB structure in the presence of gain and the periodic variations in the medium. If a structure of length L is considered, extending from –L/2 to L/2, then the boundary conditions for the wave amplitudes are

$$R(-L/2) = S(L/2) = 0 \tag{2.25}$$

Equations (2.23) now specify the electromagnetic field in the model of the DFB laser. The solution yields the oscillation states (modes) of the periodic structure. The general solution to the coupled-wave equation is of the form,

$$R = r_1 e^{\gamma z} + r_2 e^{-\gamma z}$$
$$S = s_1 e^{\gamma z} + s_2 e^{-\gamma z} \tag{2.26}$$

where γ is the complex propagation constant obeying the dispersion relation,

$$\gamma^2 = \kappa^2 + (\alpha - j\delta)^2 \tag{2.27}$$

If a symmetry is assumed in the device we get symmetric and anti-symmetric field solutions $E(-z) = E(z)$ and $E(-z) = -E(z)$. This implies that for the coefficients, $r_1 = \pm s_2$ and $r_2 = \pm s_1$. The boundary conditions (2.25) mean that $r_1 / r_2 = s_1 / s_2 = -e^{\gamma L}$. Using these results the longitudinal field distribution of the modes in the DFB structure can be described by,

$$R = \sinh \gamma(z + 1/2L)$$

$$S = \pm \sinh \gamma(z - 1/2L) \qquad (2.28)$$

where we now have a set of modes corresponding to a discrete set of eigenvalues γ. To determine the eigenvalues we insert (2.28) into (2.23) and form the sum and the difference of the resulting equations (dropping the common factors) to obtain,

$$-\gamma\sinh(\gamma L/2) + (\alpha - j\delta)\cosh(\gamma L/2) = \pm j\kappa\cosh(\gamma L/2)$$

$$-\gamma\cosh(\gamma L/2) + (\alpha - j\delta)\cosh(\gamma L/2) = \pm j\kappa\cosh(\gamma L/2) \qquad (2.29)$$

Combining the expressions gives the equations below.

$$\gamma + (\alpha - j\delta) = \pm j\kappa e^{\gamma L}$$

$$\gamma - (\alpha - j\delta) = \pm j\kappa e^{-\gamma L} \qquad (2.30)$$

Adding these equations gives an equation for the eigenvalues, γ

$$\kappa = \pm j\gamma / \sinh\gamma L \qquad (2.31)$$

where each eigenvalue there is a corresponding threshold gain constant α and a resonant frequency δ. These are obtained by subtracting the equations in (2.30) to give

$$\alpha - j\delta = \pm j\kappa \cosh\gamma L = \gamma\coth\gamma L \qquad (2.32)$$

The above solution of the coupled wave equations give the threshold modes of the DFB structure with each mode having a characteristic field pattern, threshold gain and resonant frequency.

In the case where $\alpha >> \kappa$, equation (2.27) may be written as $\gamma \approx \alpha - j\delta$. Inserting this into equation (2.30) gives the equation,

$$2(\alpha - j\delta) \approx \pm j\kappa \exp(\alpha - j\delta) L \qquad (2.33)$$

where, the absolute value gives us the threshold condition,

$$4(\alpha^2 + \delta^2) \approx \kappa\kappa^* e^{2\alpha L} \qquad (2.34)$$

when in the vicinity of the Bragg frequency ($\delta \approx 0$) can be expressed as

$$4\alpha^2 e^{-2\alpha L} \approx (n_1/\lambda)^2 + \alpha_l^2/4. \qquad (2.35)$$

A comparison of the phases in (2.33) when ($\delta << \alpha$) gives the resonant condition near the Bragg frequency, ν_0. This can be written in terms of the resonant frequencies $\nu = \omega/2\pi$,

$$(\nu - \nu_0)\,(c/2nL)^{-1} \approx q + 1/2 + (1/\pi)\text{phase}(\kappa) \qquad (2.36)$$

where, q is an integer. It is here we see that resonances are spaced by c/2nL, as is usual for a two mirror laser with a cavity length, L. For index coupling (κ real) we see

there is no resonance at the Bragg frequency. However, for gain (loss) coupling (κ imaginary) there is a resonance exactly at ($\nu = \nu_0$).

The difference in the permitted resonant frequencies between gain and index coupling shows how they can affect the spectra of DFB lasers. If we ignore the effects of the cleaved facets and assume they have zero reflectivity, then for purely index coupled lasers a characteristic spectrum will have two peaks (modes) simultaneously lasing, symmetric with respect to the Bragg frequency (corresponding to the stop band). Additionally, the further away we go from the Bragg frequency the threshold gain of the modes will increase providing spectral selectivity. For purely gain coupled lasers there is no stop band since there is a resonant frequency with the lowest threshold gain at the Bragg frequency and so the DFB spectrum should show just a single mode.

From a practical point of view, ignoring the facet effects is not really possible. Cleaved facets will have some degree of reflectivity and random phase shifts due to uncontrollable variations in the cleaving process (i.e. where the facet is cleaved in relation to the grating period). Facet reflections will generally break the gain degeneracy that occurs when there are no reflection for the two modes either side of the stop band. However, two modes of different magnitude are likely to be present reducing the single mode output that is desired. In the case where the DFB laser has reflecting facets, the DFB mode will have the lowest threshold gain and will lase before the FP modes. However, should the DFB mode and Bragg wavelength be sufficiently far from the material gain peak, then it is possible that a FP mode may have a lower threshold gain and reach threshold first. Again this would reduce the level of single mode operation.

Single mode yield problems associated with index coupled DFB lasers (due to the mode degeneracy) has led to attempts to improve the yield by using facet coatings [18]. A high (>80%) and low (~1%) reflectivity have provided good yields. However, facet coatings are an expensive, time consuming part of semiconductor laser manufacturing with added yield implications of their own. Mid-infrared quantum cascade DFB lasers are typically both index and gain(loss) coupled due to most of the epitaxial layers having some level of absorption. The complex (real and imaginary) coupling coefficient of the lasers is beneficial to them operating in a single mode, since like purely gain coupled DFB lasers, the degeneracy of the modes either side of the stop band is lifted. Their performance is relatively unaffected by facet reflections. Even for near infrared wavelength interband lasers a relatively high yield can be achieved without facet coatings by inserting an absorbing grating layer near the active region.

For a uniform grating, a longitudinal variation of the optical intensity and carrier density can be present in the cavity. Positions with high optical field intensity may result in lower carrier density resulting in spatial hole burning and multimode operation. Generally, the location of the spatial hole burning will relate to the strength of the coupling. Coupling strengths are usually put into three categories: under-coupling, critical coupling and over-coupling. For under-coupled lasers the optical intensity will be greatest at the edges of the grating. For over-coupled lasers the intensity will be greatest in the centre of the grating and for critical coupling the intensity variation will be less pronounced. The impact of the spatial hole burning is reduced for even small amounts of gain (loss) coupling [19], further improving single mode yields.

For DFB laser spectrum that shows both modes (peaks) associated with the stop band, an approximate coupling coefficient value can be calculated from the stop band width ($\Delta\nu$) when the spectrum of a FP laser of the same dimensions is also measured [Tamir1990]. The measured coupling coefficient is given by,

$$\kappa_{meas} \approx \pi\, n_g\, \Delta\nu \qquad (2.37)$$

where ($n_g = 1 / 2\ L\ \Delta\nu_{long}$) is the group refractive index measured from the longitudinal mode spacing ($\Delta\nu_{long}$) of the FP spectrum. The stop band width and FP mode spacing are both measured in units of (cm^{-1}).

2.5 Side mode suppression ratio (SMSR)

A straightforward measurement, that provides information on mode discrimination and tuning range of a DFB laser, is given by the side mode suppression ratio. The SMSR is defined as the ratio of the emitted output power of the main mode (P_m) and that emitted by the second strongest mode (P_s). It is expressed in decibels (dB) as given below.

$$\text{SMSR (dB)} = 10 \log (P_m / P_s) \qquad (2.38)$$

DFB lasers can exhibit different behaviour depending on temperature or drive current so SMSR values may vary. SMSR requirements can vary depending on the application but for near infrared telecoms applications a value of 30dB is generally required for lasers to be called dynamic single mode. A lower SMSR (~25dB) value is often sufficient for spectroscopic applications.

2.6 Metalised surface gratings

DFB quantum cascade lasers are conventionally fabricated by defining a grating in the top surface of the laser ridge. In this section the waveguide modelling of this type of device is addressed. Using the waveguide modelling software [1], the DFB laser ridge waveguide can be considered as a collection of two ridge waveguides, as shown in Fig. 2.7a. One waveguide represents the standard waveguide design. The other is the same waveguide but with the height reduced by the desired grating depth (d_g). This effectively produces a variation in the refractive index (and loss). However, this method can have complications when calculating the coupling coefficient when using the large refractive index and loss values of metals in the mid-infrared. The refractive index of gold (λ = 10μm) is (n = 11.5 + 67i) [20]. An accurate method [17, 21] for calculating the coupling coefficient is to replace the grating with an additional unperturbed layer with an intermediate refractive index as shown in Fig. 7b. This layer may selected to calculate the fraction of the mode energy contained in that 'grating' region (grating confinement factor) allowing the coupling coefficient (κ) to be calculated using equation (21). As previously explained, transverse modes propagating in the waveguide may be back-scattered from the grating, coupling the forward and backward travelling waves. The amount of feedback for each longitudinal transverse mode will vary and may be calculated. In Fig. 2.8, a plot of the relative reflection versus the grating period is shown (λ=10μm) for the TM_{00} and TM_{01} modes. It shows the fundamental mode is reflected most, for a period of ~ 1.61μm. It is also clear that for the higher order mode (with lower effective refractive index) the reflectance is greatest for a grating with a longer period.

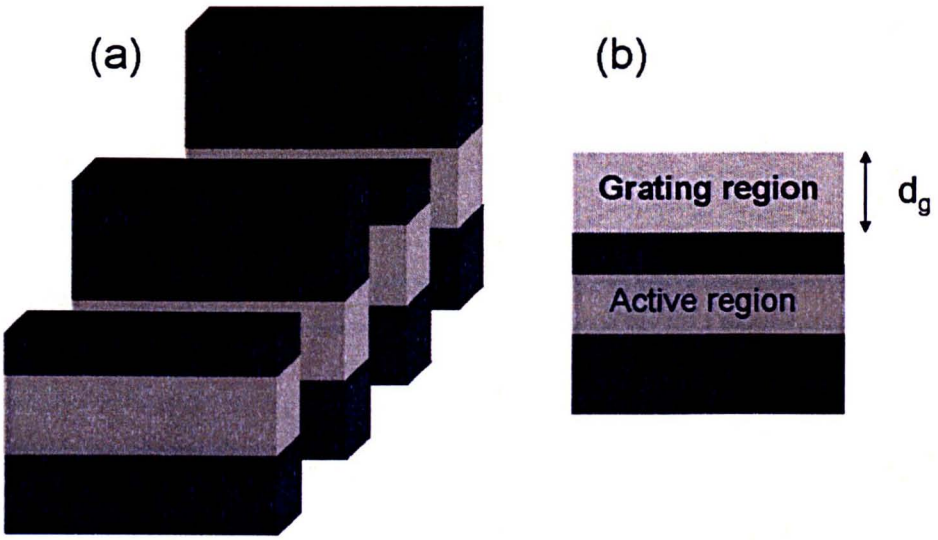

Figure 2.7 *Schematic diagram a quantum cascade DFB laser waveguide with (a) several waveguides of different height representing a surface grating (b) with grating region (depth, d_g) replaced by an unperturbed layer with an intermediate refractive index.*

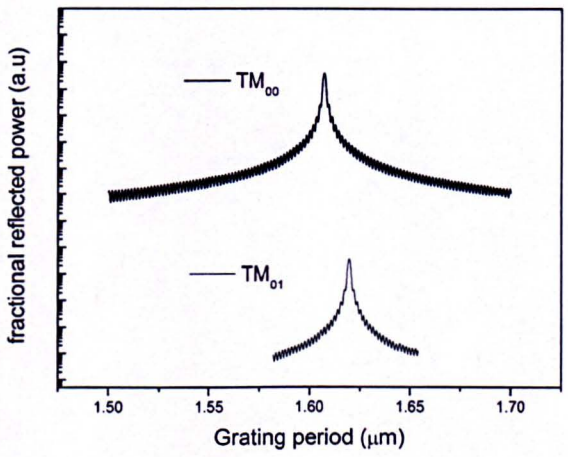

Figure 2.8 *Plot of the relative reflection versus grating period for a surface grating, DFB quantum cascade laser*

In Fig. 2.9 a plot of the calculated value of the real part of the coupling coefficient is plotted against grating depth for two different ridge widths. The grating is assumed to be rectangular with a 50% mark to period ratio. It is clear from the plot that the calculated values for the coupling coefficient are significantly higher for the narrower ridge. This is due to more of the optical mode being confined in the grating for narrower ridges.

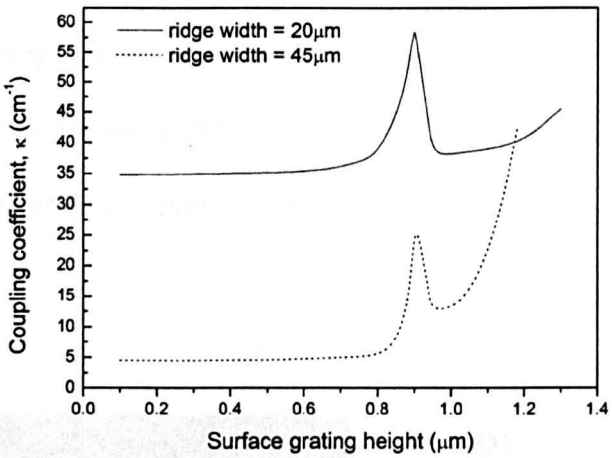

Figure 2.9 *Calculated value of the coupling coefficient (real part) plotted against the grating depth for two different quantum cascade laser ridge widths. The surface grating is rectangular with a 50% mark to period ratio.*

2.7 Buried grating

The term 'buried' grating refers to a design where the top of the active region (InGaAs layer) is partially etched and the InP cladding is re-grown on top. The same method, as explained in the surface grating section previously, may be used to calculate the coupling coefficient. A simplified representation of the structure, is shown in Fig. 2.10. Unlike the surface grating design, the refractive index contrast of the semiconductor materials (e.g. InP and InGaAs) in the grating region is much less than a semiconductor / gold grating. Since the grating may be considered "weak", it is

possible to use the Kogelnik and Shank method to estimate the coupling coefficient using equation (19). Using the computer waveguide modelling software, the modal effective refractive index in the full and 'etched' structures may be obtained (giving Δn). The two methods obtain very similar results.. For consistency with other designs, equation (21) is used for calculating κ. In Fig. 2.11 the real part of the coupling coefficient is plotted against the grating depth ($f_{red} = 1$), for ridge widths of 10 and 30μm. From the plot we see there is a linear increase in the coupling as the grating depth increases. Furthermore, there is an increase as ridge width decreases. This is due to an increase in the calculated grating confinement factor, Γ_g (the fraction of the modal power in the grating region) for narrower ridge widths.

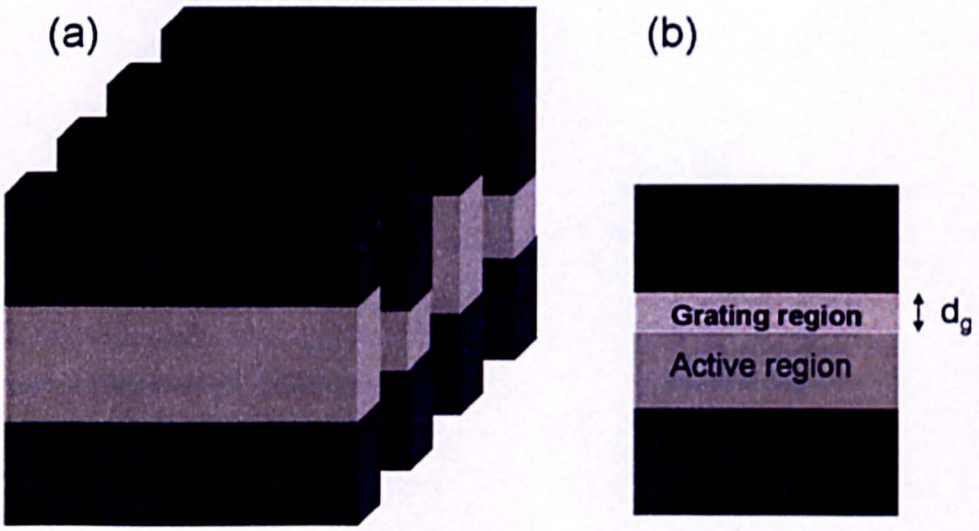

Figure 2.10 *Schematic diagram a quantum cascade DFB laser waveguide with (a) several waveguides of different active region height representing an overgrown (buried) grating (b) with grating region (depth, d_g) replaced by an unperturbed layer with an intermediate refractive index.*

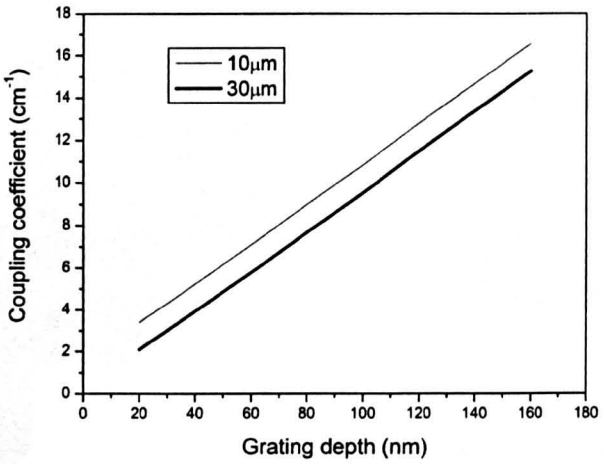

Figure 2.11 *Calculated value of the coupling coefficient (real part) plotted against the grating depth for various quantum cascade laser ridge widths. The surface grating is rectangular with a 50% mark to period ratio.*

2.8 Lateral gratings

The lateral grating design has fabrication advantages over other designs since the grating and ridge can be simultaneously defined in the same process. However, the geometric design of the device is potentially more critical than for other designs. In Fig. 2.12 a schematic diagram of the lateral grating DFB laser is shown, defining the grating width (d_g).

Etching a periodic variation into the sidewalls (and active region) of the laser results in a complex-coupled device. This is because there is a variation in the gain / loss. There is also a strong variation in the real part of the refractive index, as the sidewall is typically coated by the dielectric isolation layer (e.g. silicon nitride). Similar to the surface grating (although to a much lesser extent), a difference in refractive index will exist.

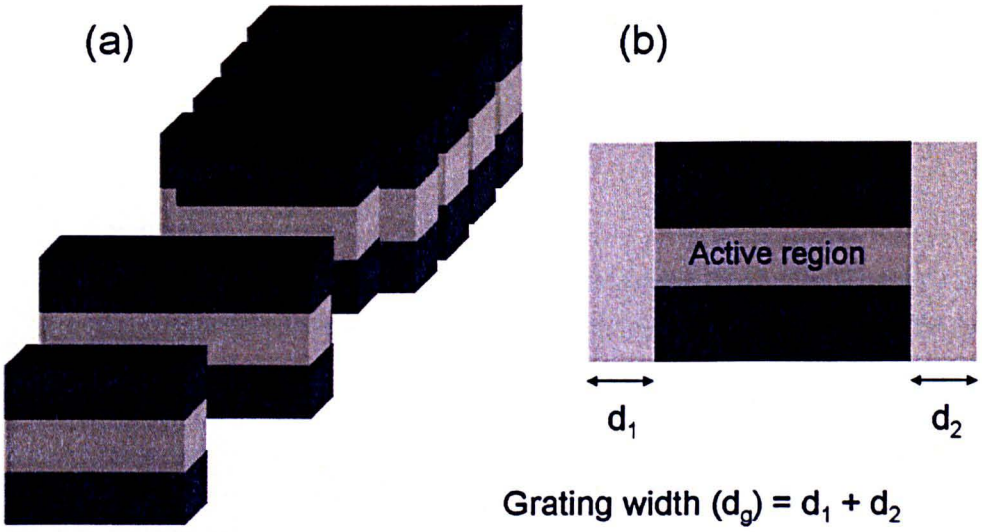

Figure 2.12 *Schematic diagram a quantum cascade DFB laser waveguide with (a) several waveguides of different width representing a lateral grating (b) with grating region (width, d_g) replaced by two unperturbed layers with intermediate refractive indices.*

However, in the lateral grating case the difference exists between the active region and the dielectric isolation layer ($\Delta n \sim 2$). Due to the lithography and etching processes, the grating is more sinusoidal in shape than perfectly rectangular. Equation (19) is used for calculating the coupling coefficient with the modulation in the effective refractive index being calculated from the effective refractive indices for two ridges of different width. For example, a 9μm ridge with 1μm lateral grating would be modelled by calculating the difference between the effective refractive indices of a 10μm and a 9μm ridge ($d_1 = d_2 = 0.5\mu m$). A graph of the coupling coefficient of the lowest order transverse modes (9, 10, 14μm wide ridges) versus the grating width is shown in Fig. 2.13. Additionally, the graph shows the coupling coefficient is significantly larger for a TM_{02} mode compared to the fundamental mode. This is due

to a greater overlap of the higher order modes with the sidewalls.

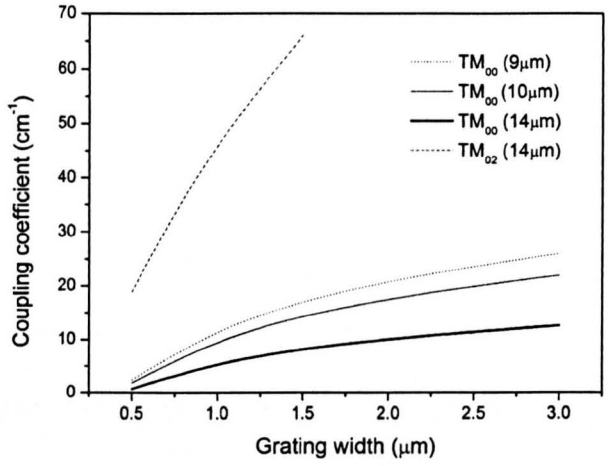

Figure 2.13 *Calculated value of the coupling coefficient (real part) plotted against the grating width (d_g) for various lateral grating DFB quantum cascade lasers. The lateral grating is sinusoidal in shape with a 50% mark to period ratio.*

2.9 References

[1] FIMMWAVE / FIMMPROP by Photon Design Ltd, UK, www.photond.com

[2] Kogelnik, H., and Shank, C.V.: 'Coupled-Wave theory of Distributed Feedback Lasers', J. Appl. Phys 1972, 43, 2327, pp.2327-2335

[3] Nakamura, M., Yariv, A., Yen, H. W., Somekh, S., Garvin, H. L.: 'Optically pumped GaAs surface laser with corrugation feedback', App. Phys. Lett. 1973, 22, p.515

[4] Aiki, K., Nakamura, M., Umeda, J., Yariv, A., Katzir, A., Yen, H. W.: 'GaAs-GaAlAs Distributed Feedback Diode Lasers with Separate Optical and Carrier Confinement', App. Phys. Lett. 1975, 27, pp.145-146

[5] Nakamura, M., Aiki, K., Umeda, J., Yariv, A., Yen, H. W., Morikawa, T.: 'GaAs-$Ga_{1-x}Al_xAs$ double-heterostructure distributed-feedback diode lasers', App. Phys. Lett. 1974, 25, 9, pp.145-146

[6] Nakano, Y., Luo, Y., Tada, K.: 'Facet reflection independent, single longitudinal mode oscillation in a GaAlAs/GaAs distributed feedback laser equipped with a gain-coupling mechanism', Appl. Phys. Lett. 1989, **55**, pp.1606

[7] Gmachl, C., Faist, J., D.L., Baillargeon, Capasso, F., Sirtori, C., Sivco, J. N., Chu, S. N. G., Cho, A. Y.: 'Complex-coupled distributed feedback quantum cascade laser', IEEE Phot. Tech. Lett. 1997, 10, 8, pp. 1090-1092

[8] Wang, S.: 'Principles of distributed feedback and distributed Bragg-reflector lasers', IEEE J. Quant. Elect 1974, 10, pp. 413-427

[9] Yariv, A., Gover, A.: 'Equivalence of the coupled mode and Floquet-Bloch formalism in periodic optical waveguides', Appl. Phys. Lett. 1975, 26, pp. 537-539

[10] Finger, N., Schrenk, W., Gornik, E.: 'Analysis of TM-polarized DFB laser structures with metal surface gratings' IEEE J. Quant. Elect 2000, 36, 7, pp.780 - 786

[11] Sudbo, A. S.: 'Film mode matching: a versatile numerical method for vector mode field calculations in dielectric waveguides', Pure and Applied Optics, 1993, 2, pp.211-233

[12] Adachi, S.: 'Physical properties of III-V semiconductor compounds' Wiley, 1992

[13] Yu, N., Diehl, L., Cubukcu, E., Pflügl, C, Bour, D., Corzine, S., Zhu, J., Höfler, G., Crozier, K. B., Capasso, F.: 'Near-field imaging of quantum cascade laser transverse modes', Optics Express, 2007, 15, 20, 13227-13235

[14] Gunde, M. K., Maček, M.: 'Infrared Optical Constants and Dielectric Response Functions of Silicon Nitride and Oxynitride Films', Physica Status Solidi (a) 2001, 183, 2, pp.439-449

[15] Page, H., Collot, P., De Rossi, A., Ortiz, V., Sirtori, C.: 'High reflectivity metallic mirror coatings for mid-infrared ($\lambda \approx 9$ μm) unipolar semiconductor lasers', Semicond. Sci. Technol. 2002, 17, pp. 1312–1316

[16] Agrawal, G. P., Dutta, N. K.: 'Semiconductor lasers', second edition, KAP, 2000

[17] Buus, J., Amann, M., Blumenthal, D. J.: 'Tunable laser diodes and related optical sources', second edition, Wiley-Interscience, 2005

[18] Yoshida, J., Itaya, Y., Noguchi, Y., Matsuoka, T., Nakano, Y.: 'Sufficiently side-mode-suppressed high output power 1.5 μm DFB lasers', Elect. Lett. 1986, 22, pp. 327-328

[19] David, K., Morthier, G., Vankwikelberge, P., Baets, R. G., Wolf, T., Borchert, B.: 'Gain-coupled DFB lasers versus index coupled and phase-shifted DFB lasers: A comparison based on spatial hole burning corrected yield', IEEE J. Quant. Elect, 1991, 27, 6, pp. 1714-1723

[20] Schulz, L. G.: 'The optical constants of silver, gold, copper, and aluminium. 1) the absorption coefficient k and 2) the index of refraction, n', J. Opt. Soc. Amer.

1954,44, pp.357–362

[21] Handa, K., Peng, S. T., Tamir, T.: 'Improved perturbation analysis of dielectric gratings', J. Applied Physics, 1975, 5, 4, pp.325-328

Chapter 3 - Distributed Feedback Quantum Cascade Lasers ($\lambda \approx 10\mu m$) with Profiled Surface Gratings

3.1 Introduction

The experimental results presented in this chapter detail the design, fabrication and characterisation of single-mode distributed feedback quantum cascade lasers (DFB QCL) with surface gratings [1]. A time consuming and complex part of the design and fabrication of a DFB laser is the production of the grating. Surface gratings etched into the top of the laser ridge (upper cladding layers) are considered the simplest way to achieve a DFB QC laser since an epitaxial overgrowth step is not required. These are usually achieved using wet chemical etching [1-3] with relatively shallow etch depths and corrugated grating profiles. Dielectric masks and reactive ion etching have been utilised to etch deeper gratings with rectangular profiles [4].

In this chapter, a novel V-groove grating is achieved using an inductively coupled plasma (ICP) etch process, allowing deep controllable etch depths and reduced processing time (compared to dielectric or metal etch masks). Furthermore, this means the upper cladding layer thicknesses are not required to be reduced to achieve greater coupling to the optical mode (which may be detrimental to any Fabry-Perot layers processed simultaneously). Additionally, there are potential benefits to the bar cleaving process and metal deposition process where deep rectangular profiles can suffer from shadowing effects resulting in non-uniform metal coverage. The coupling coefficient of the grating will be dependent on the etch depth and profile of the grating

[see chapter 2]. Therefore, a technology for creating gratings of various profiles and with good depth control is of interest and useful for investigating the relative magnitudes of these effects on device characteristics and allowing optimal device design. Included in this chapter are details of a device design that is optimised for high single mode yield and control over the emission wavelength. The potential single mode yield of a DFB QCL design (suitable for spectroscopic applications) is investigated as very little quantitative information is published on device suitability for manufacture.

3.2 V-groove gratings in Indium phosphide by inductively coupled plasma (ICP) etching

Reproducibility, anisotropy, uniformity and other advantages of dry etching are necessary for the fabrication of increasingly complex semiconductor devices. A number of papers have now been published reporting smooth, low-bias voltage etching with low surface damage of InP using $SiCl_4$ and $SiCl_4$/Ar [5–10]. These have centred upon characterizing the dry etch process to reduce surface damage and to achieve vertical sidewall profiles using reactive ion etching (RIE) [10], electron cyclotron resonance (ECR) [8] and inductively coupled plasma (ICP) etching [9]. InP etch profiles and selectivity are known to be dependent on parameters such as chamber pressure, rf power, temperature and $SiCl_4$ flow rate. CH_4/H_2 gas mixtures have been used for some time but have the drawback of polymer formation / deposition, resulting in poorer process control and contamination [11]. Much of the work in the literature is applicable to the fabrication of photonic band-gap devices such as distributed feedback (DFB) lasers. The profile of the grating structure is not

usually of significant importance, resulting only in a modification of the grating coupling strength for different grating structures [12]. For single-mode lasers operating in the mid-infrared, such as quantum cascade lasers, a DFB is often realized using gold-filled gratings. In this case, there are a number of effects simultaneously altering the degree of complex and real coupling of the grating.

Wet chemical etching based on HBr and HCl has been used to produce v-grooves in a wide variety of semiconductor materials. These grooves may be used for a range of applications, such as fibre-optic positioning, creating mirrors for total internal reflection, and as cleave initiators. These wet etchants have the disadvantage of being etch rate dependent on crystal orientation and can have significant undercutting of the mask. This limits the depth of a grating for a quantum cascade DFB laser. Furthermore, wafers may need to have their back-side protected and can suffer from poor uniformity and repeatability [13]. A dry etch process for v-groove formation would therefore be an extremely useful tool in component manufacturing, in particular for the definition of cleave initiators [14]. In this chapter we describe a process for the definition of V-shaped structures in InP by ICP etching using $SiCl_4$/Ar. Figure 1 shows a schematic diagram showing a model for the etch process. The upper part shows a cross section of the photo-resist masked sample at the beginning of the etch process. $SiCl_4^+$ and Ar^+ ions bombard the InP surface. The chemical etching mechanism produces InCl*x* and PCl*x* etch products, with InCl*x* being the less volatile and less easily desorbed. The angle of the sidewall is determined by the competing processes of re-deposition / adsorption of less volatile products (InCl*x*) onto the sidewalls, and sputtering from the etched sidewalls [5]. The etch rate and shape of the trench is therefore governed by the bombarding ion flux rate and energy, in turn

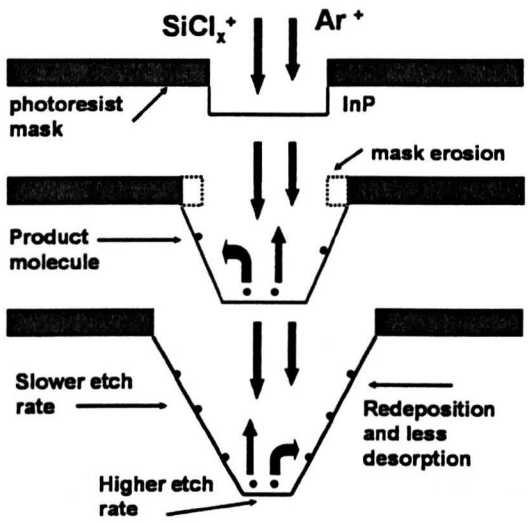

Figure 3.1 *Schematic diagram showing the influence of incident ions when inductively coupled plasma etching V-grooves in InP using $SiCl_4$/Ar. Mask erosion coupled with re-deposition and reduced desorption of the etch products creates a sloped sidewall. Ion bombardment enables desorption to occur at a faster rate from the flat, bottom part of the trench allowing the chemical etching to continue.*

governed by the surface profile, temperature, ICP power (plasma density) and rf power (ion energy). In our model, we now introduce erosion of the photoresist mask, resulting in the formation of angled sidewalls. Due to the reduced effective flux on these angled sidewalls compared to the bottom of the grating, a lower etch rate is expected, resulting in the gradual formation of a v-shaped groove. This process utilizes a small amount of photoresist mask erosion to locally vary the etch rate within the masked regions. Due to the careful tuning of the chemical and bombardment enhanced etching components of the dry etch process, this results in the formation of a v-shaped profile. This etch is shown to have a self-limiting etch rate helping us to control etch depth and indicating an improved process repeatability.

3.2.1 Etching

The experiments were carried out on (100) n^+ InP substrates. The samples were patterned using Shipley Megaposit SPR350 photoresist and conventional photolithography. For quantum cascade laser gratings this allowed fast patterning of a full 2" wafer with various pitches of grating. The resist when spun on at 4000 rpm gave a resist thickness of approximately $1\mu m$, measured using a Dektak stylus profilometer. On some samples, a 250 nm thick SiO_2 layer was deposited by PECVD prior to coating and patterning with photoresist. The photoresist mask was then used to transfer the grating pattern into the SiO_2 using ICP etching with CHF_3/Ar etch gases. Both photoresist and dielectric masked samples had a grating pitch of 1.7 μm and a mark–space ratio of 70%. InP etching was performed in a load-locked, Oxford Instruments Plasmalab System 100 ICP etcher, where samples were etched on a silicon carrier wafer. Unless otherwise stated the table temperature was 25 °C and flow rates were $SiCl_4$ (7 sccm), Ar (20 sccm). Chamber pressure was 2 mTorr. Images of surface morphology, sidewall profiles and measurements of the etched samples were obtained using a Phillips XL series SEM.

Figure 3.2 shows the etch profile obtained under ICP conditions optimized for v-groove etching for two samples etched under identical conditions. Fig. 3.2(*a*) is the SEM micrograph of a photoresist masked sample, while Fig. 3.2(*b*) corresponds to a SiO_2 masked (thickness = 250nm) sample with the same mask dimensions as the sample shown in Fig. 3.2(*a*). A striking difference in the shape of the etched trench is clear. For the photoresist masked sample the etched surface is smooth and forms a sharp, clear, v-shaped groove, at an angle of ~30° to the normal. A vertical etch depth

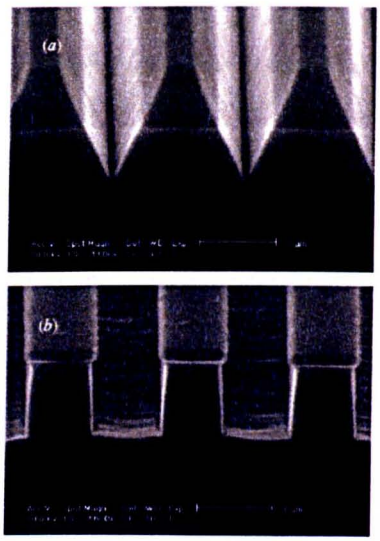

Figure 3.2 *Scanning electron microscope images of Indium Phosphide samples with inductively coupled plasma etched gratings using (a) photoresist mask (b) SiO_2 mask. Samples etched with 7/20 sccm, $SiCl_4$/Ar using ICP power = 2000 W and rf power = 100 W at 2 mTorr. Table temperature = 25 °C. Etch times = (a) 120 s (b) 60 s.*

of 700 nm is obtained. For the SiO_2 masked sample, the etch profile is flat at the bottom with almost vertical sidewalls. A vertical etch depth of 1000 nm is obtained. The only difference in the two etch processes is the choice of mask material, and their different erosion rates during etching. These observations are in agreement with our model for the etch process where a small amount of mask erosion is critical to the formation of a v-shaped groove. Fig. 3.3 shows an SEM micrograph of a sample etched using a photoresist mask under the same conditions as those used for samples in Fig 3.2. The base of the figure is aligned along (110). Angled sidewalls are observed along all sides of the mask, and therefore all crystallographic directions. This image clearly demonstrates that while the etch process is chemical in nature, there is no appreciable dependence on crystallographic orientation. In addition, and agreement with our model for the etch process, we observe a flat central etch region

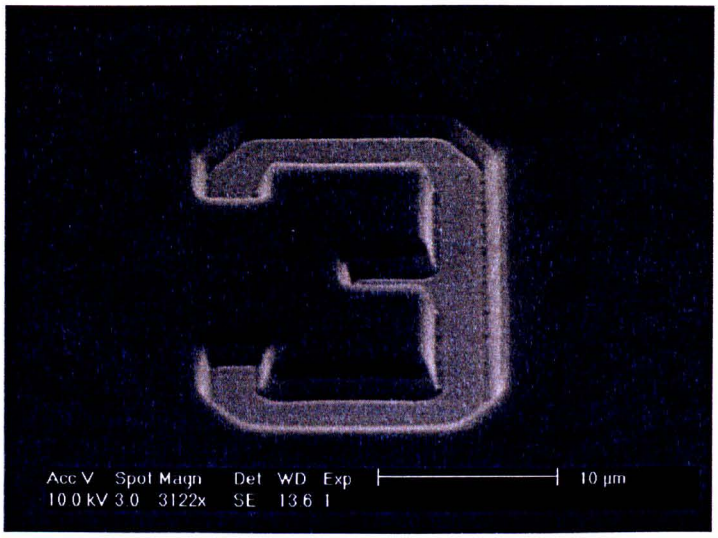

Figure 3.3 *Scanning electron microscope image of Indium Phosphide sample with inductively coupled plasma etched structure with photoresist mask still on. Samples etched with 7/20 sccm, $SiCl_4/Ar$ using ICP power = 2000 W and rf power = 100 W at 2 mTorr. Table temperature = 25 °C, etch time = 120 s.*

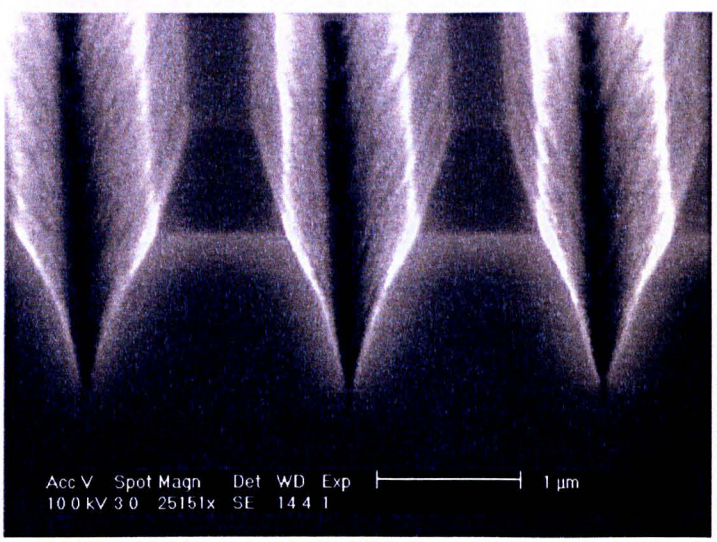

Figure 3.4 *Scanning electron microscope image of Indium Phosphide sample with inductively coupled plasma etched grating structure with photoresist mask still on. Samples etched with 7/20 sccm, $SiCl_4/Ar$ using ICP power = 2000 W and rf power = 100W at 2 mTorr. Table temperature = 70 °C, etch time = 240 s*

and an angled sidewall region. Fig. 3.4 shows a photoresist masked sample etched under identical conditions to those used previously except that a table temperature of 70°C was set. The etched surface was not as smooth as that obtained at 25°C, but a sharp, v-shaped groove at an angle of ~20° to the normal is formed. A vertical etch depth of 1000 nm is obtained at this temperature. The InP etch rate appears to increase slightly, but the sidewall angle at the bottom of the v-groove is clearly steeper at this elevated temperature. At elevated temperatures, the incident ions have a higher kinetic energy. Etch products will be more easily removed from the InP surface and the sidewall etch rate is therefore expected to increase resulting in a steeper sidewall angle. The increased surface roughness is attributed to an increase in the energy of incident ions and possible mask sputtering / re-deposition. Etches carried out at even higher temperatures resulted in a degradation of the photoresist grating pattern. The effect of plasma density on the etch profile is shown in Fig 3.5.

SEM images for samples etched using ICP powers of (*a*) 1000 W and (*b*) 500 W but with all other parameters identical to those used in Fig. 3.2. For ICP powers of 1000 W a vertical etch depth of ~700 nm was obtained at an angle of ~30° to the normal. The bottom of the v-groove is observed to be slightly less well defined than for ICP powers of 2000W (Fig. 3.2a). For an ICP power of 500W, a very poorly defined v-groove is formed with an etch depth of ~600 nm. This highlights the need to carefully balance the chemical and the ion bombardment enhanced etching, to obtain a well-defined v-groove. The vertical etch rate, for a photoresist masked sample, as a function of ICP power and etch time are plotted in Figs. 3.6(*a*) and (*b*), respectively.

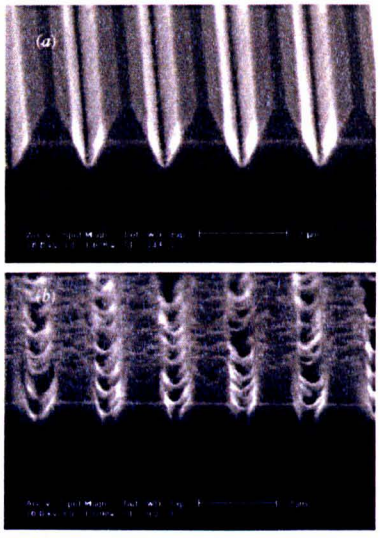

Figure. 3.5 *Scanning electron microscope image of InP sample with inductively coupled plasma etched grating structure with photoresist mask still on. Samples etched with 7/20 sccm, $SiCl_4$/Ar using ICP power = (a) 1000 W, (b) 500 W and rf power = 100 W at 2 mTorr. Table temperature = 25 °C, etch time = 240 s.*

An increase in vertical etch rate is observed with increasing ICP power, as expected due to the increase in plasma density, incident ion flux and sample surface temperature [7]. The etch rate is also observed to significantly reduce with increasing etch time, and therefore etch depth. This is in contrast to the samples masked with SiO_2 where the square grating did not show a decrease in etch rate with increasing time and etch depth. The slowing down of the etch rate coincides with the formation of the sloped sidewalls. The effect of rf power on the etch process is shown in Fig 3.7. This sample is identical to that in Fig. 3.2(*a*) except an rf power of 200W was used. A near vertical etch profile was obtained with a vertical etch depth of 800 nm. The increase in ion bombardment enhanced etching with increasing rf power increases the desorption of sidewall etch products, resulting in a near vertical etch. The increased incident ion energy has also resulted in considerable roughening / deforming of the

photoresist mask and so a non-uniform etch profile and depth is visible.

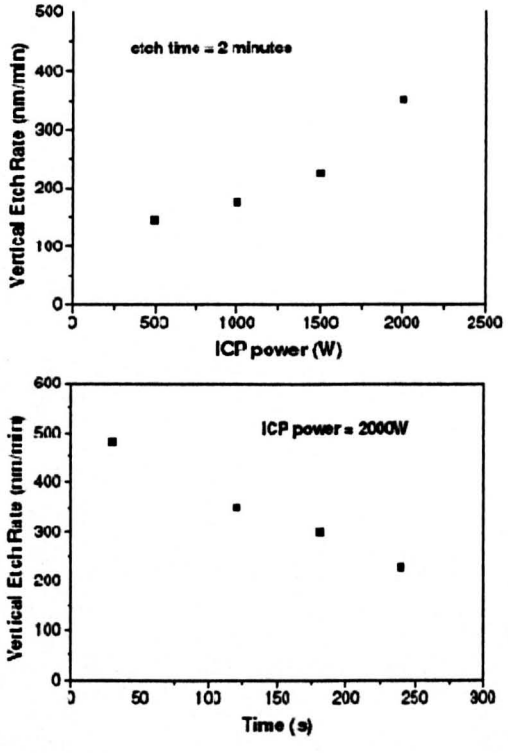

Figure 3.6 *Vertical etch rate of Indium Phosphide with photoresist mask as a function of inductively coupled plasma power (top) and etch time (bottom) in a $SiCl_4/Ar$ plasma at pressure = 2 mTorr and rf power = 100 W.*

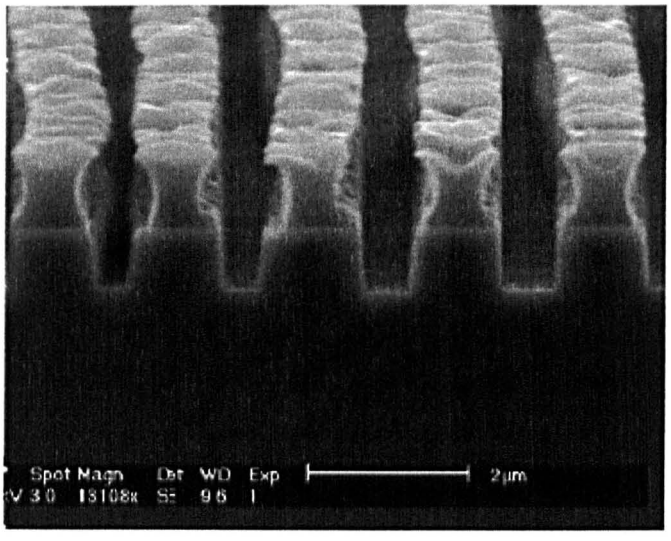

Figure 3.7 *Scanning electron microscope image of InP sample with inductively coupled plasma etched grating structure with photoresist mask still on. Sample etched with 7/20 sccm, $SiCl_4$/Ar using ICP power = 1000 W and rf power = 200 W at 2 mTorr. Etch time = 60 s*

3.3 Rectangular surface gratings

To achieve a conventional rectangular or 'square' grating profile several processes were used to compare their suitability. A $SiCl_4$ / Ar gas mixture was used to maintain consistency when comparing samples with different grating profiles.

In Figs. 3.8(a-e) SEM images of a selection of gratings etched using $SiCl_4$ / Ar are shown for a variety of etch parameters. In Fig 3.8a the effect of etching with the same parameters as the V-groove etch mentioned previously is shown. During the investigation and optimisation of the etch process, several parameters were changed. In Fig. 3.8b the ICP power is reduced to 1000W. This has the effect of reducing the chemical component of the etch and results in an increased roughness at the bottom of the grating.

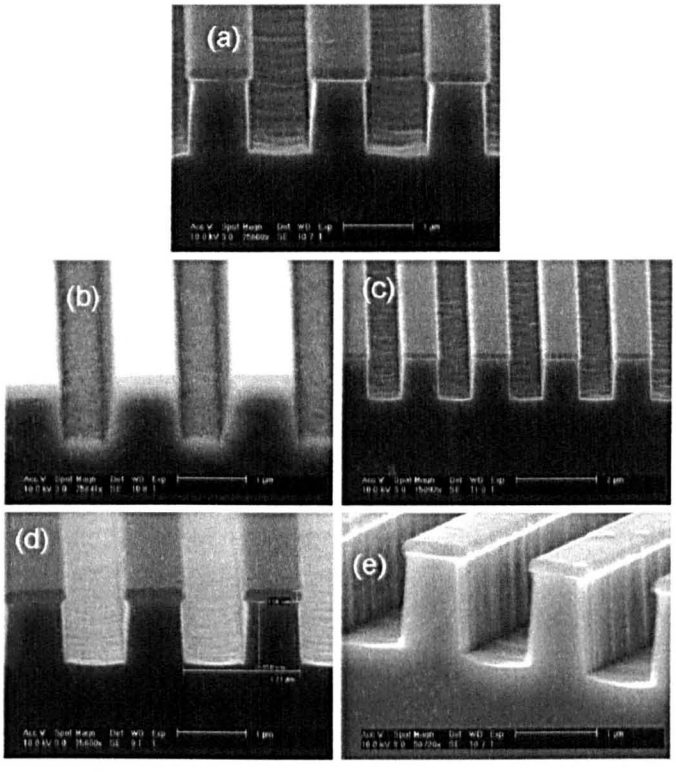

Figure 3.8 *Scanning electron microscope image of InP samples with inductively coupled plasma etched gratings. Etch parameters: table temperature = 25°C, pressure = 2mTorr* ***(a)*** *7/20 sccm, $SiCl_4$/Ar, ICP power = 2000 W, rf power = 100 W* ***(b)*** *7/20 sccm, $SiCl_4$/Ar, ICP power = 1000 W, rf power = 100 W* ***(c)*** *7/20 sccm, $SiCl_4$/Ar, ICP power = 1000 W, rf power = 220 W* ***(d)*** *7/30 sccm, $SiCl_4$/Ar, ICP power = 2000 W, rf power = 100 W* ***(e)*** *7/30 sccm, $SiCl_4$/Ar, ICP power = 1500 W, rf power = 220 W.*

In Fig. 3.8c the ICP power is kept at 1000W and the rf power is increased to 220W. A predictable increase in sidewall angle was observed without compromising surface smoothness. In Fig. 3.8d the same power parameters as in Fig. 3.8a are used but the Argon flow rate was increased to 30 sccm. This had no effect on the etch rate but a slight improvement in surface smoothness. Finally, in Fig. 3.8e the ICP power was

increased to 1500W and the rf power increased to 220W. The Argon flow rate was 30 sccm. This process had an InP etch rate of 1.2 μm/min (SiO_2 ~ 100 nm/min) with good vertical etching and smooth morphology.

3.4 Laser fabrication and characterisation

3.4.1 Fabry-Perot lasers

Samples (wafer MR2213) were initially processed into Fabry-Perot ridge lasers of various cavity lengths, and ridge widths of 14 & 19μm. The laser sample structure is given in chapter 1 and samples were processed as standard as also described in chapter 1. Lasers were mounted on gold coated copper heat-sinks and gold wire bonded. Characterisation of the optical performance was carried out using a FTIR spectrometer with a resolution of 0.2 cm^{-1}. In Fig. 3.9 the spectrum of a laser with a

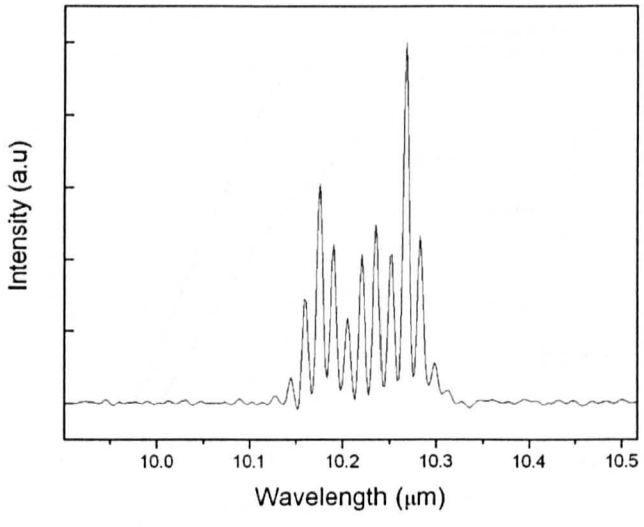

Figure 3.9 *Room temperature emission spectrum of a Fabry-Perot quantum cascade laser with ridge width = 19μm. FTIR spectrometer resolution = 0.2 cm^{-1}. Electrical pulse length = 100ns, repetition rate = 5kHz, drive current = 1A.*

ridge width of 19μm is shown. It was operated at room temperature with 100ns electrical pulse lengths and a 5kHz repetition rate. The drive current was 1A and the centre of the emission wavelength was measured to be at ~ 10.2μm. The measured value for the group refractive index (from the Fabry-Perot mode spacing) was $n_g \sim 3.45$. In Fig. 3.10 the light output power versus injection current density (under the same conditions) is shown for each of the cavity lengths and ridge widths. Characteristically, for semiconductor ridge lasers the threshold current density increases for shorter cavity lengths due to the increase in the facet mirror losses. Additionally, for longer wavelength QC lasers there is a significant increase in threshold current density for narrower ridges due to the increased loss experienced by the optical mode as it overlaps with the dielectric and gold layers on the outer walls of the ridge.

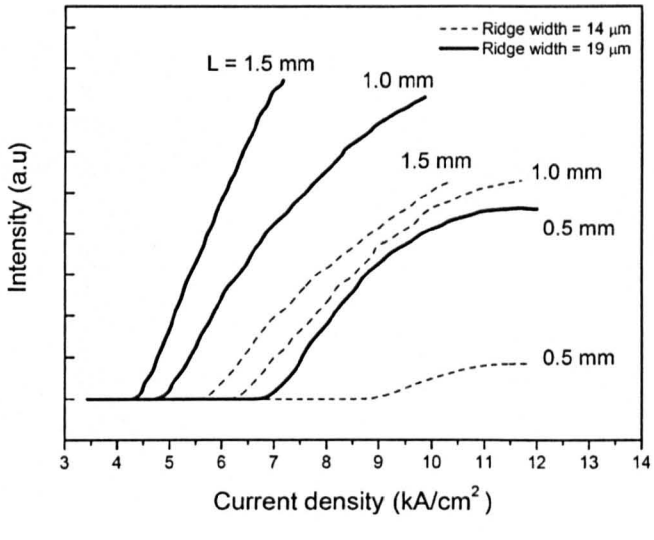

Figure 3.10 *Plot of the injection current density versus peak output power for a un-coated quantum cascade lasers with various cavity lengths and ridge width. Results are for pulsed electrical operation (100ns pulse width at 5kHz repetition rate) at room temperature.*

3.4.2 Distributed Feedback Lasers

DFB samples with first order gratings of periodicity $\Lambda = 1.680\mu m$ were exposed by contact lithography. Gratings were ICP etched to a depth of 700nm using the same epitaxial material as the FP lasers. The 'V-groove' gratings are shown in Fig. 3.11. The SEM image shows the gratings situated in the InP cladding layers above the active core region. The subsequent DFB laser fabrication for 'square' and 'V' gratings was identical to the FP lasers and the ridge width was 19μm. An example of a DFB QCL is shown in Fig. 3.12. The facets were left uncoated and the lasers were gold wire bonded and mounted to gold coated copper heatsinks with indium solder. The light output power versus injection current was measured using the same electrical parameters as the FP lasers.

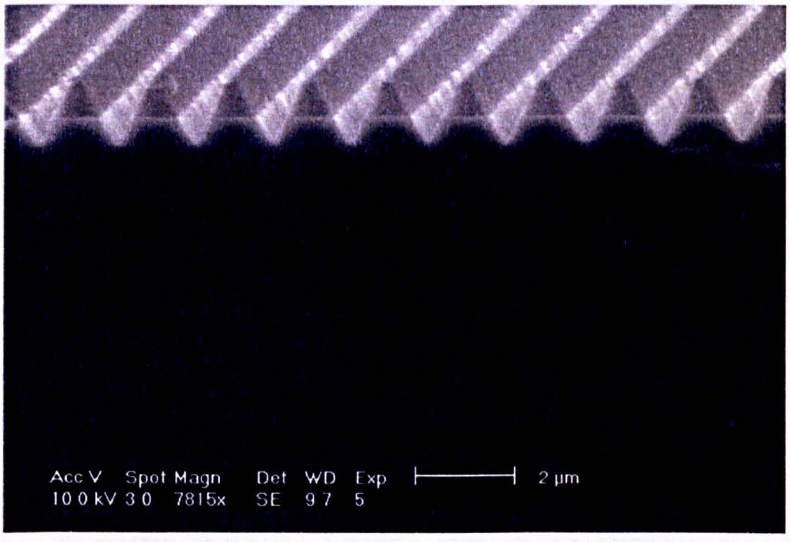

Figure 3.11 *Scanning electron microscope image of the cross section of an inductively coupled plasma etched v-groove grating in the upper cladding layers of a quantum cascade laser structure. The active core region is visible as the lighter section below the grating.*

The room temperature emission spectrum (I = 1.2A) and the LI curve for a 1mm long cavity length 'V-groove' DFB with uncoated facets are shown in Fig. 3.13. The single mode emission wavelength is ~10.2μm. This is very close to the centre of the emission wavelength measured for the FP laser at the same temperature. The effective refractive index is calculated from the measured wavelength and is ~3.04. The threshold current densities for the 'V-groove' and 'square' DFB lasers were measured to be $J_{th} \sim 4.3$ kA / cm^2 ($I_{th} \sim 820$mA) and $J_{th} \sim 4.0$ kA / cm^2 ($I_{th} \sim 770$mA), respectively. These are both less than the equivalent FP laser which had a threshold current density of ~ 4.8 kA / cm^2. This relatively small reduction in the DFB threshold current is due to the additional reflection of the optical mode from the grating.

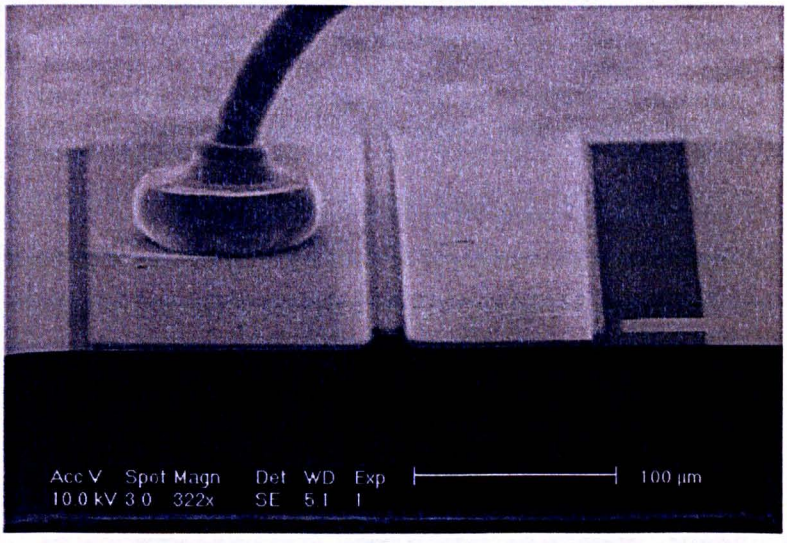

Figure 3.12 *Scanning electron microscope image of a DFB quantum cascade laser. The wet chemical etched laser ridge is visible in the centre of the device with a gold wire (on the left) ball bonded to the electroplated gold contact. The facets are uncoated and the laser is bonded to a gold coated copper heat-sink with indium solder.*

The slightly lower threshold current for the 'square' DFB may be due to the greater coupling strength that is expected for a rectangular shaped grating. Furthermore, the DFB emission is centred with the FP laser spectrum which helps to reduce the lasing threshold and achieve good single mode performance. The side mode suppression ratio was measured to be $\geq$ 25dB for all drive currents.

It was anticipated that the strong interaction of the optical mode with the grating and the metal in the grating grooves would cause the coupling constant to be large and complex. Complex coupled DFB lasers generally exhibit better single mode yield due to the loss component lifting the degeneracy between the two modes on either side of the stop-band. An indication of a strong coupling was the single mode operation of devices with cavity lengths as short as 500μm. In Fig. 3.14 the lasing spectra of two devices of cavity length = 500μm are shown. These 'V' and 'square' DFB devices displayed additional side modes, where it was assumed that these were modes on either side of the stop-band ($\Delta\nu$). This enabled the direct measurement of the coupling coefficient (κ) from the stop-band width. The measured values for the 'V' and 'square' DFB lasers were $\kappa \sim 29\ cm^{-1}$ and $\sim 35\ cm^{-1}$, respectively. This means that the 'V' devices with lengths of ~1mm will have a κL value between (1-3) which is considered suitable for high single mode yields. The larger coupling coefficient is expected for the 'square' profile and both values are in good agreement with the calculated values [Fig. 2.9] where the coupling coefficient is calculated for various grating depths for a 20μm wide ridge. A reduction value for the coupling coefficient of the v-groove grating can be calculated as $(29/35) \approx 0.83$. This is reasonably close to the theoretical reduction value for a triangular grating of $(\pi/4) \approx 0.79$.

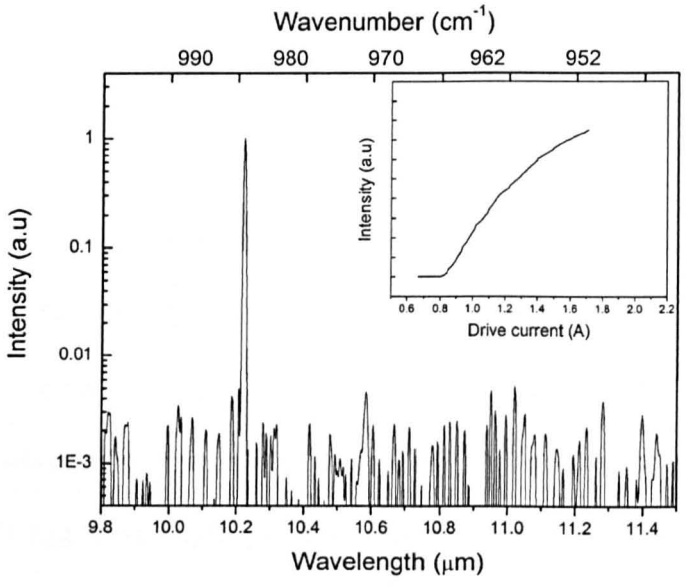

Figure 3.13 *Room temperature emission spectrum (log scale) for a 19μm wide, 1mm long cavity length, 'V' grating DFB quantum cascade laser. Drive current = 1.2A. (inset) Plot of light output power versus drive current. Pulsed electrical operation (100ns pulse width at 5kHz repetition rate) and spectrometer resolution = 0.2cm^{-1}.*

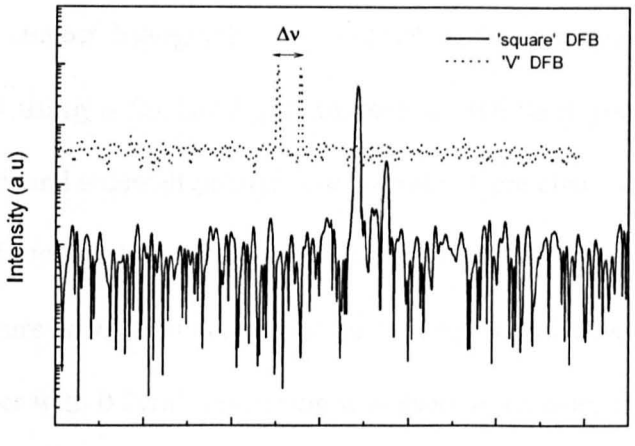

Figure 3.14 *Emission spectra of two DFB lasers with cavity length = 500μm. The 'V' and 'square' grating lasers displaying two peaks assumed to be on either side of the stop-band, Δν. Pulsed electrical operation (100ns pulse width at 5kHz repetition rate) and spectrometer resolution = 0.2cm^{-1}.*

3.5 Ridge width dependence of the lasing wavelength

The ridge width is well known to have an effect on such laser characteristics as threshold current and output power. For mid-infrared DFB QC lasers the ridge width dependence on emission frequency and single mode yield has so far not been discussed in the literature. For DFB lasers the conventional way of selecting the lasing wavelength is by the grating period. However, by changing the ridge width the effective refractive index of a mode propagating in the waveguide can be altered, so changing the Bragg wavelength and the lasing frequency. In this section a V-groove grating with a period = 1.615μm and depth of ~1μm was used with ridge widths of 30, 40 and 50μm. The shorter grating period than used previously, was to show the wavelength dependence on the grating period. Varying the ridge width was to investigate the change in effective refractive index of the optical mode for the different ridge widths.

Samples (wafer MR2045) were processed into ridge lasers and the gratings were fabricated using contact lithography. In contrast to the previous devices the ridges were ICP etched using a $SiCl_4$/Ar gas mixture to maintain good control over etch depth, ridge width and sidewall profile. The samples were cleaved into bars of various cavity length and mounted on gold coated copper heatsinks. The lasers were operated at room temperature with 100ns electrical pulse lengths and a 5kHz repetition rate. A FTIR spectrometer with 0.2cm^{-1} resolution was used to measure the laser spectra.

In Fig. 3.15 the laser spectra for the various ridge widths are shown for a cavity length of 1mm. The inset of Fig. 3.15 shows the spectrum of a 30μm wide laser plotted on a log scale. For this device, the additional side mode on the shorter wavelength side was observed and used to calculate a coupling coefficient of $\kappa \sim 16\ cm^{-1}$ ($\Delta\nu \sim 1.45\ cm^{-1}$).

This is in good agreement with the calculated value of ~20 cm^{-1} for a rectangular grating (~16 cm^{-1} using a reduction factor = $\pi/4$). A shift in emission frequency (wavelength) of $\Delta\nu \sim 4.5cm^{-1}$, ($\Delta\lambda \sim 45nm$) was measured. Therefore, the ridge width dependence was measured to be $(\Delta\nu/dw) \sim -0.22\ cm^{-1}\ \mu m^{-1}$. This dependence would be expected to be even greater for narrower ridges as the effective refractive index change would be greater for ridges with widths similar to the emission wavelength.

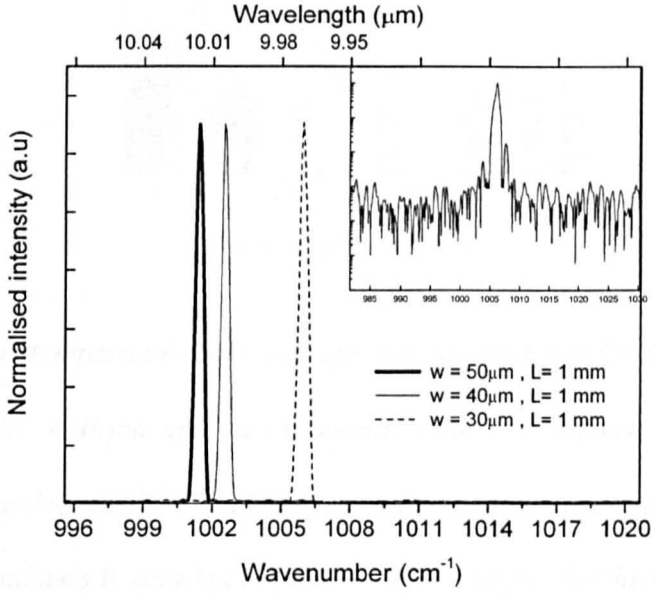

Figure 3.15 *Room temperature emission spectra of DFB quantum cascade lasers with various ridge widths. Pulsed electrical operation (100ns pulse width at 5kHz repetition rate) and spectrometer resolution = 0.2cm^{-1}. (inset) Spectrum of a 30μm wide laser (log scale) showing an additional mode assumed to be on the other side of the stop band to the main peak.*

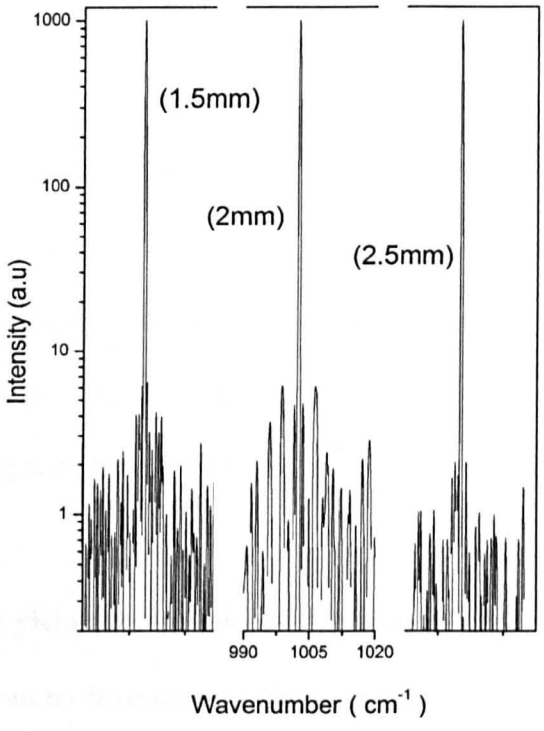

Figure 3.16 *Room temperature emission spectra (log scale) of DFB quantum cascade lasers with widths = 40μm and cavity lengths noted in brackets. Pulsed electrical operation (50ns pulse width at 5kHz repetition rate) and spectrometer resolution = 0.2cm^{-1}. Horizontal axis is split but the scale is identical for the three spectra.*

The measured effective refractive index values for the 30, 40 and 50μm wide lasers were 3.077, 3.087 and 3.091 respectively. These are slightly higher than the value for the ~19μm wide laser (n_{eff} ~ 3.04) previously discussed. The change in effective refractive with ridge width is of significant interest as it may be utilised for tuning the emission wavelength which is desirable for many applications.

Lasers with 40μm wide ridges and various cavity lengths were further characterised. In Fig. 3.16 the spectra for devices of different length are shown. Even though the

longest device (L = 2.5mm) has a calculated value of κL ~ 4, there is no evidence from the spectra of spatial hole burning. The non-uniform intensity profile along the cavity that might be expected from a large κL value may not be as problematic as those associated with interband near infrared wavelength DFB lasers. A larger sample size and investigation would be required to fully assess the effect on single mode yield, but from the devices measured there would not appear to be any degradation of the single mode spectra. This is in agreement with the results of Yu *et al*, [15] where an overgrown grating with large κL values have still produced single mode QCL's.

3.6 Single mode yield and wavelength control of DFB QC Lasers (λ ~10μm) with gratings exposed by interference lithography

A non-trivial part of the fabrication process is the ability to produce gratings with a known and consistent period. Laser written contact lithography masks are commercially available at reasonable cost but will typically have some error in the final feature size (grating period may differ from specification by up to +/- 50nm). E-beam lithography systems have significantly better resolution but have relatively long write times and can have stitching errors. Furthermore, access to e-beam systems can be costly. Although DFB QCLs are well published, the percentage yield of lasers with high SMSR values and the wavelength spread are less well-known.

In this section a laser interference lithography set-up was used to produce the grating with a period chosen to be in good alignment with the material laser gain peak. This grating period was constant over a particular sample area (~200mm^2) with no stitching errors, enabling an investigation of the single mode yield and wavelength spread. This is of significant interest for manufacturing of DFB QCLs where

particularly tight constraints by system manufacturers may be put on the laser wavelength and single mode performance.

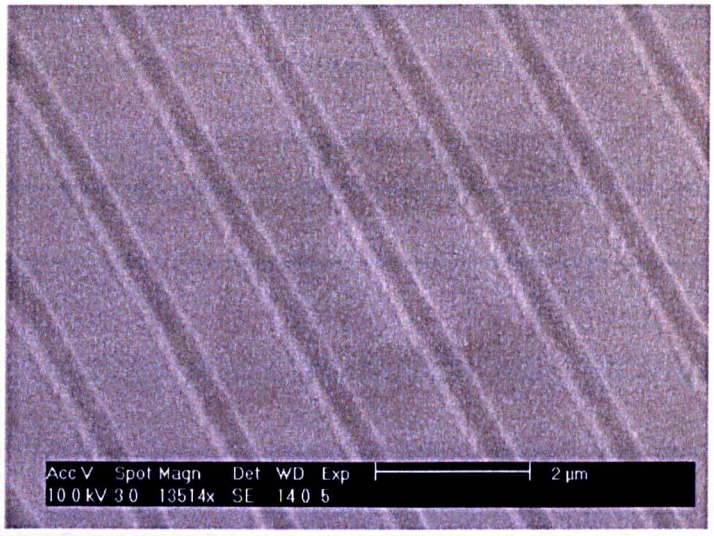

Figure 3.17 *Scanning electron microscope image of a grating produced by holographic interference lithography and transferred into a silicon dioxide layer by reactive ion etching. The grating is situated on quantum cascade laser material. Grating period = 1.628μm.*

For sample (MR2223) a first order grating (Λ = 1.628μm) was exposed in photoresist and transferred to a pre-deposited layer of PECVD silicon dioxide as shown in Fig. 3.17. The SiO_2 layer was etched by ICP etching with a CHF_3 / Ar gas mixture. After removal of the photoresist, the top InP cladding layers were ICP etched with a $SiCl_4$ / Ar gas mixture to a depth of 1.10μm. Due to the nature of the interference lithography exposure, the mark to period ratio was ~ 34%. The laser sample was processed as standard into 45μm wide ridges. The sample was cleaved into bars of 1.5mm cavity length, with the facets left uncoated.

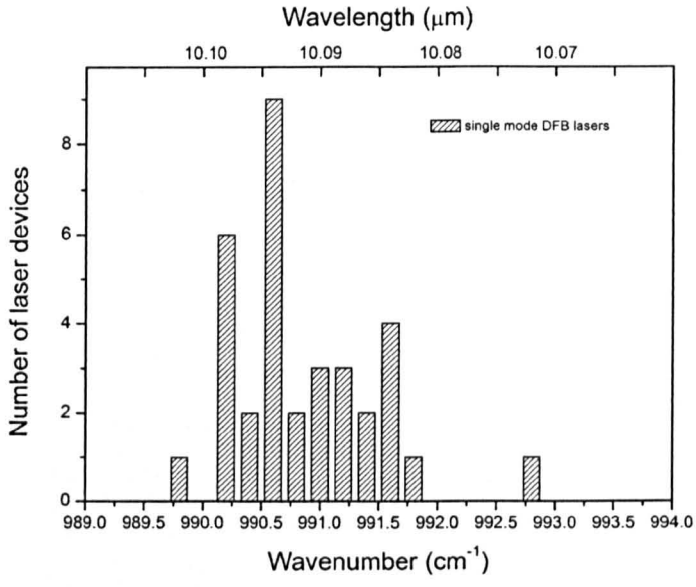

Figure 3.18 *Histogram of the room temperature emission frequencies of 34 single mode DFB quantum cascade lasers characterised in bar form (not mounted) using a single electrical probe. Pulsed electrical operation (50ns pulse width at 5kHz repetition rate). Mean frequency = 990.8 cm^{-1} (standard deviation = 0.63* cm^{-1}*).*

The lasers were operated at room temperature with 50ns electrical pulse lengths and a 5kHz repetition rate. Bar testing lasers (from across a sample) using a single electrical probe on a translation stage allowed 42 individual lasers to be characterised without the need for mounting or wire bonding the samples. In Fig. 3.18 the emission frequencies of lasers measured to be single mode (SMSR $\geq$ 25dB) are plotted to show the spread. Out of the lasers tested, 34 (80%) were single mode with a mean frequency of 990.8 cm^{-1} (standard deviation = 0.63).

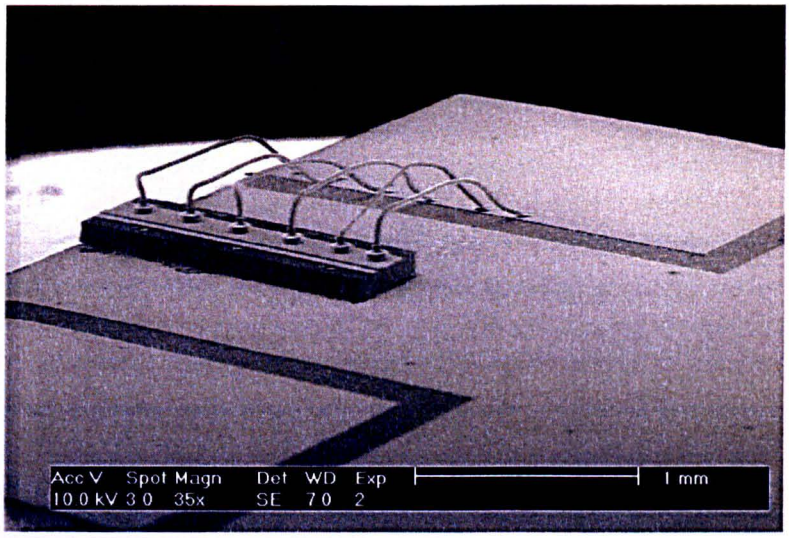

Figure 3.19 *Scanning electron microscope image of an individual DFB quantum cascade laser chip mounted with indium solder to a gold coated aluminium nitride sub-mount. The device has several gold wire ball bonds connecting the gold electroplated contact of the laser to the electrical contact of the sub-mount.*

After bar testing, 15 devices were randomly selected from across the bars and mounted on Aluminium Nitride (AlN) submounts using indium solder. Several gold wire bonds were made to each device. An example of one of the lasers is shown in Fig. 3.19. The laser testing was repeated and the spread in emission frequency is shown in Fig. 3.20. The mean frequency was measured to be 991.6 cm^{-1} (standard deviation = 0.63 cm^{-1}). The small difference in mean frequency between bar and chip testing could simply be experimental error or due to statistical sample size, but a small wavelength increase may be expected due the improved thermal extraction of laser chips mounted on heatsinks with multiple electrical contacts.

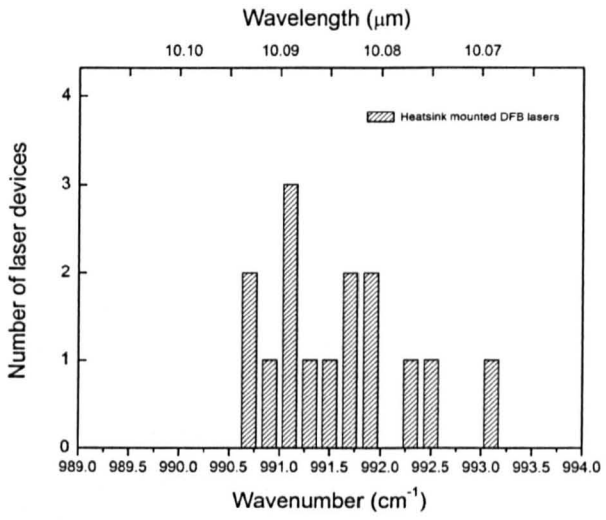

Figure 3.20 *Histogram of the room temperature emission frequencies of 15 single mode DFB quantum cascade laser chips mounted on aluminium nitride sub-mounts. Pulsed electrical operation (50ns pulse width at 5kHz repetition rate). Mean frequency = 991.6 cm^{-1} (standard deviation = 0.66 cm^{-1}).*

In Fig. 3.21 the single mode spectrum from one of the DFB lasers is shown whilst operating at a current of ~ 4A. The side mode suppression ratio was ≥ 25dB for all drive currents. The lack of any additional peak suggests there is significant loss coupling present, reducing the degeneracy of the two peaks either side of the stop band. Although the coupling coefficient could not be measured directly from the spectrum, the calculated value (including reduction factor) from Fig. 2.9 is ~ 19 cm^{-1} ($\kappa L \sim 2.8$). The room temperature L-I curve is shown in the inset of Fig. 3.21. The threshold current density was measured to be ~ 3.8 kA/cm^2 (Ith ~ 2.6A). Peak pulse output powers of up to 220mW were measured using a thermopile detector placed directly in front of the laser facet. At temperature = 293K the measured slope efficiency (dP/dI) was ~ 200 mW/A.

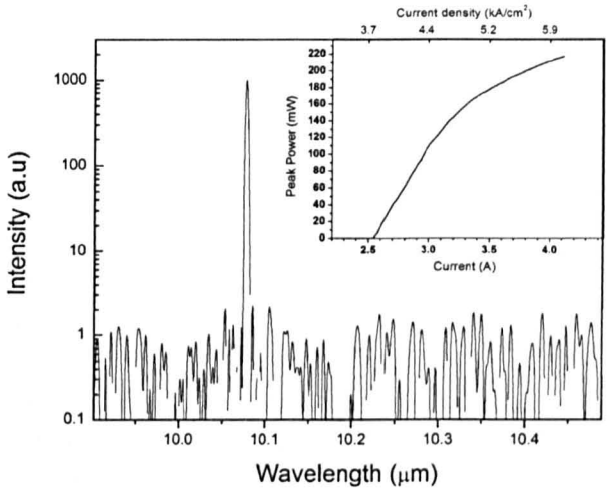

Figure 3.21 *Room temperature emission spectrum (log scale) for a 45μm wide, 1.5mm long cavity length DFB quantum cascade laser mounted and bonded to a aluminium nitride heatsink.. Drive current = 4A. (inset) Plot of light output power versus drive current. Pulsed electrical operation (50ns pulse width at 5kHz repetition rate) and spectrometer resolution = 0.2 cm^{-1}.*

3.7 Summary

Single mode quantum cascade lasers (λ ~ 10 μm) operating at room temperature with high output powers and utilising metalised surface gratings are demonstrated. A v-groove shaped grating profile was achieved using a resist mask and a process developed using ICP etching. The dry etch process allows deeper gratings than using wet chemical etching and is quicker than using dielectric or metal etch masks. The coupling coefficient may be slightly lower than compared to a rectangular shaped grating but side mode suppression ratio is not significantly affected. It may also be beneficial to end facet quality during the cleaving process. A design optimised for wavelength control using a grating produced by interference lithography and with a single mode yield of 80%, was demonstrated. This design shows the potential for a

high single mode yield and shows that bar testing devices with a single probe is a quick and suitable method for screening the devices.

3.8 Future Work

Development of high reflectivity coatings would help to lower threshold currents and achieve continuous wave (cw) operation. Although cw operation is not always necessary for spectroscopic applications it would be useful to investigate the effects on wavelength, SMSR and single mode yield. Further investigation on the benefits of a v-groove grating profile would also be beneficial. As shown, the coupling coefficient is altered for different grating profiles, so it is also likely that the loss component will differ as well. A more rigorous investigation is also required to assess the yield benefits of different lithographic methods for exposing the gratings.

3.9 References

[1] Faist, J., Gmachl, C., Capasso, F., Sirtori, C., Sivco, D.L., Baillargeon, J. N., Cho, A. Y.: 'Distributed feedback quantum cascade lasers', Appl. Phys. Lett. 1997, 70, 20, pp. 2670-2673

[2] Hofstetter, D., Faist, J., Beck, M., Muller, A., Oesterle, U., 'Demonstration of high-performance 10.16μm quantum cascade distributed feedback lasers fabricated without epitaxial regrowth', Appl. Phys. Lett, 1999, 75, 201114

[3] Kohler, R., Gmachl, C., Capasso, F., Tredicucci, A., Sivco, D.L., Cho, A.Y.: 'Single-mode Tunable Quantum Cascade Lasers in the Spectral Range of the CO_2 Laser at $\lambda = 9.5\text{-}10.5\mu m$', IEEE Phot. Lett. 2000, vol.12, no.5, pp. 474-476

[4] Green, R.P., Wilson, L.R., Zibik, E.A., Revin, D.G., Cockburn, J.W., Pflügl, C., Schrenk, W., Strasser, G., Krysa, A.B., Roberts, J.S., Tey, C.M., Cullis, A.G.: 'High-performance distributed feedback quantum cascade lasers grown by metalorganic vapor phase epitaxy,' Appl. Phys. Lett. 2004, 85, pp. 5529-5531

[5] Stern, M.B. and Liao, P.F., 'Reactive ion etching of GaAs and InP using $SiCl_4$', J. Vac. Sci. Technol. B. 1983, 1, 1053–5

[6] Fujiwara, Y., Kikuchi, K., Hashimoto, M., Hatate, H., Imai, T., Takeda, Y., Nakano, H., Honda, M., Tatsuta, T., Tsuji, O., 'Fabrication of Two-Dimensional InP Photonic Band-Gap Crystals by Reactive Ion Etching with Inductively Coupled Plasma', Japan. J. Appl. Phys. 1997, 136, 7763–8

[7] Etrillard, J., Ossart, P., Patriarche, G., Juhel, M., Bresse, J.F, and Daguet, C, 'Anisotropic etching of InP with low sidewall and surface induced damage in inductively coupled plasma etching using $SiCl_4$', J. Vac. Sci. Technol. A, 1997, 15, 626–32 (part 1)

[8] Shul, R.J., McClellan, G.B., Briggs, R.D., Rieger, D.J., Pearton, S.J.,

Abernathy, C.R., Lee, J.W., Constantine, C., and Barratt, C., 'High-density plasma etching of compound semiconductors', J. Vac. Sci. Technol. A., 1997, 15, 633–7 (part 1)

[9] Matsutani, A., Koyama, F., Iga, K., 'Low Bias Voltage Dry Etching of InP by Inductively Coupled Plasma Using $SiCl_4/Ar$', Jpn. J. Appl. Phys. 1998, 1, 37, (12A): 6655-6656

[10] Matsutani, A., Ohtsuki, H., Muta, S., Koyama, F., Iga, K., 'Mass Effect of Etching Gases in Vertical and Smooth Dry Etching of InP', Jpn. J. Appl. Phys, 2001, 1, 40, (3A): 1528-1529

[11] Lee, B.T., Park, J.S., Kim, D., Ahn, J., 'Characterization of heavy deposits on InP mesa sidewalls reactive ion etched using CH_4/H_2 plasma', Semicond. Sci. Technol.1999, 14, 345–

[12] Streifer, W., Scifres, D.R., Burnham, R.D., 'Coupling coefficients for distributed feedback single and double hetrostructure diode lasers', IEEE J. Quantum Electron. 1975, 11, 867–72

[13] Wang, J., Thompson, D.A., Simmons, J.G., 'Wet Chemical Etching for V-grooves into InP Substrates', J. Electrochem. Soc. 1998, 145, 2931–7

[14] Charles P M 2002 US Patent 6335 559 Hewlett-Packard Company

[15] Yu, J.S., Slivken, S., Darvish, S.R., Evans, A., Gokden, B., Razeghi, M.: 'Distributed feedback quantum cascade lasers', Appl. Phys. Lett. 2005, 87, 041104

Chapter 4 - Distributed Feedback Quantum Cascade Lasers (λ ≈ 10μm) with Deep Etched Lateral Gratings

4.1 Introduction

This chapter presents a distributed feedback quantum cascade laser device previously undemonstrated in the Indium Phosphide material system. Details of the design, fabrication and characterisation for single-mode QC lasers operating above room temperature are presented. The design utilises a novel multi-etch process developed to achieve double-sided, deep etched lateral gratings. Gratings for these devices were etched in the sidewalls of the laser ridge using inductively coupled plasma (ICP) etching.

A significant amount of device fabrication time is spent on defining the grating for a DFB laser. The grating is typically etched in to the top surface of the ridge laser [1-4]. An alternative method is to etch a grating close to the active core region and then subsequently use an epitaxial overgrowth step to infill the grating [5]. By fabricating the lateral gratings simultaneously with the ridge, processing time and cost is significantly reduced. A lateral grating design has previously been published for GaAs-based near infrared, interband lasers [6,7] and for QC lasers based on the GaAs material system [8]. The use of InP-based materials is advantageous due to superior wave-guiding, high thermal conductivities and the effective mass of the material. However, processing technologies for this material system are less mature. Therefore, the novel etching processes and devices demonstrated in this chapter are of significant

interest. Since the top of the ridge is left planar, surface plasmon effects [9,10] at even longer wavelengths can have significant influences on QC device performance [11,12] and so they may be investigated without the interaction of a top surface grating. The material MR2223 (layer structure described in chapter 1) was grown by metal organic vapour phase epitaxy (MOVPE), which has advantages for economical mass production. The four-well active region structure is based on a double-phonon resonance design.

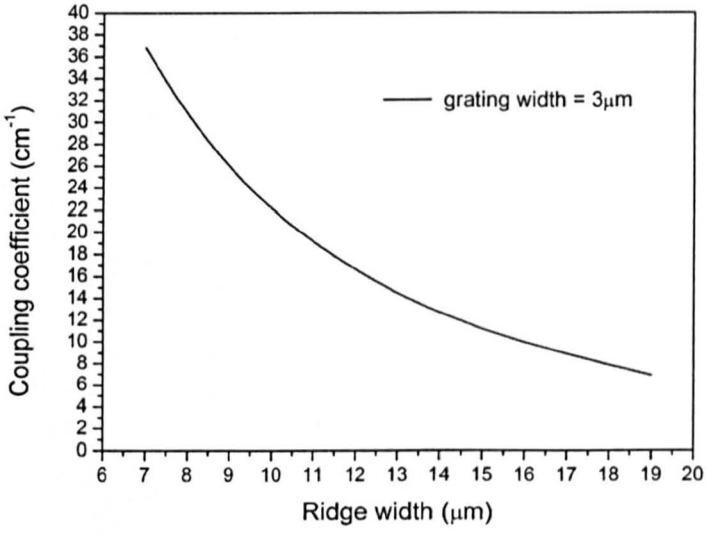

Figure 4.1 *Plot of the calculated coupling coefficient versus the laser ridge width for (λ ~10μm) lateral grating distributed feedback quantum cascade lasers. Grating width d_g=3μm.*

4.2 Modelling

An explanation of the general design and methods used for modelling these devices is described in chapter 2. A value for the strength of the grating (coupling coefficient, κ) is required for designing the grating dimensions. For lateral grating lasers, this will

determine the laser ridge width and the grating width. Using commercially available software, the effective refractive indices of transverse modes propagating in the lateral grating structure can be calculated. As can the confinement of a particular optical mode in the grating layer. These allow the estimation of the coupling strength. In Fig. 4.1 the calculated coupling strength for the fundamental transverse mode is shown as a function of the ridge width, for a constant grating width. From this we can see that kappa (κ) increases more rapidly as the ridge width decreases. Narrow ridge widths (similar to the emission wavelength) will suppress higher order transverse modes propagating in the waveguide due to the greater waveguide losses. However, for ridge widths narrower than the wavelength, a large loss will also be experienced by the fundamental transverse mode, reducing device performance.

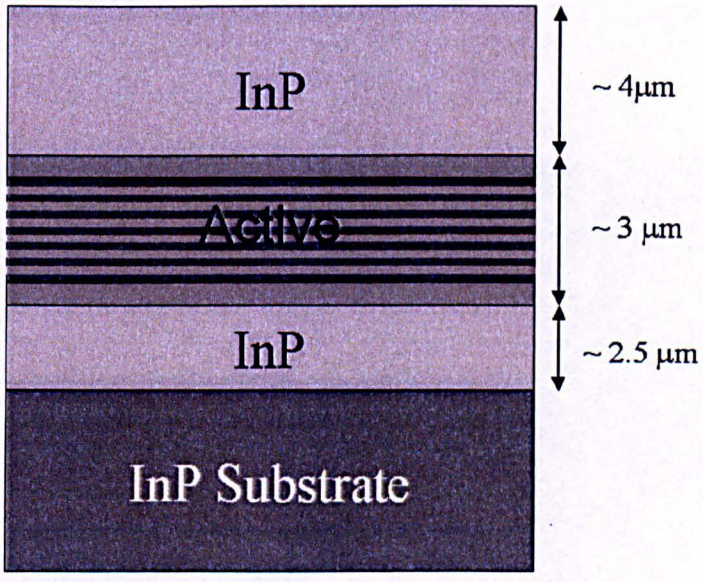

Figure 4.2 *Schematic diagram of a simplified quantum cascade laser structure. Diagram shows the InP cladding layers and the active core region containing the InGaAs / AlInAs quantum wells (not to scale).*

4.3 Fabrication / Process development

The active region containing AlInAs / InGaAs quantum wells and the doped InP waveguide are shown in Fig. 4.2. The materials have appreciably different etch rates and surface morphology for certain etch chemistries. Therefore, the development of a high aspect ratio, multi-stage, inductively coupled plasma (ICP) etch process was crucial to achieving deep etched lateral DFB devices. To obtain a smooth, vertical grating in the active region the etch depth was required to be ~9μm or more. To achieve such a depth the etch selectivity needed to be sufficiently high and so a silicon dioxide (SiO_2), dielectric mask, was favoured. The SiO_2 layer (thickness = 800nm) was deposited by plasma enhanced chemical vapour deposition (PECVD). After spin coating the sample with Microposit SPR350 photoresist, conventional contact lithography (optics optimised for ~300nm wavelength exposure) was employed to pattern the sample with the rib waveguide (grating period, $\Lambda = 1.68\mu m$).

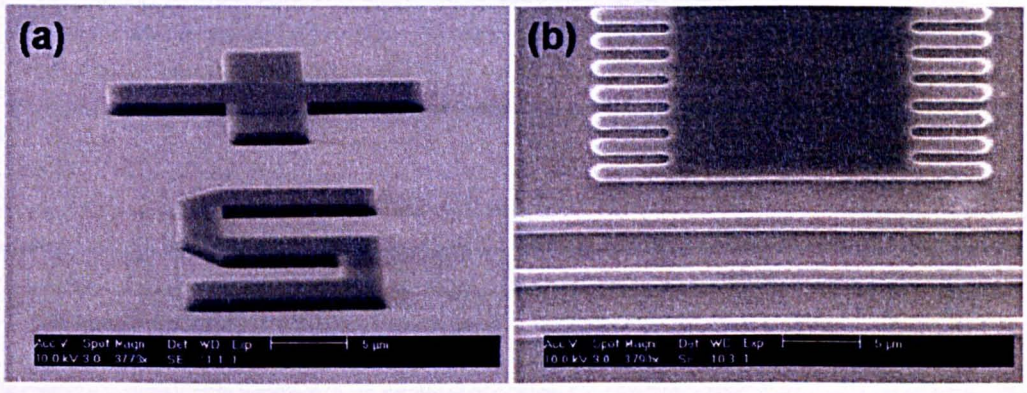

Figure 4.3 *SEM images of (a) Alignment key, defined in a SiO_2 mask using contact lithography and reactive ion etching and (b) lateral grating ridge structure defined in SiO_2. RIE process parameters: CHF_3 / Ar gas flows (20 / 30) sccm, RF power = 200W, Pressure = 25 mTorr.*

After development of the photoresist the pattern was transferred into the SiO_2 layer by reactive ion etching (RIE). Using a CHF_3 / Ar chemistry, the process was optimised to gain a smooth vertical etch profile as shown in Fig. 4.3. A photoresist to SiO_2 selectivity of ~1:4 was measured with a scanning electron microscope. The time to completely etch through the SiO_2 mask was approximately 50 minutes. After the dielectric etch was complete the remaining photoresist on the sample was removed using an oxygen plasma ash, ready for the semiconductor etch.

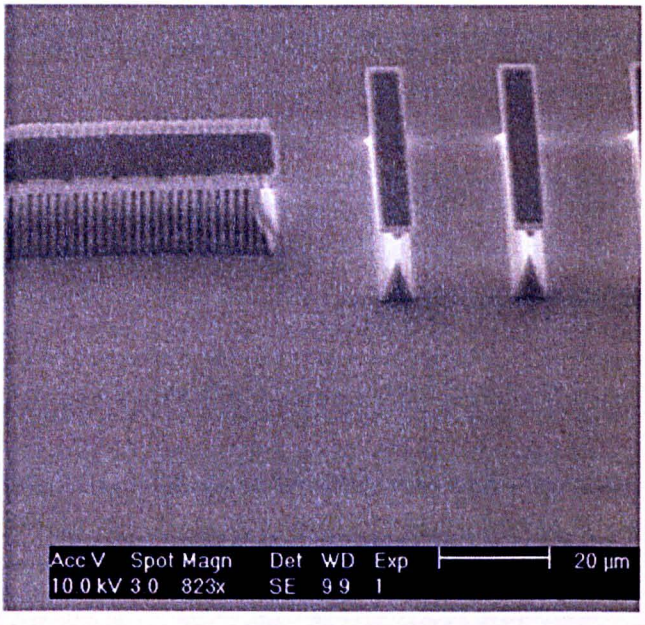

Figure 4.4 *SEM image of ridge structure with lateral gratings. InP substrate was etched using ICP and a SiO_2 mask. Process parameters: Cl_2 / Ar gas flows (15 / 12) sccm, RF / ICP power (250W / 350W), Pressure = 2mTorr, no helium cooling. Table temperature set to 25°C.*

The following series of scanning electron microscope images show the process development and effect of changing various parameters such as gas flow ratio, RF /

ICP powers and substrate temperature. Fig. 4.4 shows the result of a process recipe that contains a higher Chlorine flow rate than Argon. The pressure is kept low (2 mTorr) to help achieve a high aspect ratio etch. Although the etch surface is smooth there is a considerable amount of horizontal etching (undercutting of the mask). Therefore, we have too much of a chemical etch process and the etching in the horizontal direction has almost completely etched through the feature. To reduce the chemical etching mechanism, the flow rate of Chlorine was reduced by approximately half. The effect of this can be seen in Fig. 4.5. The amount of etching in the horizontal direction (undercutting) has been reduced and the surface morphology still remains smooth. The verticality of the sidewall is generally good but there is still excessive undercutting close to the mask at the top of the lateral gratings. The vertical etch rate compared to the horizontal etching still needs to be improved.

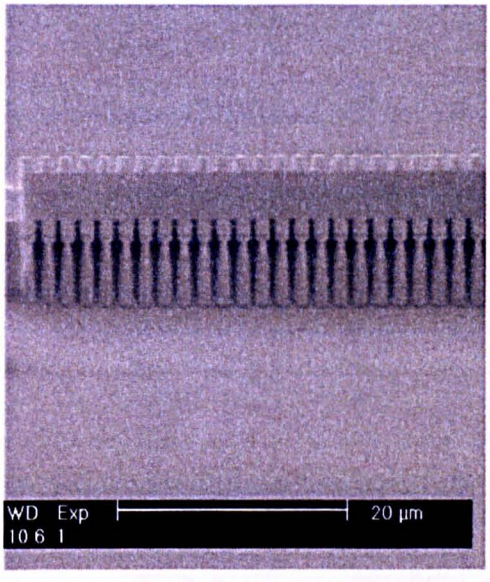

Figure 4.5 *SEM image of ridge structure with lateral gratings. InP substrate was etched using ICP and a SiO_2 mask. Process parameters: Cl_2 / Ar gas flows (7 / 12) sccm, RF / ICP power (250W / 350W), Pressure = 2mTorr, no helium cooling. Table temperature set to 25°C.*

Further reduction in Chlorine flow rate was not attempted as the mass flow controllers (MFCs) installed on the ICP machine were not as reliable operating with a lower flow rate than 7 sccm.

Since the reactive Chlorine species will form etch products of type, InClx and PClx, these etch products need to be removed from the surface to allow further chemical etching to take place and keep the vertical etch rate suitably high. The InClx etch products are non-volatile with a much higher boiling point than PClx etch products. A high temperature would normally be expected to be required to remove the etch products from the surface. However, the table temperature was set at 25°C and the actual table temperature recorded by the system was typically <30°C. The role of Argon in the process was thought, mainly to enhance the physical sputtering mechanism (ion bombardment) to remove the etch products. However, to investigate the effect of localised heating at the wafer surface (aided by the Argon sputtering) another sample was etched under the same conditions (as described for Fig. 4.5) but the helium substrate cooling was set to a flow rate of 5.8 sccm and the wafer sample was held to the silicon substrate holder wafer using fomblin oil. This would help with thermal extraction and should reduce the wafer sample surface temperature during etching if localised heating was a significant factor. As seen in Fig. 4.6, the vertical profile of the sidewalls is not a steep, as with the Helium cooling turned off. Also, the surface morphology is rougher and the etch rate was reduced by approximately a factor of 4. This shows that the rate of desorption of the etch products is affected by localised heating of the substrate and can be used to achieve faster etch rates, smooth morphology and vertical sidewalls when etching InP.

A successful process for etching InP using a Cl_2 / Ar atmosphere achieving smooth, vertical etching and good etch selectivity is shown in Fig. 4.7. This was achieved using equal ICP and r.f powers (250W). The Chlorine / Ar flow rates where 7 / 12 sccm and the pressure was 2 mTorr. With no helium cooling the InP etch rate was ~ 400 nm / minute. The darker material visible at the top of the feature is the silicon dioxide masking layer (etch rate ~ 20 nm / minute). However, when the process was transferred on to the full QCL (InP / AlInAs / InP) structure the vertical etching and good definition of the lateral gratings were lost. This was due to the different etch rates of the InP waveguide and the active region materials. A similar etch rate and a good morphology for the different layers was obtained by switching to a $SiCl_4$ / Ar atmosphere. An excessive amount of mask etching reduced the selectivity and some undercutting of the mask was evident as shown in Fig. 4.8.

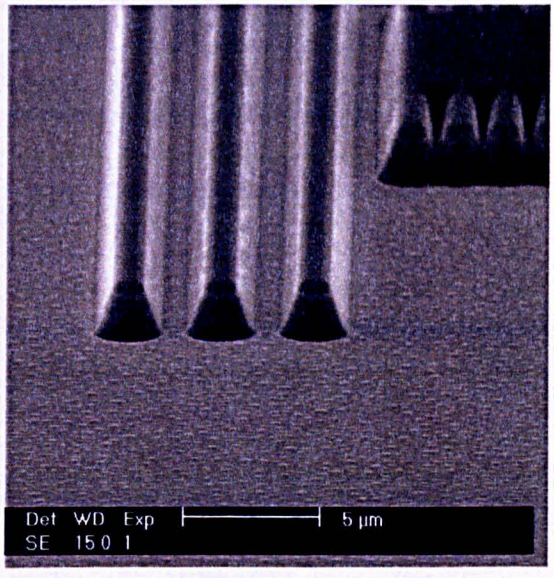

Figure 4.6 *SEM image of ridge structure with lateral gratings. InP substrate was etched using ICP and a SiO_2 mask. Process parameters: Cl_2 / Ar gas flows (7 / 12) sccm, RF / ICP power (250W / 350W), Pressure = 2mTorr, helium cooling = 5.8 sccm, Table temperature set at 25 °C.*

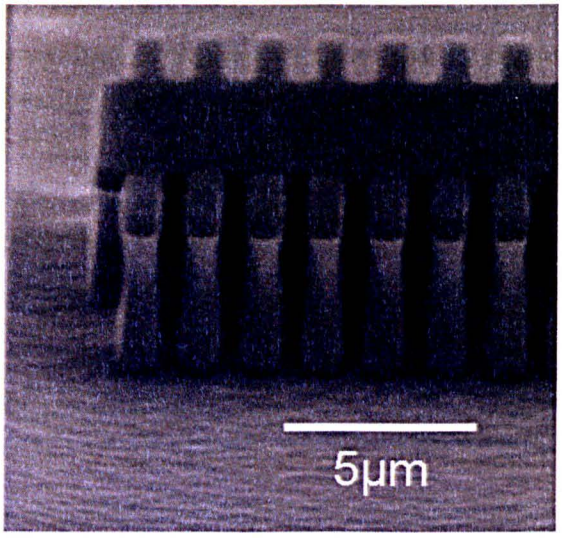

Figure 4.7 *SEM image of ridge structure with lateral gratings. InP substrate was etched using ICP and a SiO_2 mask. Process parameters: Cl_2 / Ar gas flows (7 / 12) sccm, RF / ICP power (250W / 250W), Pressure = 2mTorr, no helium cooling. Table temperature set to 25°C.*

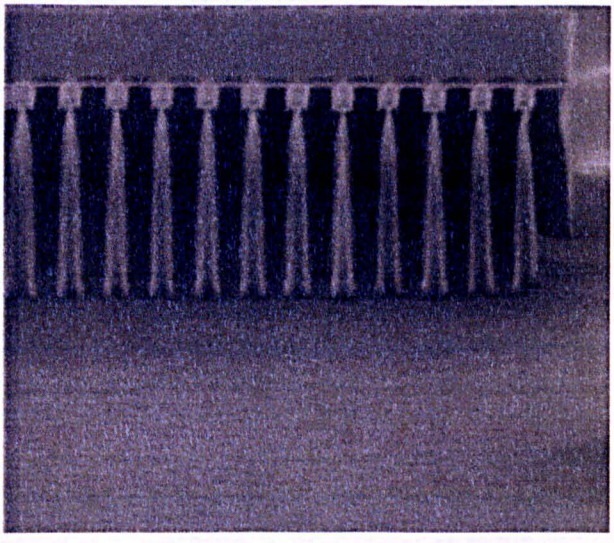

Figure 4.8 *SEM image of ridge structure with lateral gratings. InP substrate was ICP etched using a SiO_2 mask. Process parameters: $SiCl_4$ / Ar gas flows (8 / 30) sccm, RF / ICP power (220W / 1000W), Pressure = 2mTorr, No helium, Table temperature set to 25°C.*

This initiated the development of a multi-stage etch process utilising the two different etch chemistries. The result was a high aspect ratio etch with a smooth vertical etch profile and a suitable etch rate. The final process incorporated two etches. Firstly, a Cl_2 / Ar (etch rate ~ 430nm/min) followed by an etch using $SiCl_4$ / Ar (etch rate ~ 1μm/min). The chamber pressure was 2mTorr and table temperature was 25°C. The rf powers / ICP powers were (300W / 500W) and (220W / 1000W) respectively. The sample was not removed from the ICP chamber after the first etch. A 5 minute pump down was used between the two etch recipes to evacuate the chamber and so the total etch time including the pump down was 23 minutes. A semiconductor to mask selectivity >15:1 was achieved. In Fig. 4.9, the smooth morphology and vertical etching of the ribbed QCDFB structure is shown. The remaining dielectric mask was removed in HF acid, before a Silicon Nitride dielectric layer (300nm) was deposited

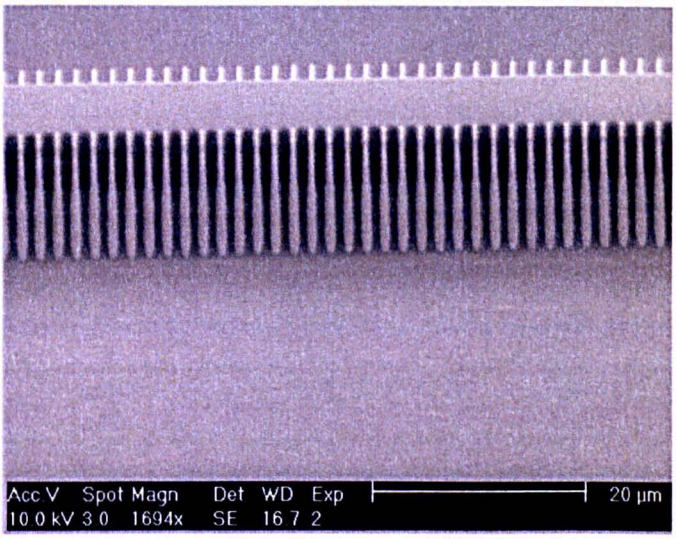

Figure 4.9 *SEM image of ridge structure with lateral gratings. The QCL sample was ICP etched using a SiO_2 mask and a multi-stage process. A Chlorine and Argon etch (7 / 12) sccm was followed an etch using a $SiCl_4$ / Argon gas mixture. A 5 minute evacuation of the chamber was used in-between the two etch processes.*

by PECVD for electrical isolation. As shown in the optical microscope image in Fig. 4.10(a), the contact window was opened in the dielectric layer using standard photolithography and reactive ion etching using CHF_3 / 0_2. Titanium and gold (20nm / 200nm) electrical contacts were thermally evaporated onto the sample. The device at this stage is shown in Fig. 4.10(b). A partially electroplated device is shown in Fig. 4.11(a), to display the lateral gratings more clearly. Approximately 1μm of gold was electroplated on to the sample before Ti / Au back contacts were thermally deposited after thinning the sample to ~180μm. Fig. 4.11(b) shows a scanning electron microscope (SEM) image of a fully processed device with un-coated cleaved facets.

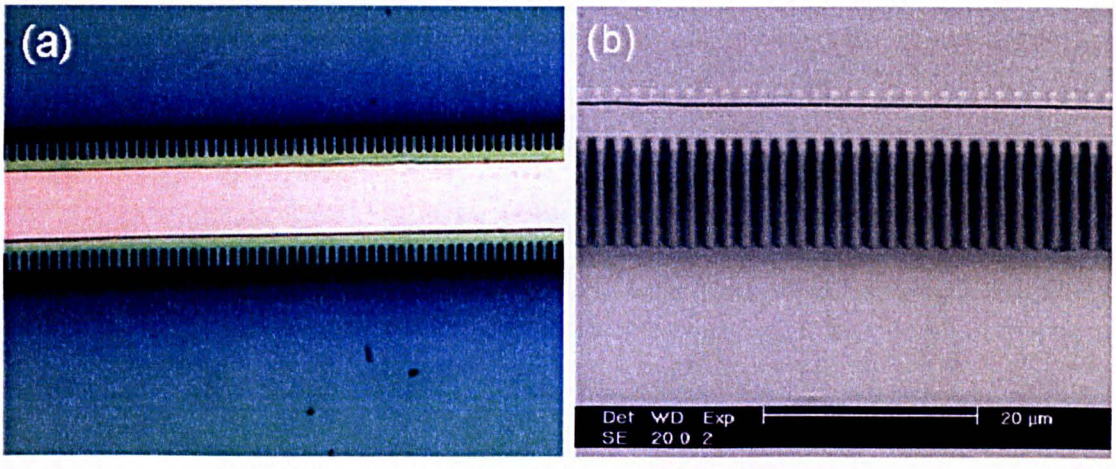

Figure 4.10 *Optical microscope image of quantum cascade DFB laser with lateral gratings after contact window was etched using reactive ion etching. (b) SEM image of device after contact window has been defined and Ti/Au contacts have been thermally evaporated on to sample.*

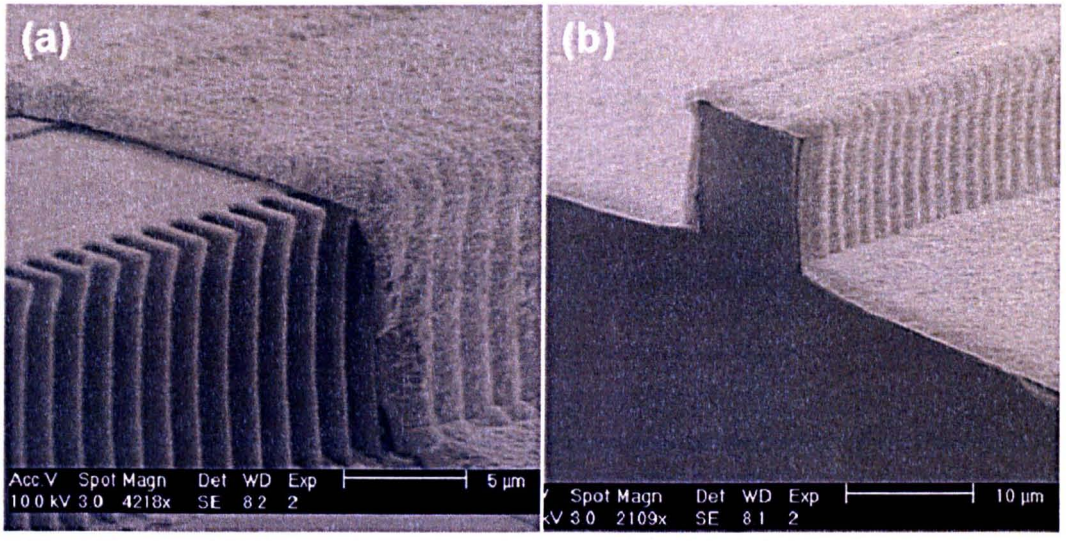

Figure 4.11 *SEM images of fully processed quantum cascade DFB ridge devices with lateral gratings. (a) part electroplated ridge (b) fully processed device with uncoated cleaved facets.*

4.4 Fabry-Perot devices

Several variations of the device design were incorporated into the mask design for the processed sample. Fabry-Perot (FP) lasers with ridge widths of 9μm and 14μm were simultaneously fabricated on the sample (using a multi-stage, inductively coupled plasma etch as detailed earlier in this chapter) with DFB devices of very similar dimensions. This allowed the direct comparison of the DFB designs with their corresponding FP devices. The wafer was then cleaved into bars and each bar then soldered with indium on to gold-coated copper blocks. Several devices were then gold wire bonded, ready for testing. Using an electrical pulse length of 25ns and repetition rate of 5kHz, the device emission spectra were measured using a Fourier transform infra-red (FTIR) spectrometer with a resolution of $0.2cm^{-1}$.

FP devices of various lengths and ridge widths were measured at room temperature and their threshold current densities are plotted in Fig. 4.12. The transparency threshold current density (J_0) for both ridge widths is ~ 2.8 kA/cm^2. As can be seen from the plot, the value for the 9μm wide ridge is slightly higher than for the 14μm ridge due to the increased waveguide losses, hence the higher threshold values for narrower ridges. The decrease in threshold going from short to long devices is caused by the lower mirror losses due to the reduced influence of the uncoated mirrors for the longer devices. From the measured spectrum for a FP laser, shown in Fig. 4.13, the emission wavelength was observed to be ~ 10μm. Using the measured longitudinal mode spacing ($\Delta\nu_{long} = 1/ 2\ L\ n_g$) and the cavity length (L) = 0.95mm, the group refractive index (n_g) was determined to be ≈ 3.55.

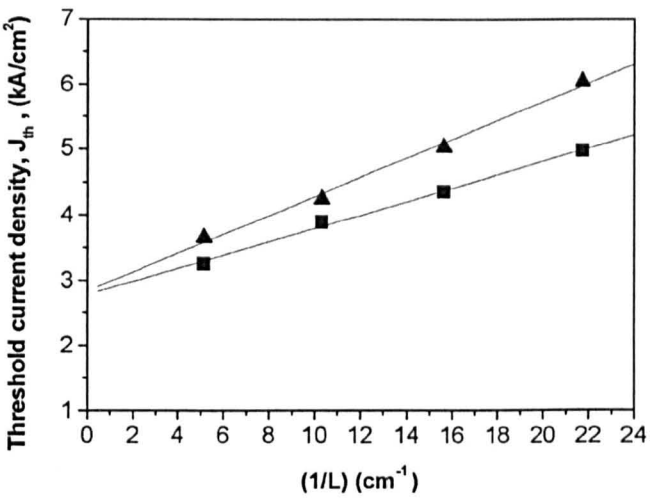

Figure 4.12 *Plot of the inverse cavity length vs. threshold current density for uncoated FP lasers of various lengths. Lasers with ridge widths = 14μm (squares) and with ridge widths = 9μm (triangles) are plotted. J_0 is <3kA/cm^2 in both cases. Results measured at room temperature, (25ns pulse width, 5kHz repetition rate)*

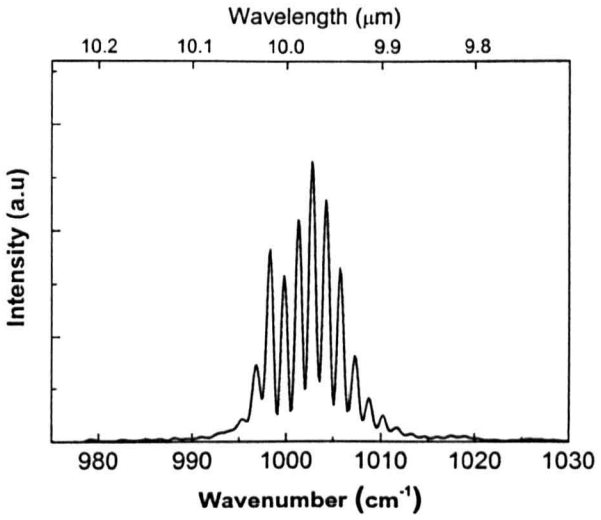

Figure 4.13 *Room temperature emission spectrum of a quantum cascade Fabry-Perot laser. Cavity length = 0.95mm. Emission wavelength ~ 10μm.*

4.5 Distributed feedback lasers

As mentioned in the previous section on FP lasers, DFB devices were fabricated simultaneously on the same sample. Using an FTIR spectrometer, single mode laser emission with was measured for DFB devices operating at room temperature for currents well above threshold. For the 9μm (λ ~ 9.9μm) and 14μm (λ ~ 10.1μm) wide ridges the full width at half maximum linewidth (FWHM) was ~ 0.3cm^{-1} (limited by the resolution of the spectrometer). The effective refractive index at room temperature, (n_{eff} = λ / 2Λ), (Λ=1.68μm) was calculated to be (≈ 2.95) and (≈ 2.99) for the 9μm and 14μm ridges respectively. Further emission spectra measurements were carried out on the two devices with length = 0.65mm. The ridge widths were 9μm and 14μm and the grating widths were 3μm and 1μm respectively. From this point, these devices will be referred to as 9_3 and 14_1. For both devices the observed change in main peak wavelength over a temperature range of 190K to 330K is linear, with a tuning coefficient measured to be –0.067 cm^{-1} K^{-1} as shown in Fig. 4.14. This

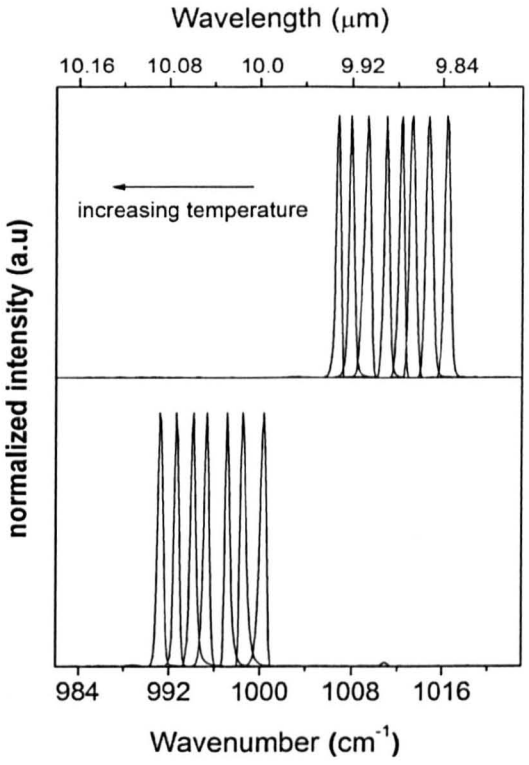

Figure 4.14 *Emission spectra of lateral grating DFB quantum cascade lasers, measured using a FTIR spectrometer with resolution = 0.2cm^{-1}. The ridge widths were 9μm (bottom) and 14μm (top). The spectra demonstrate a shift to longer wavelengths with increasing temperature (190K-330K). The tuning coefficient is measured to be –0.067 cm^{-1} K^{-1}.*

is very similar to the tuning coefficient measured for metalised surface grating DFBs previously reported around this wavelength [2,4]. In Fig. 4.15, the offset of the two plots shows the dependence of the wavelength with the ridge width (w), for devices 9_3 and 14_1 with ($d\nu/dw \approx 3cm^{-1}$ / μm). This dependence can be attributed to the fact that the guided optical mode will have some overlap with the dielectric and metal layers covering the ridge sidewalls. This overlap will be greater for the narrower ridge causing a modification of the effective refractive index (n_{eff}). The side mode

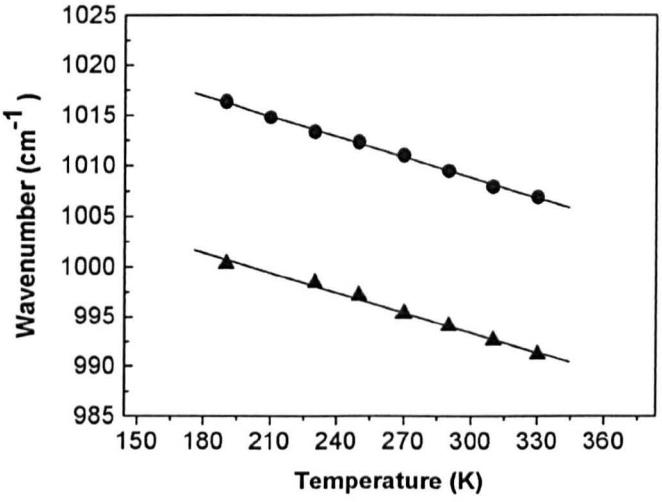

Figure 4.15 *Laser emission frequency for single mode devices with cavity length = 640μm. Line through data points shows linear tuning of emission with temperature. Circles represent a device with ridge width = 9μm and triangles represents a device with ridge width = 14μm*

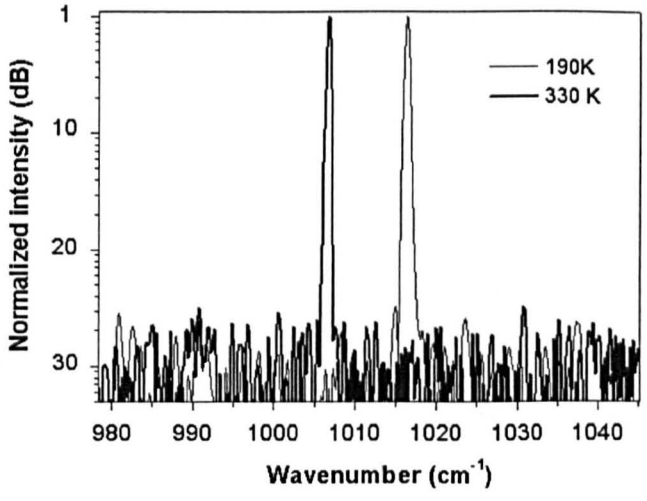

Figure 4.16 *Laser emission spectra plotted on a logarithmic scale for device 9_3. Measurements taken above threshold current for pulsed operation (25ns pulse width, 5kHz repetition rate) at temperatures of 190K and 330K. Side mode suppression ratio >25dB.*

suppression ratio (SMSR) for 9_3 was greater than 25dB for temperatures higher than 190K as shown in Fig. 4.16. Below this temperature multiple modes were present which is attributed to the reduction in the overlap between the Bragg resonance in the grating and the material laser gain peak at low temperatures.

In Fig. 4.17, we see a plot of the light output power versus injection current for a 9μm wide ridge DFB laser at the operating temperatures of 250K and 293K. The threshold current densities and (slope efficiencies) at 293K were ~ 8.5 kA/cm^2 (~ 60 mW/A) and at 250K they were ~ 6.5 kA/cm^2 (~ 85 mW/A) for drive currents in the range of 10 - 50 % above laser threshold. The side mode suppression ratio (SMSR) for 14_1 was >25dB at room temperature and above for a limited drive current range. The device did not operate in a single mode for temperatures below 290K. In Fig. 4.18 we see a plot of the light output power versus injection current at the operating temperatures of 250K and 293K. The drive current range for single-mode operation is indicated by solid lines. Dashed lines indicate multi-mode operation. The threshold current densities and (slope efficiencies) at 293K were ~ 6.8 kA/cm^2 (~ 80mW/A) and at 250K they were ~ 4.8 kA/cm^2 (~ 100 mW/A). As is the case with the other DFB devices tested, this is higher than the threshold current density for a FP device of very similar dimensions.

From the coupled wave theory it would be expected that a DFB device would have a higher value of coupling coefficient (κ) than the FP device ($\kappa = 0$) and that this would result in a lower threshold current density than that of the FP device. However, this does not take into account damping in the dielectric and metal layers, occurring in the mid-infrared. Furthermore, the performance of the DFB devices reported here are not

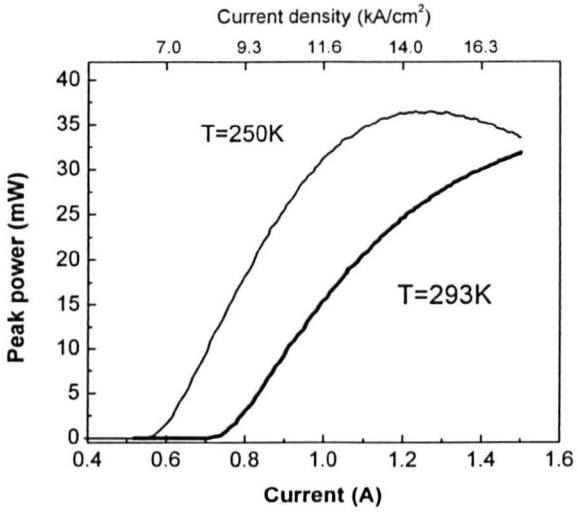

Figure 4.17 *Plot of the injection current versus peak output power for an un-coated lateral grating DFB laser with ridge width = 9μm. Results are for pulsed operation (50ns pulse width at 5kHz repetition rate) at the heat sink temperatures of 250K and 293K.*

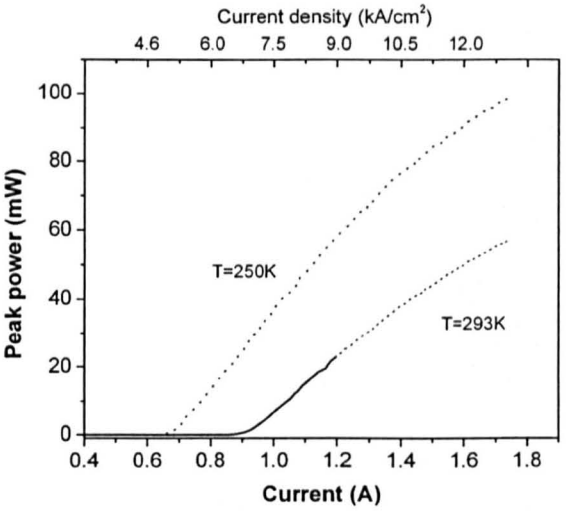

Figure 4.18 *Plot of the injection current versus peak output power for an un-coated lateral grating DFB laser with ridge width =14μm. Results are for pulsed operation (50ns pulse width at 5kHz repetition rate) at the heat sink temperatures of 250K and 293K. Solid lines represent single mode operation. Dashed lines represent device lasing in more than one mode.*

expected to be optimised for power output as they are expected to be lasing close to the edge of the laser gain spectrum rather than close to the gain peak. In Fig. 4.19 the emission spectra is shown for a 14μm wide DFB at the temperature of 250K. The occurrence of a higher order mode (different Bragg condition) is visible at a significantly shorter wavelength than the main peak. This second peak becomes more prominent as the material laser gain peak shifts to a lower wavelength and overlaps with the higher order resonant mode. Therefore, the inferior single mode performance of 14_1 compared to 9_3 is attributed to the poorer overlap with the laser gain peak, reduced coupling coefficient and the higher order resonant modes associated with the wider ridge width. The higher order modes can have a greater coupling coefficient than the fundamental transverse mode as shown in Fig. 2.13.

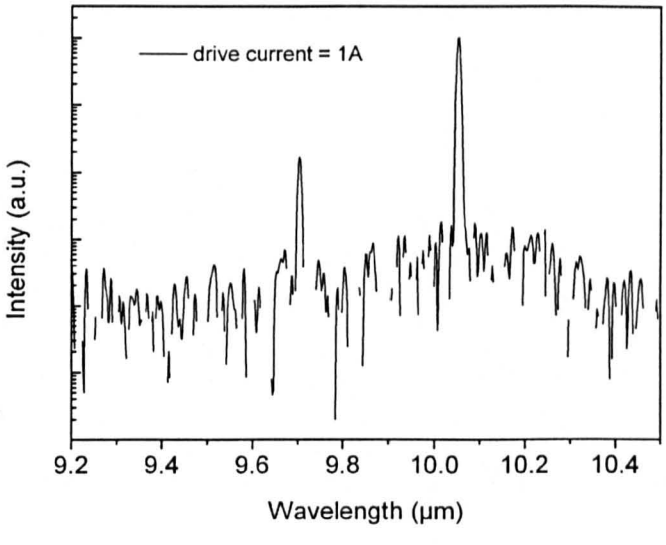

Figure 4.19 *Emission spectrum of a lateral grating DFB laser (ridge width =14μm) plotted on a logarithmic scale. Measurement temperature = 250K. The spectrum shows an additional peak attributed to a higher order transverse mode at a shorter wavelength than the main peak.*

The estimated value for the coupling coefficients based on modelling of the waveguides for devices 9_3 and 14_1 is $\kappa \approx 48$ and 11 cm^{-1}, respectively. The modelled coupling coefficient is based on an assumption that the grating is rectangular. However, in reality the grating is not perfectly rectangular due to the photolithography / etching processes. For a sinusoidal grating shape the coupling coefficient value may be expected to be reduced by a reduction factor, $f_{red} = (\pi/4) \approx 0.79$. It is expected that there would be a significant amount of loss coupling and explains the lack of any additional stop band mode and direct measurement of the coupling strength from the measured spectra.

4.6 Detection of NH_3 using a distributed feedback quantum cascade laser

As mentioned previously in the introduction to this thesis, quantum cascade lasers are of interest to system manufacturers for use in high resolution gas detection. A device similar to that detailed in this chapter was supplied to a commercial company interested in the development of systems utilising single mode QC lasers. In Fig. 4.21 a photographic image of the system along with an image from an oscilloscope screen capture is shown. The screen capture shows three measurement traces. Firstly, a ~150ns electrical pulse (3rd trace) was injected into the device. Over the duration of the electrical pulse, the heating induced in the QCL active region will cause a rapid sweep of the frequency of the emitted light (~ $1 cm^{-1}$). The light is then passed into a test gas cell (containing NH_3) with an etalon increasing the number of passes through the gas sample. As the wavelength of the laser sweeps over the absorption peak of the gas, there will be a dip in the intensity detected, as shown in the second (middle) trace. This equates to a ppm level of sensitivity. This technique successfully demonstrates the suitability of these lateral grating DFB quantum cascade lasers for

use in gas detection applications.

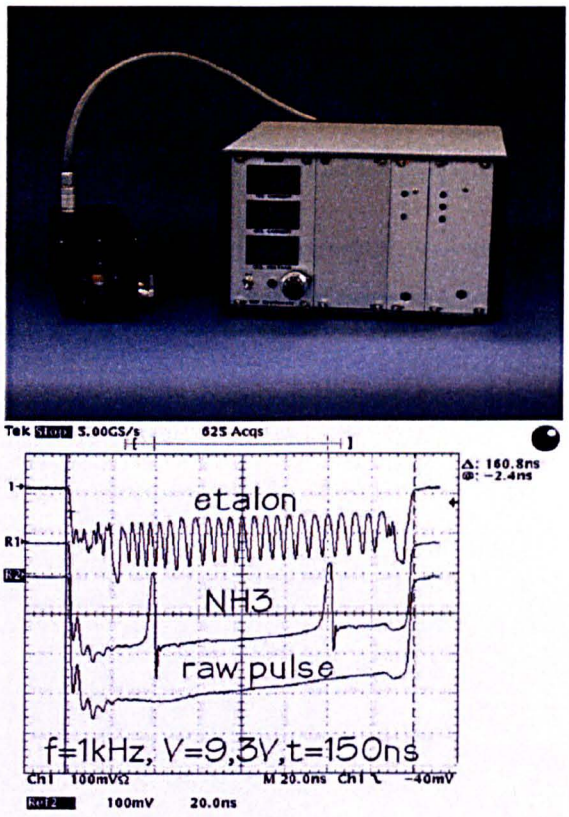

Figure 4.21 *(Upper) Image of a commercial laser based high resolution gas detection system (Lower) Oscilloscope screen capture showing the electrical pulse (~150ns) injected into the lateral grating DFB QC laser (bottom trace). The NH_3 absorption peak (detected in a test gas cell) is shown in the middle trace. (Images courtesy of INP Greifswald e.V)*

4.6 Summary

Through careful attention to the geometrical design of a quantum cascade ridge laser with deep etched lateral gratings, single mode DFB lasers operating above room temperature (λ ~ 10μm) are demonstrated for the first time in the InP material system. The devices have been shown to be suitable for use in sensitive trace gas detection

systems due to their small size, threshold current and good optical output power. A model to calculate the coupling coefficient is shown to be in good agreement with initial experimental results. The use of a lateral grating design significantly simplifies the fabrication process and may enable even more advanced structures and devices to be realised in the future.

4.7 Future work

The realisation of a lateral grating DFB quantum cascade laser will enable further research into more advanced designs. Leaving the top of the ridge planar makes mounting chips upside down easier to facilitate better thermal extraction and better high temperature performance. Deep Bragg Mirrors (DBMs) could be used to increase the reflectivity of the end facets of the lasers and may be etched simultaneously with the ridge and grating. This would increase output powers and help achieve continuous wave operation. Fig. 4.22 shows an example of a DBM DFB laser design attempted on an InP substrate. The optical properties of the dielectric layer on the outside walls of the ridge play an important role in the grating coupling strength and on device performance. Investigating materials other than silicon nitride would be of interest and potential benefit. A broad emission wavelength tuning range is desirable for many spectroscopic applications. An array of lateral grating DFB devices could be used to achieve a wide tuning range by individually or simultaneously altering the grating period, ridge width, injection current, temperature and isolation layer materials.

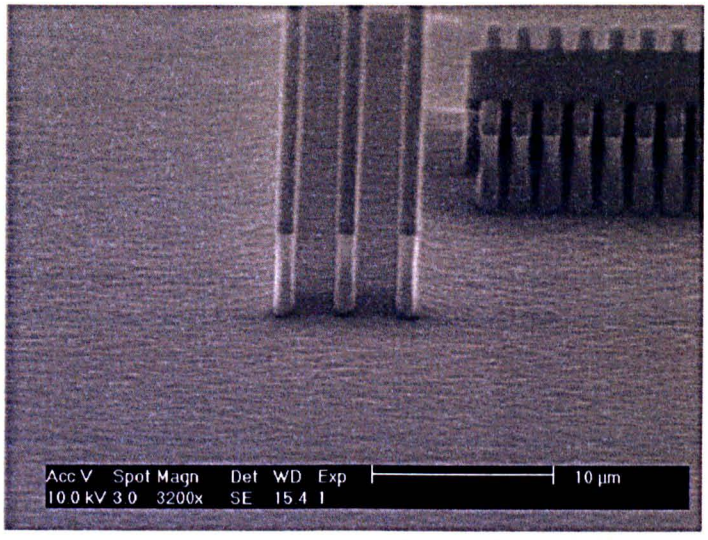

Figure 4.22 *SEM image of a ridge structure with lateral gratings (right) and a Deep Bragg Mirror (centre). Structure was etched into an InP substrate using inductively coupled plasma etching and a SiO_2 mask.*

4.8 References

[1] Faist, J., Gmachl, C., Capasso, F., Sirtori, C., Sivco, D.L., Baillargeon, J. N., Cho, A. Y.: 'Distributed feedback quantum cascade lasers', Appl. Phys. Lett. 1997, 70, 20, pp. 2670-2673.

[2] Hofstetter, D., Faist, J., Beck, M., Muller, A., Oesterle, U.: 'Demonstration of high-performance 10.16μm quantum cascade distributed feedback lasers fabricated without epitaxial regrowth', Appl. Phys. Lett, 1999, 75, 201114

[3] Kohler, R., Gmachl, C., Capasso, F., Tredicucci, A., Sivco, D.L., Cho, A.Y.: 'Single-mode Tunable Quantum Cascade Lasers in the Spectral Range of the CO2 Laser at λ = 9.5-10.5μm', IEEE Phot. Lett. 2000, vol.12, no.5, pp. 474-476

[4] Green, R.P., Wilson, L.R., Zibik, E.A., Revin, D.G., Cockburn, J.W., Pflügl, C., Schrenk, W., Strasser, G., Krysa, A.B., Roberts, J.S., Tey, C.M., Cullis, A.G.: 'High-performance distributed feedback quantum cascade lasers grown by metalorganic vapor phase epitaxy,' Appl. Phys. Lett. 2004, 85, pp. 5529-5531

[5] Darvish, S. R., Slivken, S., Evans, A., Yu, J.S., Razeghi, M.: 'Room-temperature high-power and continuous-wave operation of distributed-feedback quantum-cascade lasers at $\lambda \sim 9.6$ μm', Appl. Phys. Lett. 88, 201114 (2006)

[6] Martin, R.D., Forouhar, S., Keo, S., Lang, R.J., Hunsperger, R.G., Tiberio, R.C., Chapman P.F.: 'An InGaAs-GaAs-AlGaAs Laterally-Coupled Distributed Feedback (LC-DFB) Ridge Laser Diode', IEEE Photon. Technol. Lett. 1995, 7, 244

[7] Kamp. M., Hofmann. J., Schafer, F., Reinhard, M., Fischer, M., Bleuel, T. Reithmaier, J.P., Forchel, A.,: 'Lateral coupling – a material independent way to complex coupled DFB lasers', Optical Materials 2001, 17, pp. 19-25

[8] Golka, S., Pflugl, C., Shrenk, W., Strasser, G.: Quantum cascade lasers with lateral double-sided distributed feedback grating', Appl. Phys. Lett. 2005, 86, 111103

[9] Pendry, J.B., Martín-Moreno, L., Garcia-Vidal, F.J.: 'Mimicking surface plasmons with structured surfaces', Science, 2004, 305, pp. 847 – 848

[10] Barnes, W.L., Dereux, A., Ebbesen, T.W.: 'Surface plasmon subwavelength optics', Nature, 2003, 424, pp. 824-830

[11] Williams, B.S.: 'Terahertz quantum cascade lasers', Nature Photonics, September 2007, vol. 1, pp. 517-525.

[12] B. S. Williams, S. Kumar, Q. Hu and J. L. Reno.: 'Resonant-phonon terahertz quantum-cascade laser operating at 2.1 THz', Electronics Letters, 2004, 40, 7, pp. 431-2.

Chapter 5 - Widely Tunable DFB Quantum Cascade Laser Array Utilising Overgrown Gratings Etched by Inductively Coupled Plasma

5.1 Introduction

This chapter demonstrates a mid-infrared single mode quantum cascade laser source where the emission wavelength is tunable over a broad range. Since the fundamental vibrational modes of most gas molecules occur at mid-infrared wavelengths there is significant interest in QCL's for high resolution gas spectroscopy applications [1]. Typically, gas sensing applications require single mode emission (narrow spectral linewidth) and the ability to tune the emission wavelength in order to detect a particular gas species with high sensitivity. The emission wavelength is swept over the absorption peak of the particular gas species being detected but this absorption peak may be different depending on temperature and pressure of the gas. It is also desirable to have a laser source that could be used to detect multiple gases simultaneously (or on a very short time scale) so that the cost and size of systems can be kept to a minimum. Having several lasers in a system can considerably increase the cost and complexity of the system with a larger number of optics and components being required.

Tuning of a conventional DFB QCL wavelength is achieved by varying the operating temperature (and or drive current). Tuning coefficients of approximately -0.07cm^{-1}/K over the temperature range of 190-330K have been reported [2] and demonstrated in other chapters of this thesis. Broad gain QCLs employed with an external cavity has

enabled single mode emission with a very large tunable range of ~265cm^{-1} [3]. However, external cavity systems are generally considered to be complex and more difficult to manufacture. Alternatively, a wide tuning range has been demonstrated by Lee *at al.*, using a DFB QC laser array where a range of grating periods were defined for each individual DFB laser. The variation in grating period, in conjunction with temperature tuning, allowed continuous single mode operation between 8.7 and 9.4μm [4]. In contrast to the references mentioned above, a widely tunable ($\lambda \sim 9.76 - 10.0$ μm) single mode laser array with ridges of different width but the same grating period is detailed. Wavelength dependence on ridge width is previously demonstrated by Sarangan *at al.* [5] for near infrared interband lasers but is not published at mid-infrared wavelengths. The lasers demonstrated here are important as they are within the 8-13μm atmospheric window and may be used to detect ammonia (NH_3). Furthermore, they could even simplify the manufacturing of array type devices described by Lee *at al.* [4]. Since the first publication in 1997 [6], overgrown gratings in distributed feedback quantum cascade lasers have been demonstrated at several wavelengths [7-9]. Previous publications used various methods of lithography and wet chemical etching to produce the grating, whereas the devices demonstrated in this chapter utilised inductively coupled plasma etching (using only a photoresist mask) with a $SiCl_4$ / Ar gas mixture.

5.2 Design

The indium phosphide based laser material (MR2045) was based on a two-phonon resonance design as described in chapter 1. The 35 active regions were linked together by appropriate bridging regions and both were within an InP waveguide. The 270nm thick InGaAs spacer layer between the top cladding and the laser core region, as

described later, was partially dry etched to provide the grating for the distributed feedback lasers. In references [6-9] the InGaAs layer was generally thicker (~500nm).

An explanation of the general design and methods used for modelling these devices is described in the buried grating section in chapter 2. As a ridge width dependence on emission wavelength is utilised, it is worth noting the reduction in effective refractive index refractive index with decreasing ridge width, as shown in Fig. 2.4. We also see the effective refractive index (Bragg Wavelength) decrease more rapidly as the ridge width gets closer to the wavelength (λ~10μm). This is attributed to the greater overlap of the optical mode with the high loss layers on the outer walls of the ridge. In Fig. 2.11, the grating depth versus coupling coefficient is shown for two ridge widths and shows a linear increase in coupling strength with grating depth. The refractive index difference between the InP and InGaAs materials making up the grating is lower than for a semiconductor / gold grating. However, the intensity of the optical mode is greater for a grating close to the active layer, so strong coupling is still achievable. Furthermore, there is still expected to be some loss coupling present which will reduce the degeneracy of the two modes either side of the stop band.

5.3 Fabry-Perot lasers

Fabry-Perot ridge lasers were fabricated as standard from the material (MR2045) to measure the wavelength of the laser emission peak to check the grating period was suitable for single mode DFB laser operation. In Fig. 5.1, the emission spectrum of a ~20μm wide, 1mm long, quantum cascade laser is shown at the drive current of ~1A. Measurements were taken using a FTIR spectrometer with 0.2cm^{-1} resolution in

pulsed operation (50ns pulse widths, 5kHz repetition rate). The peak wavelength is ~9.9μm and the threshold current density was measured to be ~5.0 kA / cm^{-2}.

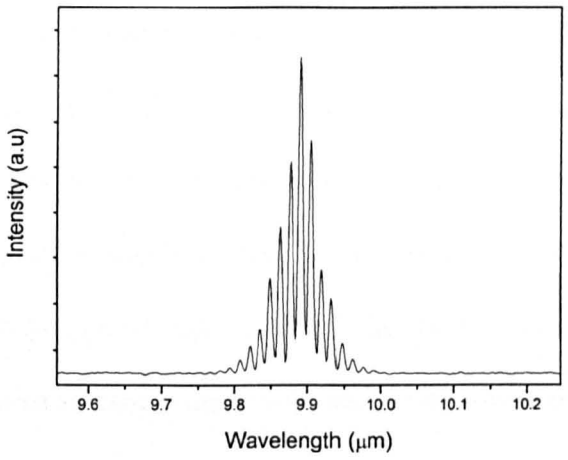

Figure 5.1 Room temperature emission spectrum of a quantum cascade Fabry-Perot laser. Cavity length = 1.0mm. Peak emission wavelength ~ 9.9μm. Measurements taken using a FTIR spectrometer (0.2cm^{-1} resolution). Pulsed electrical operation (50ns pulse width, 5kHz repetition rate).

5.4 Grating fabrication and overgrowth

As mentioned in previous chapters, one of the most time consuming and difficult processes in making a DFB laser is the grating definition. Simplifying this process is desirable to reduce the fabrication time and complexity in manufacturing these devices. Furthermore, device performance and yield can be greatly affected if the process does not produce well defined periodic structures with the correct etch depth and dimensions. A dry etch for surface gratings will typically require a larger etch depth than is required for buried gratings. For overgrown or 'buried' grating designs there is not the same requirement to etch as deep since the grating is closer to the

active region. To enable the process to be simplified, a photoresist mask (Microposit SPR350) was used as a dry etch mask. This eliminated the need to deposit a Plasma Enhanced Chemical Vapour Deposition (PECVD) dielectric mask and to transfer the pattern from photoresist to dielectric using reactive ion etching (RIE). Also, the post semiconductor etch removal of the photoresist mask is trivial. Previous publications demonstrating buried gratings have used wet chemical etches to etch the semiconductor material but wet chemical etching has disadvantages in terms of controlling the depth and size of features. It becomes increasingly difficult to control feature size as the grating period decreases for shorter wavelengths. To meet the etch requirements of smooth surface morphology and controllable etch rate an inductively coupled plasma etch process was developed.

Contact lithography was employed using a Suss MJB3 mask aligner with UV300 optics. A first order grating with period (Λ) = 1.615μm and mark to period ratio ~ 38% was defined in the photoresist. An inductively coupled plasma etch process using $SiCl_4$ / Ar gases was optimized to etch a first order grating into the upper InGaAs layer. The pattern transferred to the semiconductor with the same period, mark : period ratio and a depth of 120nm. The photoresist was removed with solvents and was followed by an oxygen plasma ash to remove any remaining residues. Prior to overgrowth, the sample was cleaned with in a 1:1 sulphuric acid solution (H_2SO_4 : H_2O) for one minute to remove any surface oxide. The sample was quickly rinsed with de-ionised water and stored in a methanol bath before being loaded into a high-vacuum chamber. Re-growth of the InP cladding layer was carried out in a gas-source MBE machine (by Mykhaylo Semtsiv under the direction of Professor Ted Masselink at Humboldt University Berlin) where thermally cracked AsH_3 and PH_3 provided the

group V elements. Solid sources provided the group III elements. Any remaining surface oxide was thermally desorbed under a flux of cracked AsH_3 at a sample temperature of 470°C as measured by an optical pyrometer. The temperature was then decreased to 440°C and InP growth was initiated using an In flux and cracked PH_3. The first few tens of nanometres of InP were grown at a rate of ~0.2 ML/s until a clear and sharp 2x4β surface reconstruction (monitored by RHEED) was recognised, indicating a smooth surface morphology. The growth rate was then increased to 0.85ML/s and 3.8μm of low-doped ($n=1x10^{17}cm^{-3}$) InP:Si was grown, followed by0.9μm of highly doped ($n=7x10^{18}$ cm^{-3}) InP:Si. A bar was cleaved from the overgrown sample in a perpendicular direction to the lines of the grating. In Fig. 5.2 a scanning electron image of the overgrown grating is shown. The grating in the lighter shaded InGaAs layer is clearly visible with a trapezoidal shape.

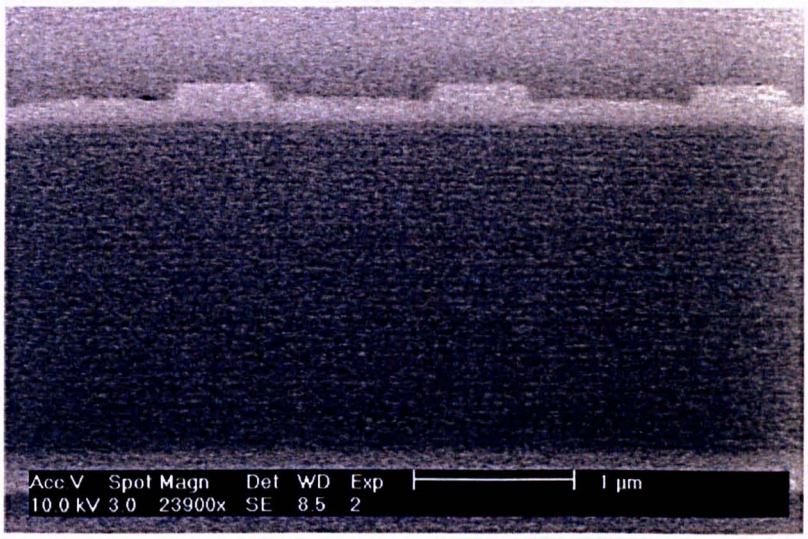

Figure 5.2 Cross sectional SEM (parallel to laser ridge) of an overgrown grating. Grating defined using inductively coupled plasma etching and overgrown using GS MBE. Grating is located in the InGaAs layer directly above the active core region.

5.5 Device fabrication

Laser ridges 10, 20 and 30μm wide were defined by ICP etching (using a SiO_2 mask), allowing excellent control over ridge width and depth. Good vertical sidewalls were achieved using a Chlorine / Argon etch (etch rate ~ 430nm/min) followed by a $SiCl_4$ / Ar etch (etch rate ~ 1μm/min) at chamber pressure = 2mTorr and table temperature of 25°C. The rf powers and ICP powers for the Cl_2 / Ar and $SiCl_4$ / Ar etches were (300W / 500W) and (220W / 1000W) respectively. The sample was not removed from the ICP chamber between etches and a 5 minute pump down was used between the two etch recipes to evacuate the chamber. After removal of the SiO_2 mask using HF acid, a silicon nitride isolation layer (~ 400nm thick) was deposited by plasma enhanced chemical vapour deposition. Dielectric was etched from the top of the ridge using reactive ion etching and CHF_3 / O_2 etch gases. Top metal contacts of Titanium and Gold were thermally evaporated onto the sample and annealed in a rapid thermal annealing system at a temperature of 340°C. The sample substrate was thinned down to ~150μm to help with the thermal extraction and cleaving processes. Finally, 0.5, 1.0 and 1.5mm bars were cleaved from the sample. The devices were then mounted ridge side up using indium solder and gold wire bonded.

5.6 Laser characterisation

The optical characteristics of the lasers were measured using a Fourier transform infra-red spectrometer with a resolution of $0.2cm^{-1}$. The lasers were driven by 50ns electrical pulses with a repetition rate of 5 kHz. The 0.5mm cavity length devices showed 'single-mode like' emission but had poor side mode suppression ratios and typically operated in more than one mode. This was expected since κL was calculated

to be less than 1. The 1mm and 1.5mm cavity length devices both showed good single mode operation with side mode suppression ratios ≥25 dB at room temperature The room temperature emission spectra for 1.5mm long DFB lasers with the same grating period but different ridge width are shown in Fig. 5.3. The emission wavelength can be observed to shift non-linearly to a shorter wavelength with decreasing ridge width. Furthermore, this shift is very significant (~10cm^{-1}, ~ 100nm).

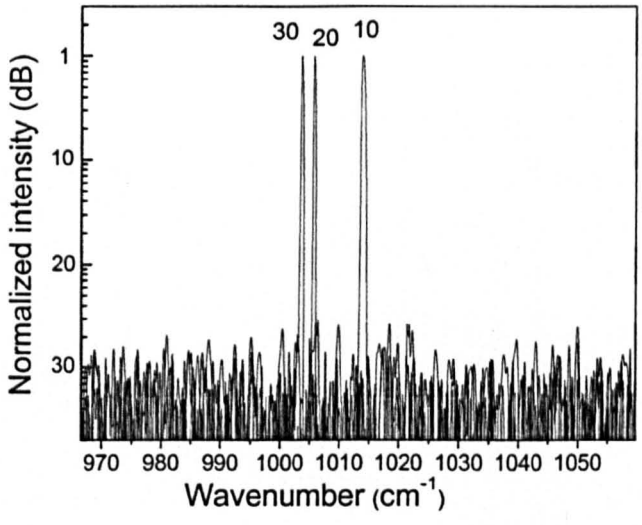

Figure 5.3 Room temperature emission spectra of DFB quantum cascade lasers with the same grating period but different ridge width. Ridge widths (μm) are shown above the emission peaks. Cavity length = 1.5mm.

Considering the waveguide modelling and the graph in Fig. 2.4, the measured wavelength shift is larger than the predicted shift by about a factor of two. In Fig. 5.4 the current-voltage curves for 10, 20 and 30μm wide ridges are plotted. At liquid nitrogen temperatures the curves are similar for the three ridge widths but a higher resistance is observed for narrower ridges. At room temperature there is a distinct

difference in the I-V characteristics and a greater difference in resistance for each ridge width. This allows a simple check of each device using a multimeter probe giving a rough guide to ridge width, without the need for optical or electron microscopes.

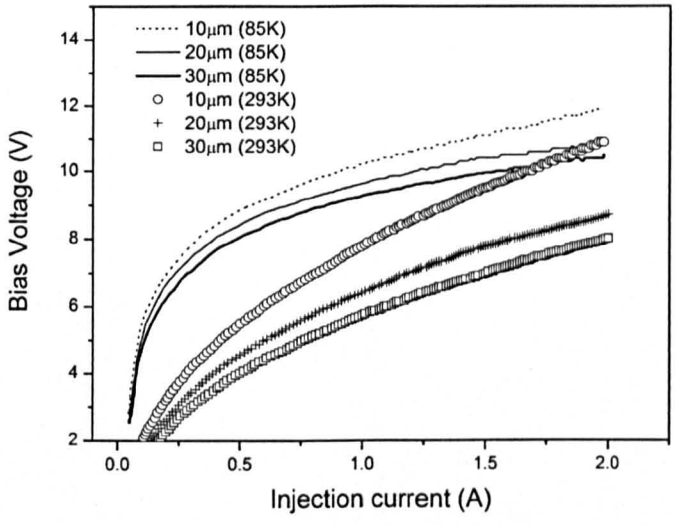

Figure 5.4 I-V curves at the temperatures of 85K and 293K for DFB quantum cascade lasers with ridge widths of 10, 20 and 30μm.

The room temperature pulsed light-current characteristics of the three ridges with different widths are plotted in Fig 5.5. Even though the facets were left uncoated and the cavity lengths are relatively short (L=1mm), peak output powers of tens of milliwatts were measured at room temperature and lasers still operated above room temperature. Laser modes confined within the narrower ridges will experience a greater loss due to the larger overlap of the optical mode with the dielectric and gold layers on the outside walls of the ridges. This loss will cause a modification of the effective refractive index and decrease the Bragg wavelength. The measured effective refractive index values ($n_{eff} = \lambda / 2 \, . \, \Lambda$) obtained from the spectral lines for the 10, 20

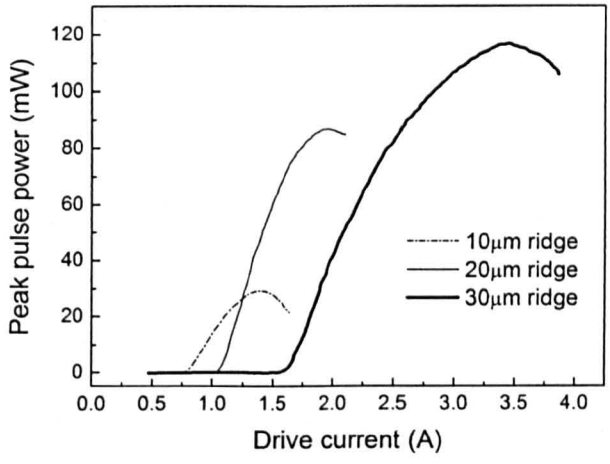

Figure 5.5 Peak output power versus drive current at room temperature for DFB quantum cascade lasers with different ridge widths but same grating period. Cavity length = 1mm

and 30μm ridge widths are ~ 3.05, 3.07, 3.08 respectively. The coupling coefficient was once again able to be measured directly from the spectrum of one of the devices measured. A 10μm ridge DFB laser was observed to have two modes, assumed to be either side of the stop band. The spectrum is shown in Fig. 5.6. The stop band width is measured be ~1cm^{-1} which gives an approximate value for the coupling coefficient of $\kappa \approx 10.8$ cm^{-1}. The calculated values for the coupling coefficients for the 10, 20 and 30μm ridges are (12.8 + 1.2i) cm^{-1}, (11.7 + 0.1i) cm^{-1} and (11.4 + 0.03i) cm^{-1} respectively. Calculations are based on the method described in section 2.7.

The calculated values are for a square grating shape and 50% mark to period ratio. Therefore, a slightly lower measured value is to be expected for the lower mark to period ratio measured for these devices. The reduction factor for this device is experimentally found to be ~0.83. This value is between the reduction value, f_{red} = sin

($\pi\Lambda_1/\Lambda$) expected for a sinusoidal shaped grating (~0.79) and a rectangular shaped grating with 38% mark to period ratio (~0.93).

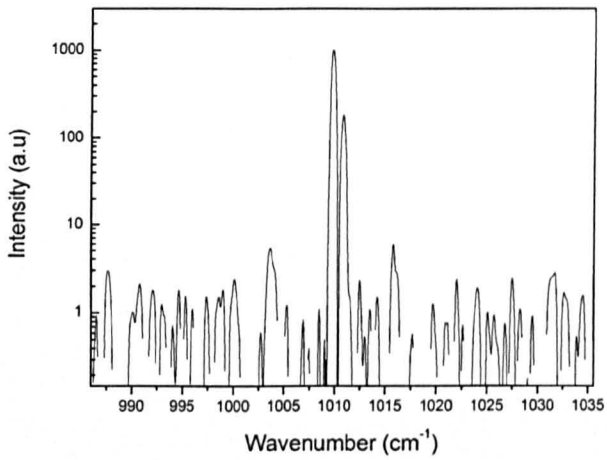

Figure 5.6 Emission spectrum of a 10μm wide 'buried' grating DFB laser plotted on a logarithmic scale. Spectrum shows two nodes which are assumed to be either side of the stop band, allowing the direct measurement of the coupling coefficient.

The slight discrepancy could be due to the trapezoidal shape of the grating, but the experimental and calculated values are in good agreement. From the calculated coupling coefficients and single mode laser spectra it is evident there is some loss coupling present, helping to reduce the degeneracy of the two modes either side of the stop band. The high single mode yield (~75%) for all ridge widths tested (L = 1mm and 1.5mm) is evidence of a good match between material laser gain peak and grating period. However, there was no obvious reduction in threshold current density which suggests the grating does incorporate a significant loss into the waveguide structure. The reduction in the optical mode confinement by etching the InGaAs layer (directly

above the active region) introduces losses, but is an effective method for producing single mode devices with high spectral selectivity.

Figure 5.7 shows the emission spectra of two single mode lasers of ridge widths 10 and 20μm for different heat-sink temperatures. Side mode suppression ratios (SMSR) were measured to be ≥ 25dB for all drive currents. The temperature was varied over a range where the emission was still observed to be single mode. Below 140K, multimode behaviour is observed since the gain peak of the material and Bragg wavelength of the grating are not suitably overlapping. The 20μm ridge was still operating in a single mode at 380K, but the 10μm ridge was only tested up to 300K because its emission wavelength already matched that of the 20μm ridge at 140K. The converging wavelengths of the two lasers enabled a combined continuous wavelength tuning range of ~ 235nm (~ 24cm^{-1}) with a tuning coefficient of –0.1 cm^{-1} K^{-1}.

In Fig. 5.8 the threshold current density for the two laser ridge widths is plotted against operating temperature for pulsed electrical operation. Measurements were detected using a liquid nitrogen cooled HgCdTe detector. The plot shows the higher current density requirement for lasing of the narrower ridge, due to the greater waveguide losses.

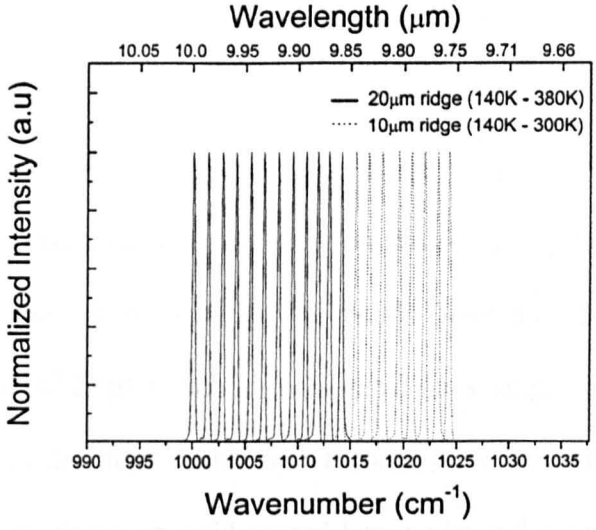

Figure 5.7 Single mode emission spectra of two DFB lasers with 10μm and 20μm wide ridges. The spectra show the temperature wavelength tuning for both ridges. The two laser ridges demonstrate a broad, combined, continuous tuning range.

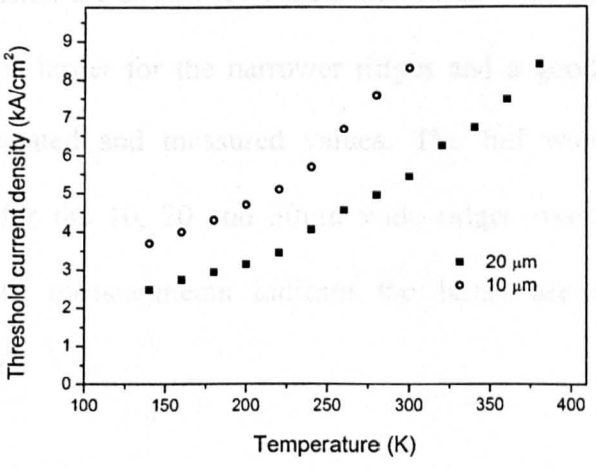

Figure 5.8 Threshold current density versus operating temperature for DFB lasers with ridge widths of 10 and 20μm. Measurements are for pulsed electrical operation (50ns pulse widths, 5kHz repetition rate).

5.7 Far-field measurements

Far-field measurements of the DFB laser ridges were performed to investigate the angular intensity distribution in the lateral direction. The far-field measurements would confirm the lasers were operating in the fundamental longitudinal transverse mode and show the effect of the ridge width on the angular spread of the emitted light. The far-field in the lateral direction depends strongly on the lateral guiding mechanism (index guiding) which should result in a single peak with the angular spread increasing as the ridge width decreases. A laser bar with devices of different ridge widths were mounted on gold coated heat-sinks and operated with 100ns wide pulses and a 5kHz repetition rate. The room temperature intensity was measured using a liquid nitrogen cooled HgCdTe detector placed a distance (10cm) away from the front facet of the laser bar. The detector was situated on an arm, fixed at one end to a rotation stage. This allowed the angle to be measured as the detector was swept through the emitted output of the laser. In Fig. 5.9 the measured and calculated far-field intensity patterns are shown for 10, 20 and 30μm wide ridges. As expected the beam divergence is larger for the narrower ridges and a good agreement is shown between the calculated and measured values. The full width at half maximum (FWHM) values for the 10, 20 and 30μm wide ridges were ~ 46°, 31° and 22° respectively. These measurements indicate the lasers are all operating in the fundamental mode.

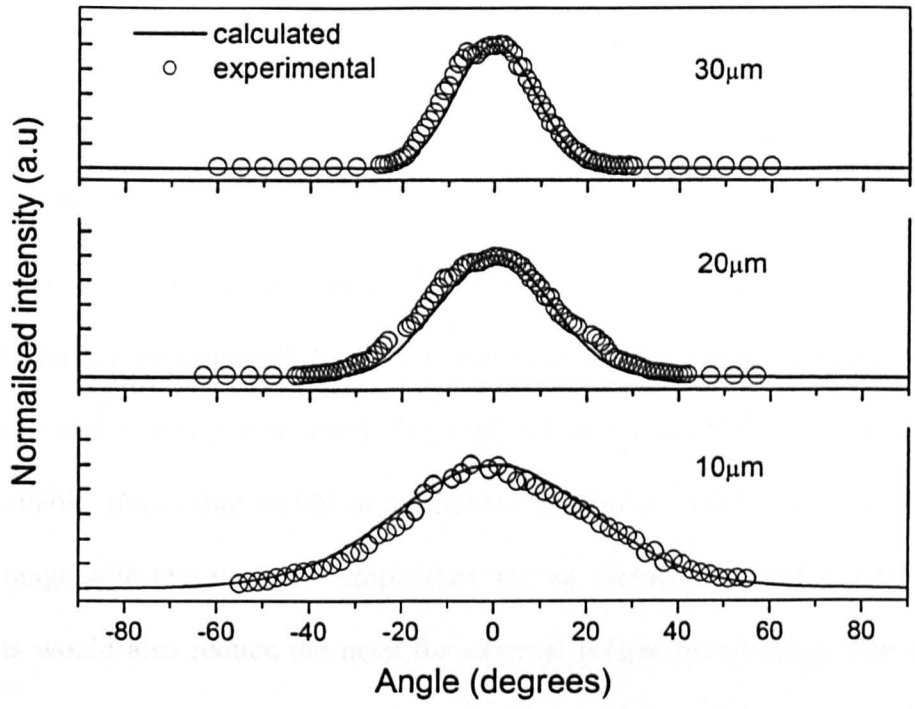

Figure 5.9 Far-field intensity measurements for 10, 20 and 30 μm wide quantum cascade DFB laser ridges. Measurements are taken in lateral direction. Calculated (solid line) and measured (circles) values are in good agreement.

5.8 Summary

This chapter demonstrates mid-infrared, high power, single mode lasers in an array with side mode suppression ratios greater than 25dB over a wide temperature range. A buried grating design was etched by using an inductively coupled plasma etch process using a $SiCl_4$ / Ar chemistry and overgrown by GSMBE. A large tunable emission wavelength range in excess of 230nm was achieved utilising a temperature and ridge width dependence on emission wavelength. The combined tuning coefficient was measured to be -0.1 / cm / K. The lasers emitting close to $\lambda = 10\mu m$ are suitable for gas sensing applications and may simplify manufacturing of such DFB lasers since

only a single grating period is used. This enables holographic interference lithography to be used more effectively.

5.9 Future work

The demonstration of a significant shift in emission wavelength with ridge width could be further investigated to increase the tuning range and investigate the larger shift measured than was calculated. The high single mode yield for all ridge widths should enable more ridge widths to be defined in close proximity to produce a large tuning range with less need for temperature tuning. Development of on-chip heating elements would also reduce the need for external temperature tuning. The effect of lowering the waveguide losses by increasing the facet reflectivity could be investigated to observe any additional change in wavelength. Varying the facet reflectivity combined with variable ridge widths may further increase the tuning range.

5.10 References

[1] Normand, E., Duxbury, G., Langford, N.: Characterisation of the spectral behaviour of pulsed quantum cascade lasers using a high resolution Fourier transform infrared spectrometer', Optics Comm., 2001, 197, pp. 115-120

[2] Green, R.P., Wilson, L.R., Zibik, E.A., Revin, D.G., Cockburn, J.W., Pflügl, C., Schrenk, W., Strasser, G., Krysa, A.B., Roberts, J.S., Tey, C.M., Cullis, A.G.: 'High-performance distributed feedback quantum cascade lasers grown by metalorganic vapor phase epitaxy,' Appl. Phys. Lett. 2004, 85, pp. 5529-5531

[3] Maulini, R., Mohan, A., Giovannini, M., Faist, J., Gini, E. : 'External cavity quantum-cascade laser tunable form 8.2 to 10.4μm using a gain element with a heterogeneous cascade', Appl. Phys. Lett. 2006, 88, 201113

[4] Lee, B.G., Belkin, M.A., Audet, R., MacArthur, J., Diehl, L., Pflügl, C., Capasso, F., Oakley, D.C., Chapman, D., Napoleone, A., Bour, D., Corzine, S., Hofler, G.: 'Widely tunable single-mode quantum cascade laser source for mid-infrared spectroscopy', Appl. Phys. Lett. 2007, 91, 231101

[5] Sarangan, A.M., Huang, W.P., Makino, T., Li, G.P.: 'Dynamic Single-Transverse-Mode Properties of Varying Ridge Width DFB laser Arrays', IEEE PTL, 1996, vol. 8, no. 10, pp. 1305-1307

[6] Gmachl, C., Faist, J., D.L., Baillargeon, Capasso, F., Sirtori, C., Sivco, J. N., Chu, S. N. G., Cho, A. Y.: 'Complex-coupled distributed feedback quantum cascade laser', IEEE Phot. Tech. Lett. 1997, 10, 8, pp. 1090-1092

[7] Blaser, S., Yarekha, D. A., Hvozdara, L., Bonetti, Y., Muller, A., Giovannini, M., Faist, J.: 'Room-temperaure, continous-wave, single-mode quantum-cascade lasers at λ~5.4μm', Appl. Phys. Lett, 2005, 86, 041109

[8] Yu, J. S., Slivken, S., Darvish, S.R., Evans, A., Golkden, B., Razeghi, M 'High-power, room-temperaure, and continous-wave operation of distributed-feedback quantum-cascade lasers at λ~4.8μm', Appl. Phys. Lett, 2005, 87, 041104

[9] Darvish, S.R., Slivken, S., Evans, A., Yu, J.S., Razeghi, M.: 'Room-temperaure, high-power, and continous-wave operation of distributed feedback quantum-cascade lasers at λ~9.6μm', Appl. Phys. Lett, 2006, 88, 201114

Chapter 6 - Narrow Ridge Quantum Cascade Laser ($\lambda \approx 3.9\mu m$) with Symmetric Far-Field Profile and Improved Thermal Conductance

6.1 Introduction

Typically, edge emitting semiconductor lasers produce a beam of light with an elliptical cross section. This is due to the different sizes of the optical cavity along the fast axis (perpendicular to the epitaxial layers) and slow axis (parallel to the epitaxial layers). In addition to the spectral and electrical requirements of mid-infrared laser based applications, the laser beam profile and divergence [1-2] can have an important impact on the optical design of a system. In some imaging and spectroscopic applications [3-6] the elliptical cross section beam profile is shaped (towards being circular) through the use of cylindrical optics which increases the complexity and cost of the optical set-up. The beam quality factor or beam propagation factor (M^2) is the standard measure where, $M^2 = 1$ corresponds to a 'perfect' Gaussian beam profile and is often referred to as diffraction limited (can be focussed to the smallest diffraction limited spot size). All real beams have an M^2 value greater than 1 with the beam quality factor of a laser beam limiting the degree to which the beam can be focused.

In this chapter quantum cascade lasers ($\lambda \approx 3.9$ μm) emitting in the technologically important, 'absorption window' region of the mid-infrared are described. Even with narrow ridges the peak output powers are suitably high without using a buried heterostructure design, where the active region is surrounded by insulating InP (doped with Fe), grown by further epitaxy processes [7-8]. The lasers emit in a single TM_{00}

spatial mode with a beam divergence that is equal in both the vertical and lateral directions. The ridge widths demonstrated here are narrower, with a beam quality factor that is closer to unity than reported for wider QCL ridge waveguides [9]. Due to the large number of active and injector regions within a QCL, there is more flexibility in determining the optical cavity sizes [10, 11]. Therefore, details reported in this chapter will aid future waveguide design so that the beam quality may be optimised even if the output power requirements are increased. The narrow ridge design was modelled and a new mask set designed to achieve a 2-stage, thick electroplated gold layer for good thermal management. The narrow ridge was achieved by inductively coupled plasma etching with smooth morphology and is shown to be comparable, in terms of thermal conductivity, to 'buried' (overgrown) ridge designs. The greater thermal extraction demonstrated by the narrow ridge laser allows continuous wave (CW) operation at low temperature and high-duty-cycle operation on thermoelectric cooler. Therefore, these QC lasers are suitable for many mid-infrared applications as well as being suitable for further development into single mode distributed feedback lasers for high resolution detection of gases such as HBr.

6.2 Sample design and fabrication

The laser structure (sample HU1596) was grown using gas-source molecular-beam epitaxy (GSMBE) on a low-doped ($n = 2 \times 10^{17}$ cm^{-3}) InP : Sn substrate. The substrate also serves as the lower cladding layer. The epitaxy layer sequence consisted of 247 nm $In_{0.52}Ga_{0.48}As$: Si ($n = 5 \times 10^{16}$cm^{-3}), then the 1.447 μm (total thickness) 30-stage active region, 231 nm $In_{0.52}Ga_{0.48}As$: Si ($n = 5 \times 10^{16}$ cm^{-3}), then 18 nm $In_{0.52}Ga_{0.48}As$: Si-$In_{0.52}Al_{0.48}As$: Si four-period graded superlattice, then a 2.5 μm ($n = 1 \times 10^{17}$ cm^{-3}) InP : Si plus 0.8 μm ($n = 4 \times 10^{18}$ cm^{-3}) InP : Si top cladding layer, and finally a 120

nm $In_{0.52}Ga_{0.48}As$: Si (n = 1 x 10^{19} cm^{-3}) top contact layer. The strain-compensated bound-to-continuum active region design is similar to that described in reference 12. The active region layer thicknesses (in nanometres) starting from the injection barrier are

3.0/**0.9**/1.8/**0.9**/5.0/**1.7**/4.2/**2.1**/3.8/**1.5**/3.4/**1.3**/3.0/**1.1**/2.6/**0.9**/2.2/*1.4*/**0.9**/2.0/*1.4*/**0.9**/1.8. The AlAs layers are in bold, $In_{0.73}Ga_{0.27}As$ in roman and $In_{0.55}Al_{0.45}As$ in italic.

In Fig. 6.1 the refractive index and calculated optical mode intensity profiles (vertical direction) are plotted for a quantum cascade ridge laser structure ($\lambda \sim 3.9$ μm) as previously described. The structure takes an average refractive index value for the active core region but the cladding layers are specified individually.

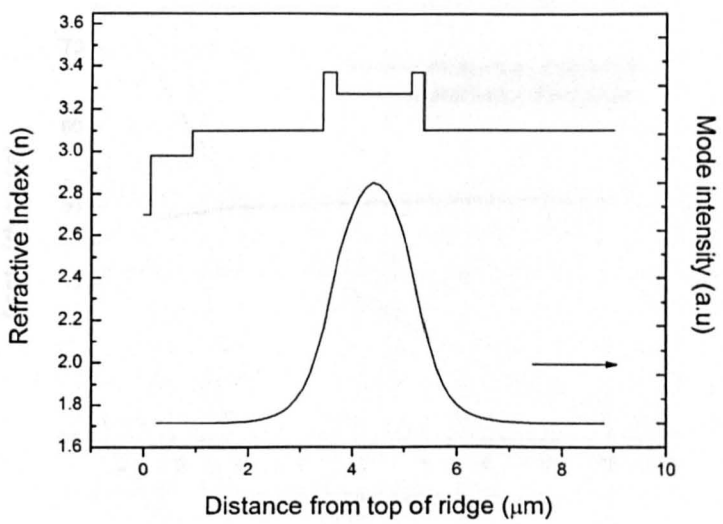

Figure 6.1 Refractive index and optical mode intensity profiles for the fundamental TM mode in the vertical direction (perpendicular to epitaxial layers) of a quantum cascade ridge laser ($\lambda \approx 3.9$ μm). Ridge width = 5 μm.

For high duty cycle or continuous-wave operation, good thermal management is required. This is critical for QC lasers due to their relatively high threshold current densities. A good choice of materials (such as electroplated gold) covering the laser ridge allows greater extraction of heat from the sidewalls of the ridge [13]. Mounting lasers with the epitaxial side down (in contact with heat-sink) can also improve the thermal extraction but can be less desirable from a manufacturing point of view. Narrow ridges increase the thermal conductance per unit area away from the active region because of an increased contribution of the heat flow through the sidewalls relative to the vertical heat flow [14]. Therefore, when considering the design of these lasers, a narrow ridge is desirable but a compromise has to be found between the increased losses incurred by narrower ridges (lower output power / high threshold current density) and any advantages (good thermal management and beam quality).

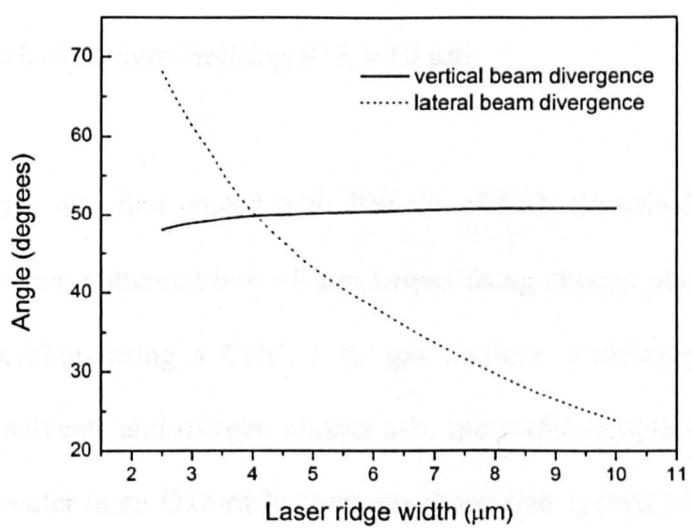

Figure 6.2 Plot of the calculated beam divergence against the laser ridge width for a quantum cascade laser ($\lambda \approx 3.9\ \mu m$). Lateral (parallel to epitaxial layers) and vertical (perpendicular to epitaxial layers) directions are shown. Full divergence angle is plotted using the FWHM values.

In Fig. 6.2 the calculated beam divergence is plotted against the ridge width using a waveguide modelling software [15]. The laser beam divergence is plotted for both the vertical and horizontal directions. A full width at half maximum (FWHM) value is used to determine the full beam divergence angle. From the graph shown in Fig. 6.2 it is apparent that a symmetric far-field profile can be achieved with a laser ridge width between 4 and 5μm. Both the vertical and the lateral beam divergence are slightly less than 50°. The lateral beam divergence is clearly more dependent on ridge width than the vertical divergence which is essentially set by the grown layer thicknesses of the active region. An important parameter is the refractive index of the silicon nitride used as an insulating layer on the outer walls of the ridge. At a wavelength of 3.9 μm the refractive index is taken to be 1.95 [16]. The absorption coefficient at this wavelength is low, especially compared to $\lambda \approx 10$ μm, as used in other chapters in this thesis. The low absorption enables narrower ridge lasers as waveguide losses do not increase as much as devices emitting at $\lambda \approx 10$ μm.

The laser sample was first coated with 800 nm of SiO_2 deposited by PECVD. The SiO_2 layer was then patterned into ~5 μm stripes using contact photolithography and reactive ion etching, using a CHF_3 / Ar gas mixture. Following stripping of the photoresist in solvents and oxygen plasma ash, the wafer sample was loaded onto a silicon carrier wafer in an Oxford Instruments Plasmalab system 100 ICP etcher. The table temperature was set at 25 °C and the pressure was set to 2 mTorr. The flow rates for the $SiCl_4$ and Ar gases were 8 sccm and 35 sccm respectively. The semiconductor etch process enabled a narrow ridge width to be etched controllably (using a laser end-point detection system) while still keeping the ridge width close to the intended linewidth without undercutting of the mask. This was important for aligning the

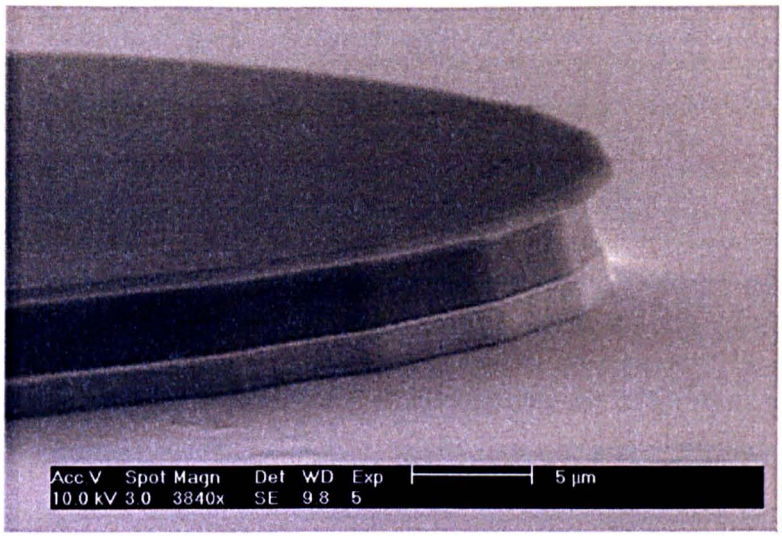

Figure 6.3 Scanning electron microscope image of a circular mesa structure etched into quantum cascade laser material. Lighter shaded material at bottom of material is active region. Material was etched by ICP etching and a SiO_2 mask. Process parameters were: $SiCl_4$ / Ar gas flows (8 / 35) sccm, RF / ICP power (220 / 1000)W, Pressure = 2 mTorr, no helium cooling. Table temperature set to 25 °C

contact window to the top of the ridge. A good smooth surface morphology and slightly sloped sidewall were produced. The final ridge width and depth were measured by scanning electron microscope to be ~4.6 μm and ~5.5 μm respectively. After removal of the SiO_2 mask in HF acid a 300 nm thick PECVD silicon nitride layer was deposited onto the sample. Titanium and Gold (20 / 200 nm) electrical contacts were thermally evaporated onto the sample after a 2 μm window was etched into the silicon nitride layer on top of the ridge using reactive ion etching. Thick electroplated gold was deposited in two stages to form good heat-sinking around the ridge. Approximately 3 μm of gold was electroplated over the whole ridge and then another 2 μm of gold was deposited on the ridges, leaving gaps at the facets to aid the

cleaving process. Finally, the sample was thinned down to ~100 μm thick, and Ti / Au contacts (20 / 200 nm) were evaporated on to the back of the sample. Lasers were cleaved from the sample (length = 3 mm) and indium soldered to copper submounts with the epitaxial layers up and were tested with the cleaved facets left uncoated. In Fig. 6.3 a circular mesa etched with the same process as described above is shown. The smooth surface morphology and sidewall etching is visible in the SEM image. There is also some undercutting of the mask due to the chemical nature of the etch, slightly reducing the sidewall verticality. In Fig. 6.4, a SEM image of a fully processed quantum cascade laser is shown. The thick electroplated gold is clearly visible surrounding the ridge.

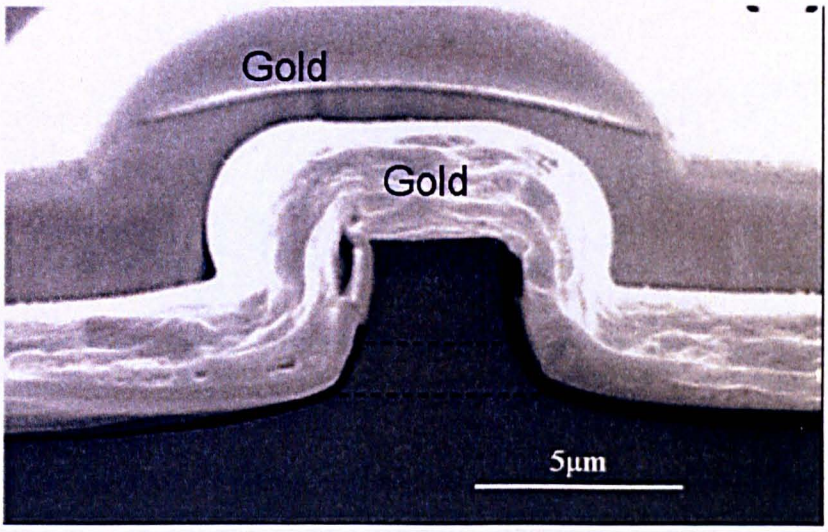

Fig.ure 6.4 Scanning electron microscope image of a narrow ridge quantum cascade laser (λ ≈ 3.9 μm) with thick gold electroplating. The active core region is contained within the area outlined by dashed lines. Dark layer directly under the gold is PECVD silicon nitride.

6.3 Laser characterisation

Far-field measurements of the lasers were carried out at room temperature. Two methods were used to measure the laser emission. Firstly, a fixed single pixel detector was used in combination with a rotation stage. Secondly, infrared imaging using a 384 x 288 pixel, HgCdTe detector array based camera (Thermosensorik CMT 384M) operating in the 2.0 μm – 6.0 μm range was used. The spectral range of the camera was restricted to 3.4 μm – 6.0 μm by using an optical filter and by measuring differential images to minimise the impact of ambient thermal emission on the far-field image. Figure 6.5 shows an image of the laser far-field intensity in logarithmic scale, where the camera was focused close to the facet of the laser. The image demonstrates the circular cross-section of the single TM_{00} mode beam.

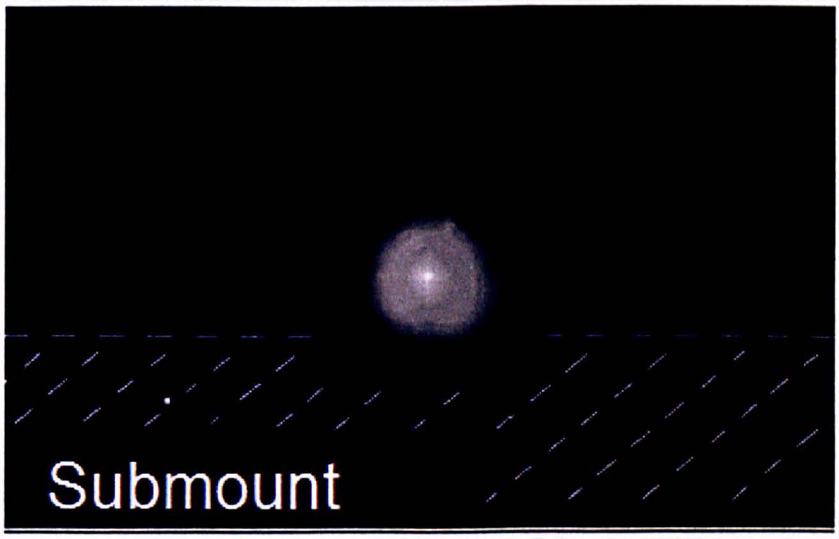

Figure 6.5 Measured two-dimensional beam profile of a narrow ridge quantum cascade laser (λ ≈ 3.9 μm) showing a single TM_{00} mode. Image is recorded using a Thermosensorik (CMT 384M) HgCdTe detector array based infrared camera. Measurements were taken at room temperature. Reproduced from[20].

The copper submount, that the laser is situated on shadows a bottom portion of the laser beam. Also, some low intensity diffuse light is detected around the laser beam which is the reflected emission from the rear facet. The beam divergence in the vertical (fast axis) and lateral (slow axis) directions were measured with the laser mounted on a translation stage and using the single pixel detector. The beam divergence in both directions was measured to be 46° (FWHM) implying a circular beam profile as shown in Fig. 6.6.

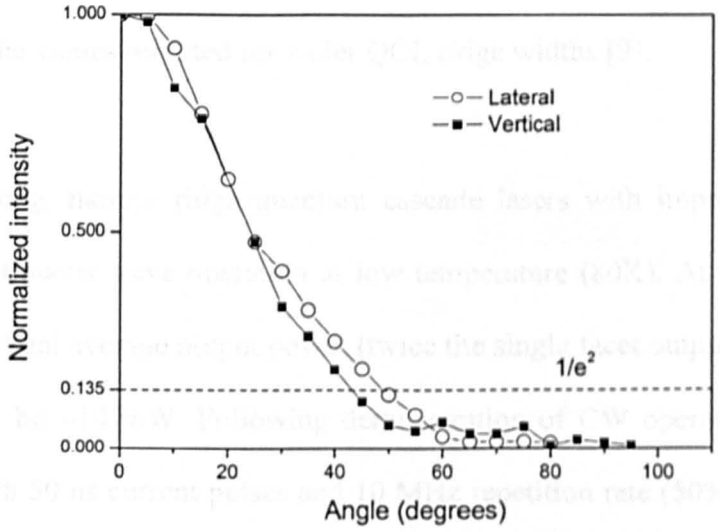

Figure 6.6 Measured laser beam divergence of a narrow ridge quantum cascade laser (λ ≈ 3.9 μm) in the lateral (slow axis) and vertical (fast axis) directions. Measurements were taken at room temperature in pulsed operation. The $1/e^2$ intensity level is indicated with a dashed line. Full width at half maximum (FWHM) value for both directions is 46°.

Calculations based on the effective beam waist size radius (ω) in the vertical direction (using $1/e^2$ values) found the beam to be essentially diffraction limited along the fast axis. The beam quality factor [17-18] is given by,

$$M^2 = \frac{\theta \pi^2 \omega}{360 \lambda}$$

where θ is the full beam divergence angle (degrees) at $1/e^2$ values and λ is the wavelength. Along the slow axis, the beam waist size is taken to be equal to the facet size. The beam quality factor is calculated to be $M^2 \approx 1.6$. These beam parameters are better than the values reported for wider QCL ridge widths [9].

The 3mm long, narrow ridge quantum cascade lasers with improved heat-sinking allowed continuous wave operation at low temperature (80K). At a drive current of 430 mA the total average output power (twice the single facet output) of the laser was measured to be ~10 mW. Following demonstration of CW operation the laser was operated with 50 ns current pulses and 10 MHz repetition rate (50% duty cycle). The total average output power was measured to be 200 mW at a drive current of 870mA. A slope efficiency of 0.42 W/A was measured to be almost constant in the current range between 400 and 870 mA.

The laser performance at room temperature and thermoelectric cooler temperature is even more important when integrating the devices into portable systems for spectroscopic and imaging applications. The room temperature laser emission is centred at approximately 3.9 μm as shown in the Fourier transform spectrum inset in Fig. 6.7. The total average output power for a 3 mm long laser mounted on a double-

stage thermoelectric cooler was measured as function of duty cycle and temperature and plotted in the same figure. The maximum average power at 730 mA was measured to be 5 mW and 63 mW at the temperatures of 20 °C and -52 °C, respectively. The maximum (low duty cycle) peak optical power (averaged over the pulse length) at 730 mA was measured to be 86 mW and 460mW at 20 °C and -52 °C, respectively.

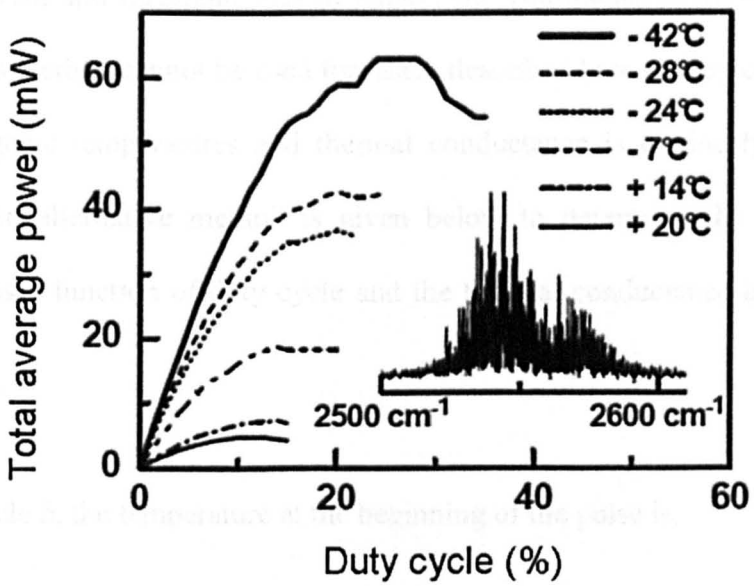

Figure 6.7 Total average emission power as a function of duty cycle for different heat-sink temperatures. Measurements are for a 3 mm long, narrow ridge QCL with uncoated facets. Drive current = 730 mA, current pulse length = 50 ns. The inset shows a room temperature, high-resolution (0.2 cm^{-1}) Fourier-transform spectrum of the laser (drive current = 760 mA, current pulse length =10 ns.Reproduced from[20]

The average laser emission power versus duty cycle curves at different temperatures can be used to determine the total thermal resistance R_{th} of the laser. The thermal conductance per unit area is $G_{th} = 1 / A R_{th}$, where A is the device area. At a duty

cycle of approximately 25%, the average output power reaches a maximum before reducing. This effect is due to the increased temperature in the active region during the pulse which is dependent on duty cycle. For very low duty cycles the active region temperature at the beginning of the pulse is the same as the heat-sink temperature. However, for higher duty cycles the active region temperature does not return to the heat-sink temperature before the next pulse starts. A commonly accepted method to determine the thermal conductance of a QCL ridge *is based on a comparison of* threshold current and threshold bias in pulsed and continuous wave operation [19]. However, this method cannot be used for lasers described here as they only operate in CW at cryogenic temperatures and thermal conductance is obviously temperature dependent. An alternative method is given below to determine the active region temperature as a function of duty cycle and the thermal conductance is gained from this. [20]

For a duty cycle δ, the temperature at the beginning of the pulse is,

$$T_0 \approx T_c + P_{\text{drive}} R_{\text{th}} \delta,$$

where, T_h is the heat-sink temperature and P_{drive} is the input power. During the pulse, the emitted power also decreases due to the active region heating. This heating also takes place for a very low duty cycle. The average emission power during the pulse P^*_{out} is approximately the mid-pulse power at time $t = t_p / 2$. The active region temperature is given by,

$$T_a = T_c + [P_{\text{drive}} t_p / 2 C_{\text{th}}] + P_{\text{drive}} R_{\text{th}} \delta$$

where, C_{th} is the thermal capacity of the active region. The rise in temperature during half the pulse is given by, $P_{drive}\, t_p / 2\, C_{th} \approx 5$ K. The average emission power during the pulse is a function of T_a only, with T_a as a function of T_c and δ (constant P_{drive}). It then follows that, $P^*_{out}(T_a) = P^*_{out}(\delta, T_h) = P^*_{out}(\delta = 0, T_h) + [(dP^*_{out} / dT)\, P_{drive} R_{th} \delta]$. Thus, when $P^*_{out}(\delta, T_{h1}) = P^*_{out}(\delta = 0, T_{h2})$, then $T_a(\delta, T_{h1}) = T_a(\delta = 0, T_{h2})$. As long as C_{th} is independent of temperature, the data gives the increase in the active region temperature as a function of duty cycle and so, $T_0(\delta, T_{h1}) = T_{h2}$. The increased temperature due to the nonzero duty cycle is then,

$$\Delta T_a = T_{h2} - T_{h1} \approx P_{drive} R_{th} \delta .$$

Figure 6.8 plots the temperature increase of the active region as a function of duty cycle. The thermal conductance is then approximately the ratio of average dissipated power to ΔT. The pulse power used was 8.7 W, which indicated an absolute thermal conductance of 0.056 W/K or an absolute thermal resistance of R_{th} = 18 K/W. Even though the thermal conductance per unit area increases for narrow ridges, the absolute thermal resistance can be high due to the small area. Since the threshold power scales with the area of the laser, the most appropriate figure to use is the thermal conductance per unit area. Therefore, the corresponding thermal conductance per area is calculated to be 380 $WK^{-1}cm^{-2}$. This value fits well into the general trend of similar quantum cascade lasers with different ridge widths where thermal conductance per unit area increases with decreasing ridge width. Reported values include, 225 $WK^{-1}cm^{-2}$ for a 12 μm by 2 mm long ridge QCL [21], 338 $WK^{-1}cm^{-2}$ for a 7.5 μm wide buried heterostructure stripe and 1461 $WK^{-1}cm^{-2}$ for a 3 μm wide buried heterostructure stripe [11]. This is reportedly due to a highly anisotropic thermal

conductivity within the superlattice active region where the lateral thermal conductivity is higher than perpendicular to the layers [22, 23]. Therefore, a narrow ridge width can be more important than the material laterally adjacent to the active region.

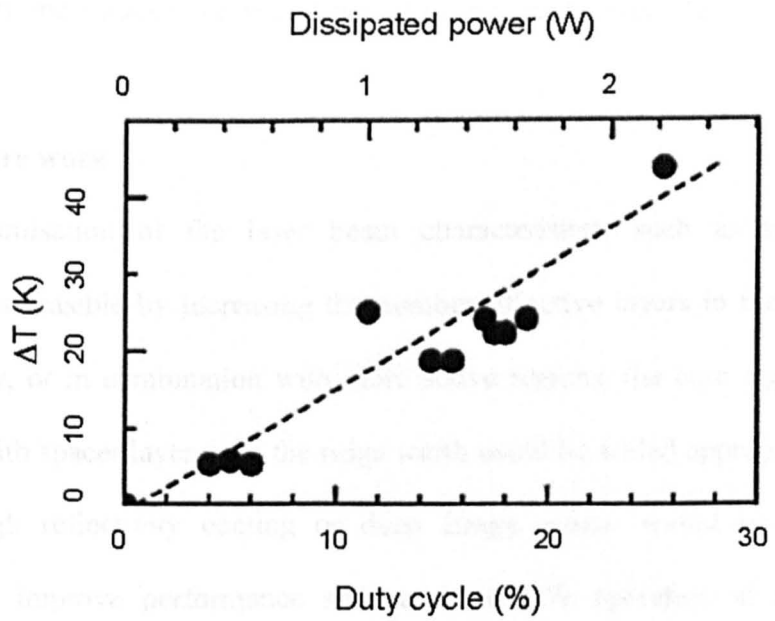

Figure 6.8 Increase in active region temperature (ΔT) plotted against duty cycle. Dashed line represents the linear fit of the data. From the linear fit, the thermal resistance is $R_{th} \approx 18$ K/W and the thermal conductance is $G_{th} \approx 380$ W K^{-1} cm^{-2}.Reproduced from [20]

6.4 Summary

A mid-infrared quantum cascade laser (λ ≈ 3.9 μm) operating at room temperature has been described. A narrow ridge width was used to achieve a symmetric far-field profile with improved beam quality. Even with a relatively narrow ridge width (~5 μm), the average output power exceeded 60mW for a thermoelectrically cooled,

pulsed operated laser. This is sufficient for mid-infrared spectroscopic and imaging applications. The narrow ridge increases the relative lateral heat dissipation from the active region, resulting in a thermal conductance per unit area as high as G_{th} = 380 $WK^{-1}cm^{-2}$ for a 3mm long device. The use of a PECVD silicon nitride insulation layer covered with thick electroplated gold resulted in a total thermal conductance comparable to the values obtained for buried heterostructure quantum cascade lasers.

6.5 Future work

Further optimisation of the laser beam characteristics, such as smaller beam divergence is feasible by increasing the number of active layers in the core region. Alternatively, or in combination with more active regions, the core region could be interlaced with spacer layers and the ridge width could be scaled appropriately. Some form of high reflectivity coating or deep Bragg mirror would be expected to significantly improve performance and result in CW operation at much higher temperatures. Additionally, an investigation into the optimum ridge width, depth and insulating layer thickness could yield further improvements. The thermal conductivity of semiconductor multilayered heterostructures is anisotropic. When the layer widths are comparable or smaller than the phonon mean free path (40 – 250 Å at 300 K) the rate of phonon scattering by interfaces increases (with temperature), hampering the phonon transport and reducing the heat dissipation rate. Consequently, both the thermal conductivity components in both planes can be much lower than for bulk materials. Further improvement in thermal conductivity could be gained by designing buffer layers in the active region. All the above improvements could be used to produce high power distributed feedback lasers for use in high resolution spectroscopic applications.

6.6 References

[1] Gao, X., Zheng, Y., Kan, H., Shinoda, K.: 'Effective suppression of beam divergence for a high-power laser diode bar by an external-cavity technique', Opt. Lett. 2004, 29, pp. 361

[2] Chi, M., Thestrup, B., Petersen, P. M.: 'Self-injection locking of an extraordinarily wide broad-area diode laser with a 1000-mm-wide emitter',Opt. Lett. 2005, 30, pp. 1147

[3] Guo, B., Wang, Y., Peng, C., Zhang, H. L., Luo, G. P., Le, H. Q., Gmachl, C., Sivco, D. L., Peabody, M. L., Cho, A.Y.: 'Laser-based mid-infrared reflectance imaging of biological tissues', Opt. Express. 2005, 12, 1, pp. 208-219

[4] Wang, Y., Wang, Y., Le, H. Q.: 'Multi-spectral mid-infrared laser stand-off imaging', Opt. Express (2005), 13, 17, pp. 6572-6586

[5] Moeskops, B. W. M., Cristescu, S. M., Harren, F. J. M.: 'Sub-part-per-billion monitoring of nitric oxide by use of wavelength modulation spectroscopy in combination with a thermoelectrically cooled, continuous-wave quantum cascade laser', Opt. Lett. 2006, 31, 6, pp. 823-825

[6] Nelson, D. D., McManus, J. B., Herndon, S. C., Shorter, J. H., Zahniser, M. S., Blaser, S., Hvozdara, L., Muller, A., Giovannini, M., Faist, J.: 'Characterization of a near-room-temperature, continuous-wave quantum cascade laser for long-term, unattended monitoring of nitric oxide in the atmosphere', Opt. Lett. 2006, 31, 13, pp. 2012-2014

[7] Diehl, L., Bour, D., Corzine, S., Zhu, J., Hofler, G., Loncar, M., Troccoli, M., Capasso, F.: 'High-temperature continuous wave operation of strain-balanced quantum cascade lasers grown by metal organic vapor-phase epitaxy', Applied Physics Lett. 2006, 89, 081101

[8] Diehl, L., Bour, D., Corzine, S., Zhu, J., Hofler, G., Loncar, M., Troccoli, M., Capasso, F.: 'Pulsed- and continuous-mode operation at high temperature of strained quantum-cascade lasers grown by metalorganic vapor phase epitaxy', Applied Physics Lett. 2006, **88**, 041102

[9] Bewley, W. W., Lindle, J. R., Kim, C. S. Vurgaftman, I., Meyer, J. R., Evans J. S., Yu, J.S., Slivken, Razeghi, M .: 'Beam Steering in High-Power CW Quantum-Cascade Lasers', IEEE J. of Quant. Elect., 2005, 41, 6, pp. 833-841

[10] Gresch, T., Giovannini, M., Hoyer, N., Faist, J.: 'Quantum cascade lasers with large optical waveguides', IEEE Photon. Technol. Lett. 2006, 18, 3, pp. 544-546.

[11] Gmachl, C., Capasso, F., Tredicucci, A., Sivco, D., Köhler, R., Hutchinson, A., Cho, A.: 'Dependence of the device performance on the number of stages in quantum-cascade lasers', IEEE J. Sel. Topics Quantum Electron., 1999, 5, 3, pp. 808–816.

[12] Semtsiv, M. P., Ziegler, M., Dressler, S., Masselink, W. T., Georgiev, N., Dekorsy, T., Helm, T.: 'Above room temperature operation of short wavelength (λ=3.8μm) strain-compensated $In_{0.73}Ga_{0.27}As$-AlAs quantum-cascade laser', *Appl. Phys. Lett.*, 2004, 85, pp. 1478–1480

[13] Evans, A., Yu, J. S., David, J., Doris, L., Mi, K., Slivken, S., Razeghi M.: 'High-temperature, high-power, continuous-wave operation of buried heterostructure quantum-cascade lasers', Appl. Phys. Lett. 2004, 84, 3, pp. 314-316

[14] Yu, J. S., Slivken, S., Evans, A., Doris, L., Razeghi M.: 'High-temperature, high-power, continuous-wave operation of a 6μm quantum-cascade laser at room temperature', Appl. Phys. Lett. 2005, 83, 13, pp. 2503-2505

[15] FIMMWAVE / FIMMPROP by Photon Design Ltd, UK, www.photond.com

[16] Gunde, M. K., Maček, M.: 'Infrared Optical Constants and Dielectric Response Functions of Silicon Nitride and Oxynitride Films', Physica Status Solidi (a) 2001,

183, 2, pp.439-449

[17] Siegman, A. E.: 'Defining, measuring, and optimizing laser beam quality', Proc. *SPIE. 1993, 1868: Laser Resonators and Coherent Optics: Modeling, Technology, and Applications,* pp. 2-12

[18] Silfvast, W. T.: 'Laser Fundamentals', Cambridge University Press, 1996.

[19] Faist, J., Capasso, F., Sirtori, C., Sivco, D. L., Hutchinson, A. L., Cho, A. Y.: 'Continuous wave operation of a vertical transition quantum cascade laser above T=80 K', Applied Physics Lett. 1995, 67, 21, pp. 3057-3059

[20] Weinold, M., Semtsiv, M. P., Bayrakli, I., Masselink, W. T., Ziegler, S., Kennedy, K., Hogg, R.: 'Optimcal and thermal characteristics of narrow-ridge quantum-cascade lasers', J. *Appl. Phys.* 2008, 103, 083113

[21] Slivken, S., Yu, J. S., Evans, A., David, J., Doris, L., Razeghi M.: 'Ridge-Width Dependence on High-Temperature Continuous-Wave Quantum-Cascade Laser Operation, IEEE Phot. Tech. Lett. 2004, 16, 3, pp. 744-746

[22] Pflügl, C., Litzenberger, M., Schrenk, W., Pogany, D., Gornik, E., Strasser, G.: 'Interferometric study of thermal dynamics in GaAs-based quantum-cascade lasers', Appl. Phys. Lett. 2003, 82, 11, pp.1664-1666

[23] Lops, A., Spagnolo, V., Scamarcio, G.: 'Thermal modeling of GaInAs/AlInAs quantum cascade lasers', J. Appl. Phys. 2006, 100, 043109

Chapter 7 - Conclusions

The work presented within this thesis has successfully demonstrated high power single-mode laser devices suitable for spectroscopic applications such as trace gas detection at mid-infrared wavelengths ($\lambda \sim 10\mu m$). The increasing demand for low cost mid-infrared sources with narrow emission linewidths at thermoelectric cooler temperatures has created much interest in quantum cascade DFB lasers. This thesis has addressed a lack of information in the literature as to the potential single mode yield of these devices and demonstrated new designs and processes that will aid the development of even more advanced and lower cost lasers. The work has provided additional information on the emission wavelength dependence on the ridge width and provides a potential mechanism for widely tunable devices.

Single-mode quantum cascade DFB lasers ($\lambda \sim 10\ \mu m$) with high peak output powers (>200mW) and a single mode yield of 80% were observed. These devices had as-cleaved facets and utilised a gold coated surface grating that was etched by inductively coupled plasma. V-groove shaped gratings were etched using only a resist mask which is simpler than using dielectric or metal etch masks. The coupling coefficient may be lower in comparison to a rectangular shaped grating but side mode suppression ratio is not significantly affected. The reduced coupling may even be preferable in some devices. Furthermore, there are potential benefits to end facet quality and consistency after the cleaving process.

Additional information is provided about the spread of wavelengths from the same sample showing that wavelength control is a non-trivial part in the development of

low cost devices. Tight wavelength specifications from systems suppliers may have a large impact on device yields even if the single-mode and side mode suppression ratio yields are high. A constant grating period and ridge width will improve the control of the emission wavelength but control over the refractive index and thickness of the semiconductor, isolation and electrical contact layers is also critical.

The first demonstration of an InP-based quantum cascade DFB laser with deep etched lateral gratings is presented in this thesis. The devices were fabricated using a novel multi-stage ICP etch process. The smooth and vertical etching process plays a vital role in achieving such devices. The suitability of the lasers for use in sensitive trace gas detection systems is demonstrated and a model to calculate the coupling coefficient is shown to be in good agreement with initial experimental results. The use of a lateral grating design significantly simplifies the fabrication process allowing simultaneous etching of the grating and ridge. Furthermore, it may enable more advanced devices in the future. Careful attention must be paid to the dimensions of the grating and ridge width. Lasers with different emission wavelength may require significantly different dimensions. Greater output powers may not simply be achieved with wider ridges as grating coupling strength will decrease and so lasers may no-longer retain their single-mode operation.

The study of the ridge width dependence on emission wavelength demonstrates the potential for using multiple quantum cascade laser ridges with the same (or variable) grating periods to achieve large tuning ranges. High power, single mode lasers with side mode suppression ratios greater than 25dB over a wide temperature range were observed for a buried grating design. The grating and ridges were etched using an

inductively coupled plasma etch process using a $SiCl_4$ / Ar chemistry. The grating was successfully overgrown by gas source MBE. A large emission wavelength tuning range in excess of 230nm was observed by utilising a temperature and ridge width dependence on emission wavelength. Since a single grating period is used this may simplify the fabrication process and increase yields as holographic lithography may be used to pattern a single wafer. Multiple ridge widths on a single chip may be used to increase the chance of achieving the desired wavelength. Typically, the need for a buried grating becomes more important for shorter wavelengths where less of the optical mode will overlap with a surface grating and there is less refractive index contrast between gold and semiconductor.

The ridge width has also been shown to affect the far-field profile of quantum cascade lasers and may be utilised to produce symmetrical far-field profiles which are more suitable for some imaging applications. Furthermore, a narrow ridge width has been shown to allow better extraction of heat from the active region which improves laser performance. A similar thermal conductance value for a ridge waveguide laser compared to buried waveguide devices may allow a simpler device fabrication process.